Osaka University – Graduate School of Science

Department of Physics

Doctor of Philosophy Dissertation

Study of Multilayered Cuprate Superconductors by Electronic Raman Scattering

by

Giulio Vincini

Osaka 2018

Index

1:Introduction

Since their discovery in 1985 the cuprates superconductors have attracted a huge attention from the community in the field of solid state physics, and a tremendous amount of work has been put into clarifying the mechanism that gives to these superconductors such a high critical temperature, however some of the fundamental questions still remain unanswered. The first of these is surely the pairing mechanism, and therefore the driving force of superconductivity. Nevertheless the joint work of the community took us much closer to understanding the rich physics of these materials. However while new experimental observation take us closer to understanding the cuprates, they also bring forth new questions that are sometimes are not easily solved.

A perfect example of these long standing issues in the research of cuprates superconductors is the doping dependence of the superconducting gap. While in the overdoped regime the gap size is proportional to the critical temperature T_C, in the underdoped region the antinodal and nodal gaps show different doping dependence, with the antinodal gap increasing monotonically[1] and the nodal gap staying constant or decreasing with lower doping, and this is accompanied by a deviation of the gap function from the simple d-wave symmetry.[2]–[4] Therefore in the underdoped regime we have the highly unusual situation where neither the nodal nor the antinodal gap seem to be proportional to the critical temperature.

This behaviour is likely connected to the poorly understood pseudogap state, which dominates the phase diagram in the underdoped region. Even though from recent experiments results it seems likely that the pseudogap state originates from a different order parameter than superconductivity, the fundamental nature of the pseudogap state is still unclear. Additionally the relationship of the pseudogap with superconductivity is not fully understood. While it is true that these two states do seem to compete for the area of the Fermi surface close to the antinode, on the other hand they coexist and it is not clear how superconductivity is influenced.

A further unclear point is that the different nodal and antinodal energy scale in the underdoped side is picked up in a different way by different momentum sensitive techniques such as Angle Resolved Photoemission Spectroscopy ARPES and Raman. This apparent inconsistency needs to be addressed to improve our understanding of the doping dependence of the pseudogap and superconductivity.

Another interesting topic of the field is the study of multilayer cuprates. The main reason for the interest in these is that the T_c of the cuprates strongly depends on the number of Cu-O_2 planes per unit cell n. T_c increases when n increases from n=1 to n=3, where it reaches its maximum, and then decreases for $n\geq4$. [5] Up to date the cause of this T_c enhancement is not clear, with several possible factor being proposed, such as the tunnelling of Cooper pairs between different layers[6], the increased next-nearest neighbour hopping parameter t'[7] and the disorder protection of the inner Cu-O_2 plane IP by the outer Cu-O_2 planes OP.[8] Additionally for $n\geq3$ an interesting situation arises, namely that Cu-O_2 planes with different doping level coexist in the same sample, and the

OP is more doped than the IP due to its proximity to the charge reservoir layer CRL.[9] How these layers interact with each other, and how this affects T_C is an open problem that should be solved to understand the source of the high T_C of the triple layer cuprates. Unfortunately the difficulty of growing high quality single crystal is higher in the case of triple layer cuprates, and this held back the research for long. However the recent improvement in sample quality now allows to carry out new observations on these materials.

In this work we focused on $Bi_2Sr_2Ca_2Cu_3O_{10}$ Bi2223 the triple layer member of the BSCCO family ($Bi_2Sr_2Ca_{n-1}Cu_nO_{2n+4}$) of cuprates superconductors. Using Electronic Raman Scattering ERS, which is a powerful energy and momentum resolved technique, we investigated this triple layer cuprate. We were able to observe a signature of the double superconducting gap of this material, originating from the two inequivalent kind of Cu-O_2 plane (IP and OP), which has never been observed previously by Raman. The temperature and doping dependence of this double peak structure was investigated, and a higher energy scale for this triple layer material, with respect with other single and double layer cuprates, was observed. These results have been explained by a combination of multilayer effects and the complex relationship between superconductivity and the pseudogap. This could be a step forward in understanding the non-trivial physics of multilayer cuprates.

Additionally in order to try to solve the apparent inconsistencies between Raman and ARPES, and to improve our understanding of the Raman spectra, we performed calculations of the Raman spectra, starting from the ARPES data, using the Kubo formalism. This was done for the double layer component $Bi_2Sr_2Ca_1Cu_2O_8$ Bi2212 samples of three different dopings and for an optimally doped Bi2223 sample. The doping dependent Bi2212 study allowed us to show how the inconsistencies between Raman and ARPES are likely to be only due to a difference in how these two techniques pick up the effect of the coexistence between superconductivity and the pseudogap, and how the relationship between these two states affects the Raman spectra. The Bi2223 calculation was successful, and constitutes a strong proof that the origin of the experimental double peak structure, observed in this work, is truly the double superconducting gap of this material originating from the two inequivalent Cu-O_2 planes, the IP and the OP.

2:Background

2.1 High temperature superconductivity

The history of superconductivity begins in the early years of the 20th century, when scientists were wondering how the resistivity of metals would have been close to the absolute zero. Thanks to the newly discovered Hampson–Linde cycle for the liquefaction of gases, investigation of the low temperature resistivity of materials had just became possible. Driven by this interest the Dutch physicist Heike Kamerlingh Onnes was able in 1908 to produce liquid helium for the first time. With this newly achieved technology Onnes and Jacob Clay started measuring the low temperature resistivity of platinum and gold. They later moved to mercury and in 1911 they observed an abrupt drop in the resistivity at 4.19 K. They observed that at this temperature the resistivity of mercury became almost zero. This observation marked the discovery of superconductivity. Onnes was also able to show the persistence of the current in superconducting rings without an applied voltage, and in 1913 he received the Nobel Prize for the discovery of Superconductivity. In the following decades several other superconductors were discovered, but these had low critical temperature T_c (<20K).

A turning point in the history of superconductivity is when in 1957 John Bardeen, Leon N. Cooper, and Robert Schrieffer formulated their theory of superconductivity, the BCS theory[10], for which they earned the Nobel Prize in Physics in 1987.The BCS theory gave for the first time a successful microscopic picture of the phenomenon. The fundamental idea is that electrons bind themselves in Cooper pairs. Here a weak positive attraction between two electrons mediated by the coupling with the lattice (phonon) can cause them to form pairs, despite the strong Coulomb repulsion between the electrons. The so formed pairs could condense in the same way bosons condense in a superfluid state. Prediction based on the BCS theory suggested that the pairing energy had to be smaller than the typical phonon energy, and therefore it was believed that T_c could not exceed 30K[11].

However in 1985 a new superconductor was discovered that exceeded this limit. In that year Bednorz and Müller discovered the copper oxide perovskite $La_{2-x}Ba_xCuO_4$ which had a T_c of 35K.[12] This was the first of a new family of superconductors, which re-sparked interest in the field, the cuprates. These had as common feature a layered structure and CuO_2 planes separated by different ionic layers named charge reservoir layers CRL. The cuprates were of great interest not only because the maximum T_c at ambient pressure was quickly raised to 133K-138K in $HgBa_2Ca_2Cu_3O_{8+\delta}$ [13], [14], but also because the BCS theory could not predict many of their fundamental characteristics.

For some time the cuprates remained the only High Temperature Superconductors HTS, but this changed in 2006, when Iron Based Superconductors IBS where discovered[15], [16]. These materials contain a common structural unit of iron - pnictide conductive layers separated by an insulating blocking layer. The discovery of IBS was surprising since iron, having a large magnetic momentum, was believed to be harmful to superconductivity. IBS were believed to be the new

high temperature superconductor, and showing such a good promise, they re-sparked a huge interest in the field of superconductivity.

Surprisingly though the record T_c held by cuprates was not broken by IBS. Instead in 2015 superconductivity was discovered in H_2S with a T_c of 203 K at extremely high pressures (around 150 gigapascals)[17]. Even though actually the phase responsible for such high T_c is likely to be H_3S, formed from H_2S by decomposition under pressure. What is even more surprising is that unlike the cuprates or the IBS which show exotic properties and cannot be simply explained by the BCS theory, the newly discovered H_2S can be explained by the BCS theory and in fact numerous calculation have predicted high transition temperatures for many hydrides.[18]

Even though more than one century of research on superconductivity has been carried out, a great part of its rich physics remains poorly understood, and many surprising results keep on being uncovered. Although much work is still needed, the huge effort of many researchers got us closer to understanding this fascinating phenomenon and allowed us to increase the T_c enormously. As it can be seen form Fig. 2.1 we went from the few kelvin of mercury to the 203K reached recently, getting us closer to the dream of room temperature superconductivity.

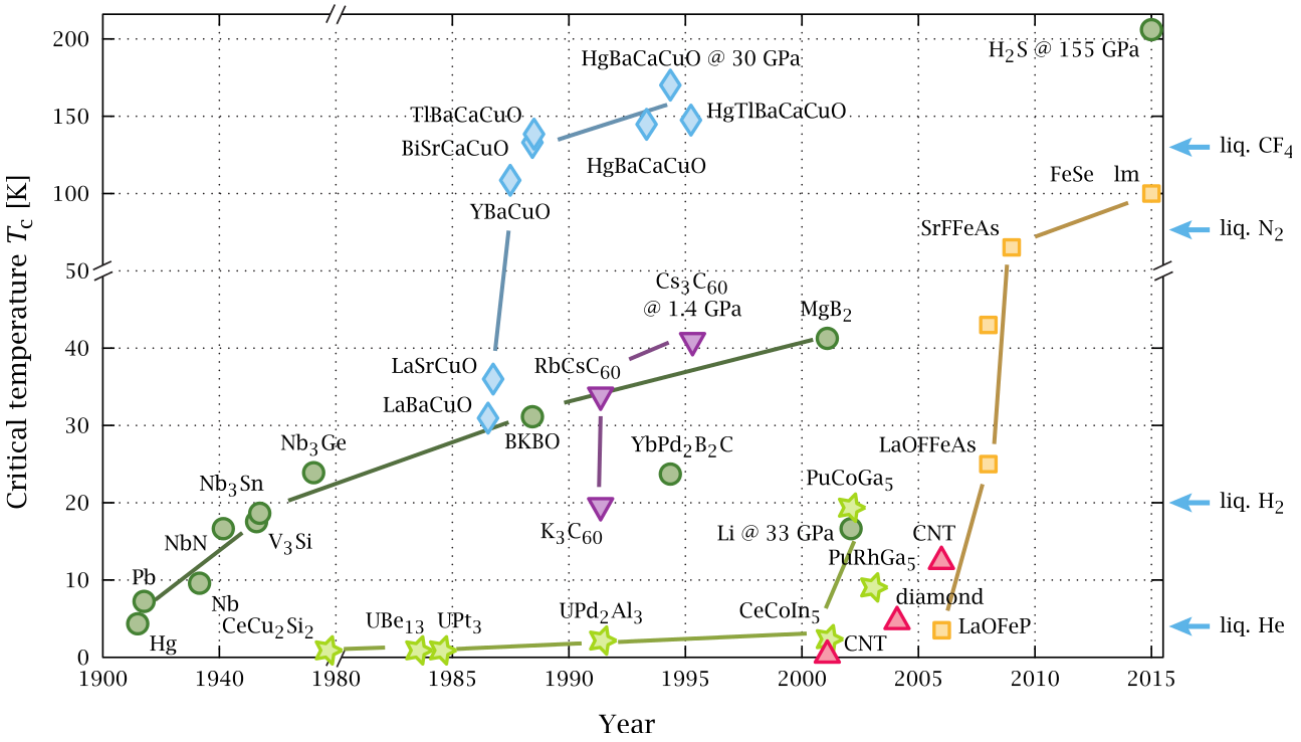

Fig 2.1 Superconductors T_c plotted against the year of discovery. Taken from Ref [19]. Axes are not in scale for easier visualization.

2.2 Cuprates general concepts

Following the discovery of $La_{2-x}Ba_xCuO_4$ other copper oxide based superconductors where discovered. These all have in common one or multiple CuO_2 layers separated by different ionic, electronically inert, buffer layers. The buffer layers can contain different ions such as lanthanum, barium, strontium, or other atoms. These ions act as a stabilizer of the crystal structure and the doping can be controlled by changing the chemical composition of this buffer layer, which is therefore usually referred as charge reservoir layer CRL.

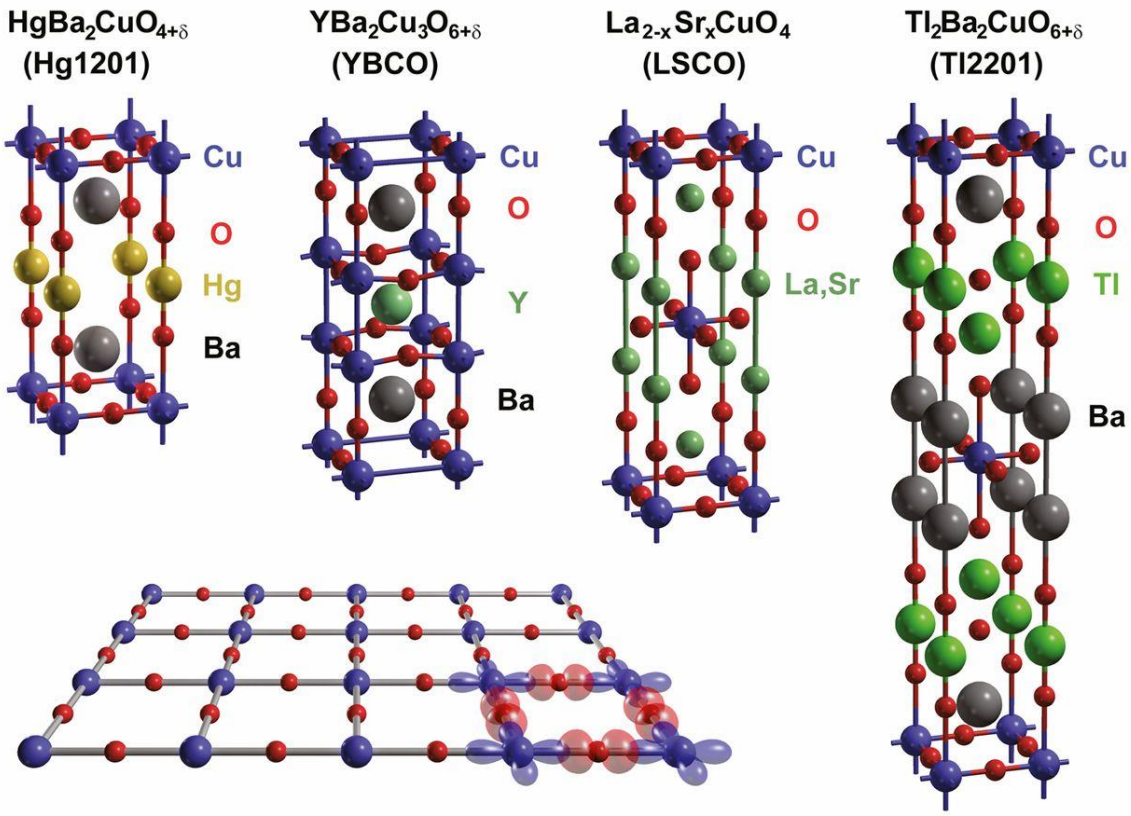

Fig. 2.2 Crystal structure of some example cuprates superconductors. Taken from Ref [20]. All cuprates have one or multiple CuO_2 layers in common (bottom left) separated by different ionic buffer layers.

The layered structure of cuprates, with weak interaction between the layers, makes cuprates quasi-2D materials, and therefore gives them a quasi 2D electronic structure. Nevertheless for realistic band dispersion calculations, and to introduce the material variability interaction out of plane should be considered. [7], [21] A single band crosses the Fermi level in cuprates which comes mainly from the hybridization of Cu d_{x2-y2} and O p_x p_y states (shown in the bottom left of Fig. 2.2) and forms a large hole like fermi surface as it can be seen in Fig2.3 (e).

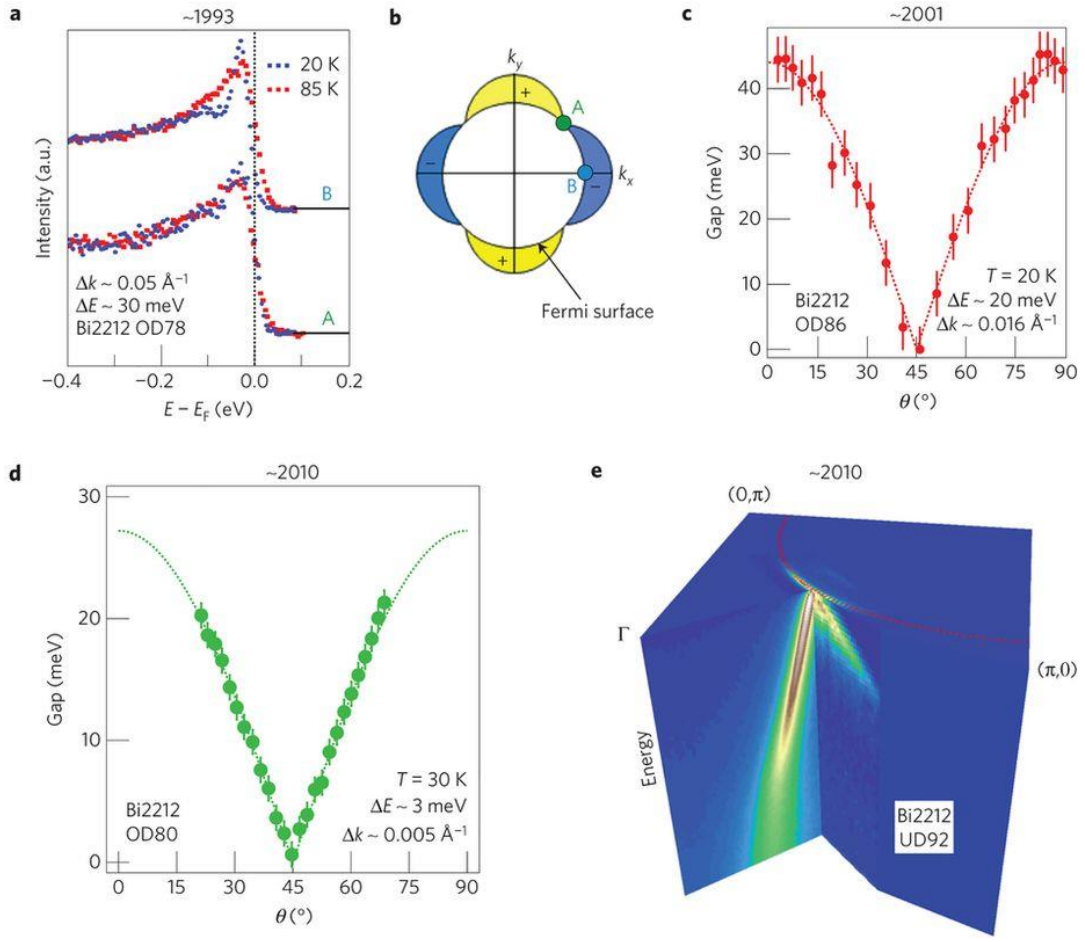

Fig2.3 Taken form Ref[1]. **a** Superconducting gap anisotropy in cuprates, first observed in 1993 in Bi2212 (Ref[22]) the A and N are the nodal and antinodal spectra respectively. **b** Schematic of a d-wave superconducting order parameter. The gap is zero at the node A where it changes sign and reaches the maximum at the antinode B. **c** Bi2212 gap measured by synchrotron ARPES. **d** Bi2212 Gap measured by laser ARPES. **e** Three-dimensional ARPES data set, showing the quasi-particle dispersions both perpendicular and parallel to the Fermi surface near the node, reproduced from Ref [23].

As it will be discussed more in detail later on, the cuprates are antiferromagnetic Mott insulators at zero doping. By doping electrons or holes superconductivity appears, and the superconducting gap opens in the above mentioned band. In this work the discussion will be limited to hole doped cuprates for simplicity. In contrast with the isotropic *s*-wave gap of conventional BCS superconductors the gap in cuprates, was shown to possess *d*-wave symmetry [1] as it can be seen in Fig.2.3. The superconducting order parameter changes sign at the (0,0)-(π,π) axes of the momentum space. These zones where the gap becomes zero are named nodes, while the zones where the gap is maximum, along the (0,0)-(π,0) axes, are referred as antinodes. A schematic representation of the *d*-wave (d_{x2-y2}) order parameter can be seen in Fig.2.3 (b).

One feature of the conventional BCS superconductor, where phonon is the pairing interaction, is the isotope effects. This is the dependence of T_c on the isotope mass *M*. Changing the isotope mass changes the energy of the phonon and therefore T_c according to the empirical relations T_c

$\propto M^{-\alpha}$. The isotope coefficient α predicted form the BCS theory is 0.5. On the other hand as it can be seen in Fig2.4 the cuprates show a non-trivial α which depend on the doping *p* and on the number of CuO_2 planes per unit cell *n*. From the early days of the research on cuprates similar observations on the isotope coefficient α suggested that the phonons had to be ruled out from the possible pairing interactions. [24]

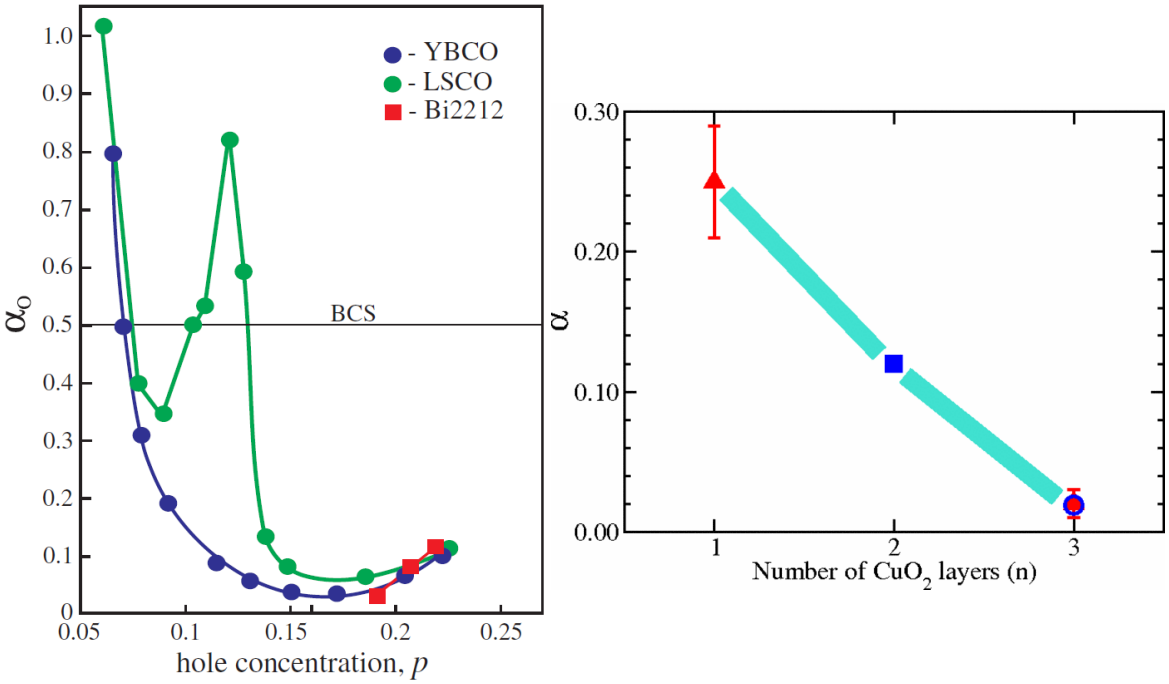

Fig2.4 **a** Doping dependence of the isotope coefficient α. Taken from Ref.[25] **b** Dependence on the number of layer per unit cell of the isotope coefficient α. Taken from Ref.[26]

Cuprates are all type II superconductors, meaning that due to their short coherence length ξ with respect to the penetration length λ, if a strong enough magnetic field is applied, the filed will not be completely expelled from the superconductor. Instead some lines of magnetic flux will pass through the material, turning a region of the superconductor normal, these region are known as vortex, or an Abrikosov vortex. The existence of type II superconductor had been predicted by the Ginzburg-Landau theory[27], which predicted a negative energy of the interface between superconducting and normal phases. Experimentally type II superconductors have two critical fields, which separate the 3 regions of complete Meissner effect, vortex state and suppression of superconductivity.

The hole doped cuprates feature a rich and complex phase diagram which can be seen in Fig2.5 and that will be treated more in detail later on. Different competing orders appear at low temperature. Among these the pseudogap PG attracted a strong interest from the community. This appears as a suppression of the density of states, in the underdoped and optimally doped cuprates, at temperature much larger than T_c. The nature of the pseudogap was and still is a controversial topic. Two main theories existed, one attributing the pseudogap to a precursor state of superconductivity and the other attributing the pseudogap to a different competing order.

Recent experiments point to the latter as correct answer, but some issues still remain to be clarified.

One of the perquisite to achieve high T_c according to the BCS theory is a high density of states at the Fermi level N_F [28], however the cuprates, at room temperature above the superconducting region, are such poor conductors that they can hardly be classified as metals. Additionally the conductivity in this region exhibits frequency and temperature dependence which are incompatible with the conventional theory of metals. This led to this region of the phase diagram to be referred as "strange metal" which can be seen in Fig 2.5. This phase and the Mott insulator phase are a consequence of the strong correlation between electrons. Similar behaviour has been observed numerous non superconducting materials [29] The cuprates and these non-superconducting materials, in which the interaction between the electrons is strong, are therefore a new class of materials called "highly correlated electron systems" which cannot be well described by the conventional quantum theory of solids.

The cuprates showed numerous inconsistencies with the conventional BCS superconductors, and therefore earned the name of unconventional superconductors. The most prominent of these differences is, most likely, the pairing interaction, and therefore the nature of the superconducting mechanism. As stated before the phonons have been ruled out from the possible pairing interactions and several other candidates have been proposed. These include charge or spin mediated pairing. However no clear solution has been found and this fundamental point is still under debate.

2.3 Phase diagram of cuprates

The phase diagram of cuprates is packed with different phases, most of which have a rich physics behind. An example of phase diagram of the cuprates can be seen in Fig.2.5. As stated before in the underdoped side the strong correlation effects make the cuprates Mott insulators, and below T_N, antiferromagnetism kicks in (blue area in Fig.2.5). With increasing doping after the first critical doping p_{min} superconductivity appears at low temperature. The superconducting phase is present in a dome like area of the phase diagram (green area in Fig.2.5), where the maximum T_c is reached at the optimal doping p_{opt}=0.16, and it disappears at the second critical doping p_{max} in the overdoped side. In the underdoped side below T* the pseudogap phase is visible (yellow area in Fig.2.5). As it can be seen in Fig.2.5 the pseudogap phase coexists with superconductivity at low temperature, and this is indicated by the lighter green area. Above T* and above T_c at intermediate doping, the previously mentioned strange metal phase appears, which is indicated with the magenta area in Fig.2.5. At higher doping the anomalies of the strange metal phase disappear, and are substituted by a Fermi liquid-like behaviour (white area in Fig.2.5). Additionally to these phases a variety of different competing order are seen in the phase diagram, competing with superconductivity. These include spin-density-wave SDW or stripe order, charge-density – wave CDW, electron-nematic phase and others. Some interesting aspects of these orders remain

yet to be explained, but their existence and many of their main features were explained and anticipated by theory.[30]

In the following sections the most relevant phases will be examined more in detail.

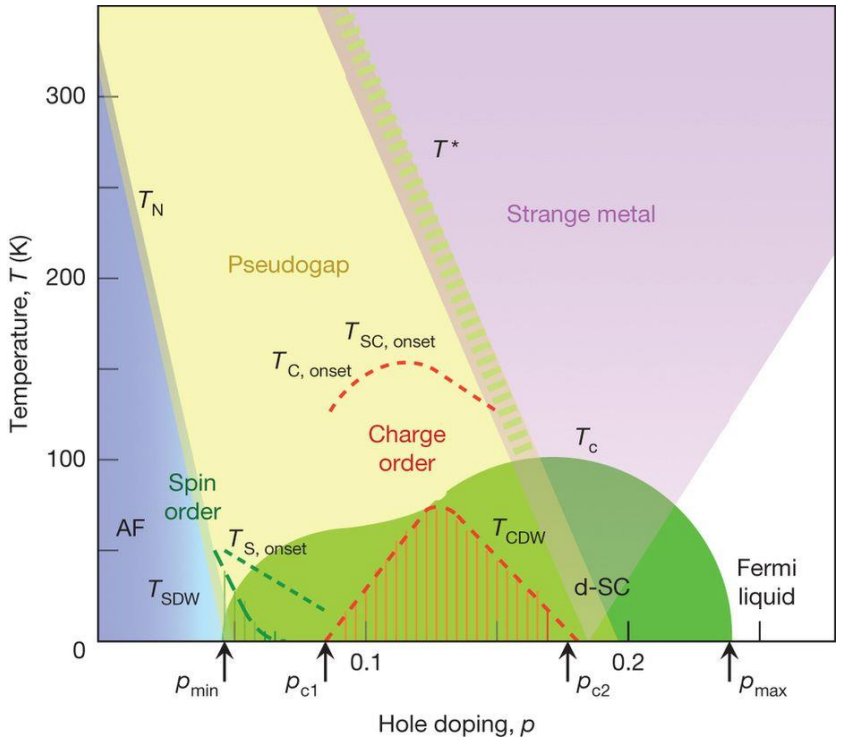

Fig.2.5 Phase diagram of cuprates taken from Ref.[31]

2.3.1 Mott insulating phase and anti-ferromagnetism.

The zero doping curates accommodate an even number of electrons per unit cell, therefore the conventional band theory would predict them to be metallic. However strong correlation between the electrons, and in particular strong Coulomb repulsion between the electrons, makes the underdoped cuprates Mott insulators. Defining U as the on-site Coulomb repulsion and t as the transfer integral between neighbouring atoms, in the case of half-filled band, when $t > U$ a metallic behaviour can be expected, but if on the other hand $U > t$ a Mott insulator is expected. In this case the lower energy state will be achieved by localized electrons around their respective ions, that minimize the Coulomb repulsions energy term. These localized electrons cannot occupy the same site unless they are given the on-site repulsion energy U, and therefore the material will be a Mott insulator, with an energy gap of U (Hubbard gap).

The localized electrons spins interact between each other. If the spins of the two neighbouring electrons are antiparallel they could penetrate in each other site without violating the Pauli exclusion principle, even if this is prevented by the strong U. Therefore if the spins are antiparallel there will be a gain in energy given by the exchange constant J, on the other hand if the spins are

parallel there will be no gain in energy since the Pauli exclusion principle prohibits the process. Following these considerations there can be two possibilities. One is AFM long range order, which is indeed observed as seen in the phase diagram in Fig.2.5. The other possibility is that the electrons form paired singlet without requiring long range order. In this case even if the electrons are localized the spins can move freely. This second possibility is the so called resonating valence bond or quantum spin fluid.[32]

With increasing doping the AFM and Mott insulating phase disappears as it can be seen in the phase diagram in Fig.2.5. The Neel temperature T_N decreases and the sample starts showing metallic behaviour entering the strange metal phase, while at low temperature superconductivity appears.

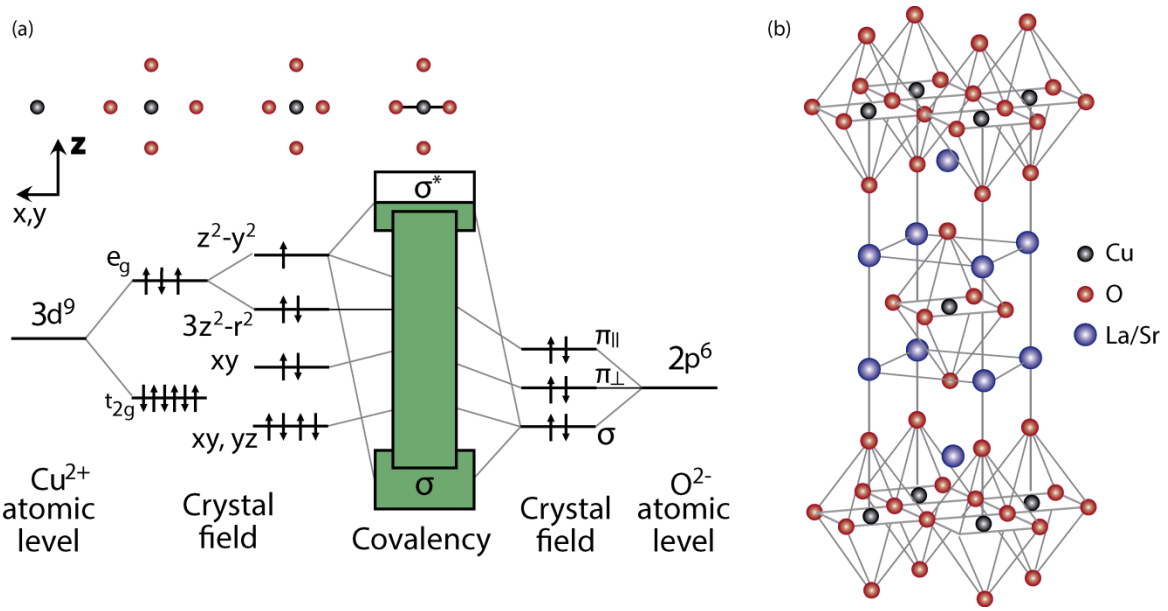

Fig.2.6 Taken from Ref.[33] **a** Crystal-field splitting and hybridization giving rise to the Cu-O bands. **b** Crystal structure of La_2CuO_2 LCO

To understand the electronic structure of the underdoped cuprates the single layer $La_{2-x}Sr_xCuO_2$ LSCO can be discussed for simplicity. In particular, to examine the underdoped regime, the un-doped La_2CuO_2 LCO can be used whose crystal structure is shawn in Fig.2.6 (b). The outer 3*d* shell of the Cu^{2+} atoms contains nine electrons, while the O^{2-} ions have an outer 2*p* shell which is fully filled with 6 electrons. Forming an octahedron with the 6 neighbouring O atoms splits the Cu 3d levels in t_{2g} and e_g levels. The octahedron in LCO is distorted, with a longer Cu-O bonding direction in the *c* direction than in the *ab* planes. This is the so called Jahn-Teller distortion which splits furtherly the 3*d* orbitals in d_{yx}, d_{zx}, d_{xy}, $d_{z2\text{-}r2}$ and $d_{x2\text{-}y2}$. All of these are fully occupied except for the $d_{x2\text{-}y2}$ orbital which is the highest in energy and accommodates only a single electron. The oxygen *p* orbitals separate in p_σ $p_{\pi\perp}$ and $p_{\pi\parallel}$. Of these p_σ is parallel to the Cu-O bonding directions while $p_{\pi\perp}$ and p_π are perpendicular to the Cu-O bonding directions, with $p_{\pi\parallel}$ being in plane and $p_{\pi\perp}$ being out of plane. The oxygen p_σ strongly hybridize with the copper $d_{x2\text{-}y2}$ orbitals. The above described splitting and hybridization can me seen in Fig.2.6 (a). With these considerations one of the simplest way to treat the problem is to write a Hamiltonian for non-interacting electrons,

considering only the Cu d_{x2-y2} orbital and the O p_σ orbitals (p_x or p_y) and considering only the nearest neighbour hopping in the form:

$$H_0 = \epsilon_d \sum_{i\sigma} n_{d\sigma}(i) + \epsilon_p \sum_{j\sigma} n_{p\sigma}(j) + \sum_{<ij>\sigma} V_{ij}\left(d_{i\sigma}^{\dagger} p_{j\sigma} + p_{j\sigma}^{\dagger} d_{i\sigma}\right) \qquad (2.1)$$

Here $d_{i\sigma}^{\dagger}$ creates a hole in the Cu d_{x2-y2} orbital, $p_{j\sigma}^{\dagger}$ creates a hole in the O p_x (or p_y), $< ij >$ indicates the summation on nearest neighbour and $V_{ij} = (-1)^{\alpha_{ij}} t_{pd}$ where t_{pd} is the hopping integral between oxygen and copper orbitals and α_{ij} changes sign according to the relative position of the O and Cu atoms. However this simple Hamiltonian will give metallic solutions, since the conventional band theory always predict metallic band structure for half filled bands. To improve the calculation, the correlation between the electrons must be considered. Adding the Coulomb repulsion between electrons U and considering also the nest-nearest neighbour hopping t_{pp} we can write the Hamiltonian:[34]

$$\begin{aligned} H = \; & \epsilon_d \sum_{i\sigma} n_{d\sigma}(i) + \epsilon_p \sum_{j\sigma} n_{p\sigma}(j) + t_{pd} \sum_{<ij>\sigma} \left(d_{i\sigma}^{\dagger} p_{j\sigma} + h.c.\right) + t_{pp} \sum_{<jj'>\sigma} \left(p_{j\sigma}^{\dagger} p_{j'\sigma} + h.c.\right) \\ & + U_d \sum_i n_{i\uparrow}^d n_{i\downarrow}^d + U_p \sum_j n_{j\uparrow}^p n_{j\downarrow}^p + U_{pd} \sum_{<ij>,\sigma} n_{i\sigma}^d n_{i-\sigma}^p \qquad (2.2) \end{aligned}$$

Here the terms U_d , U_p and U_{pd} are the on site Coulomb repulsion between holes on the copper site, on the oxygen site and the coulomb repulsion between holes on nearest neighbour site respectively. This triple band Hubbard Hamiltonian can give a correct but approximate description of the underdoped cuprates electronic structure. In cuprates since *U*>*W* (where W=8t is the typical width of the band) from the metallic solution of the Hamiltonian in (2.1) where 3 bands are present (bonding non-bonding and anti-bonding), shown in Fig.2.7 (a), a Mott Hubbard gap opens on the antibonding band, in the solution of the Hamiltonian in (2.2). Here there are 2 possibilities depending on the values of U_d and Δ_{pd}, where $\Delta_{pd} = \epsilon_d - \epsilon_p$ is the anion cation charge transfer.In case $W < U_d < \Delta_{pd}$ we have a Mott Hubbard insulator, shown in Fig.2.7 (b). The other possibility, which is the case for cuprates, arises when $W < \Delta_{pd} < U_d$, in this case the material is a charge transfer insulator, shown in Fig.2.7 (c).

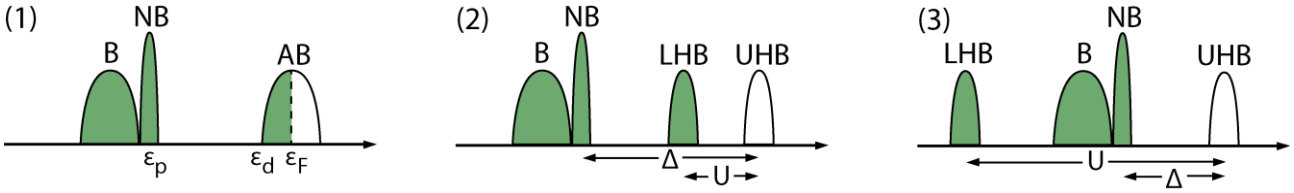

Fig.2.7 **a** Density of states for a calculation not considering the Coulomb repulsion *U* using a Hamiltonian similar to Eq.2.2. Three bands appear, bonding non-bonding and antibonding band. The result of this calculation is metallic. **b** Mott Hubbard insulator density of state. **c** Charge transfer insulator density of state.

2.3.2 Superconductivity

As previously mentioned, doping hole in the material, anti-ferromagnetism is suppressed and superconductivity appears at low temperature. The superconducting phase has a dome-like shape in the phase diagram, starting at p_{min} in the underdoped side and ending and p_{max} in the overdoped side. The maximal T_c is reached at the optimal doping p_{opt}=0.16. A widely used approximate formula to describe the shape of the superconducting dome in the phase diagram is: $T_c/T_{c,max}=1—82.6\ (p-0.16)^2$ [35], [36]. However this is a rough approximation. For example, as it can be seen in Fig.2.5 at p=0.12 there is a suppression of T_c. This doping is where the charge density wave is strongest (maximum T_{CDW}), and its competition with the superconductivity causes the suppression of T_c.[37]

The superconducting gap is anisotropic in the momentum space, and as stated earlier it was shown to possess *d*-wave (d_{x2-y2}) symmetry. This was understood in early studies using different techniques including ERS[38], [39], ARPES[22], [40], penetration depth[41] and phase sensitive measurements.[42] The gap can therefore be described by the *d*-wave (d_{x2-y2}) function, where the amplitude of the gap in the momentum space is given by: $\Delta(\boldsymbol{k}) = \Delta_0|\cos k_x a - \cos k_y a|/2$ However this function is a good representation of the superconducting gap only in the overdoped side of the superconducting dome. In the underdoped samples towards the antinode a deviation from the *d*-wave function was identified by ARPES. [43], [44] As it can be seen from Fig.2.8 in the antinodal side there is a deviation from the d-wave gap profile extrapolated from the nodal gap,

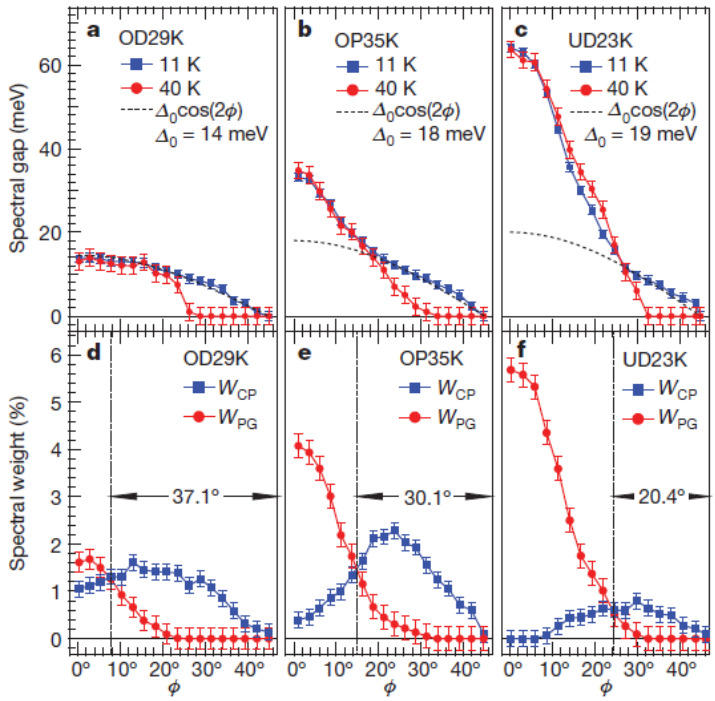

Fig.2.8 Deviation of the gap from the d-wave function in Bi2201 taken from Ref.[44]. In the upper panels the gap value is shown below and above T_c. In the lower panes the spectral weight associated with the superconducting gap W_{CP} is compared to the one associated with the pseudogap W_{PG}.

and this deviation becomes stronger in the underdoped samples. This deviation is commonly associated with the pseudogap, which coexists with the superconducting gap, and is usually referred as two gap behaviour. However the source of this deviation is controversial. There have been works reporting absence of any deviation in a wide range of doping, suggesting that the deviation may be due to cation substitution that it is sample specific.[45]

One of the problems that come with the two gap behaviour is the doping dependence of the superconducting gap. In the framework of the BCS theory there should be a simple proportionality relationship between the critical temperature and the gap value $T_c \propto \Delta$. However while this relation could hold in the overdoped side, it is not true in the underdoped side. In the underdoped side the antinodal gap increases with lower doping while the T_c decreases and this can be seen in Fig.2.9. In the strongly underdoped side showed in Fig.2.9 the antinodal gap increases with lower doping, while the nodal gap decreases. This opposite doping dependence is sometimes referred as two energy scale, and it also observed by other techniques such as Raman. [46]–[49] One may think that in the underdoped side the T_c is determined not by the antinodal, but by the nodal gap. However ARPES reported that in a wide range of doping the nodal gap is in fact constant. [2] As it can be seen from Fig.2.10 (d) the nodal gap is almost constant between $p = 0.076$ and $p = 0.19$, and it only decreases outside of this interval in the strongly underdoped and overdoped side. This furtherly complicates the problem, since in this region it seems that neither the nodal nor the antinodal gap follow the doping dependence of T_c, and it is therefore unclear what determines the critical temperature.

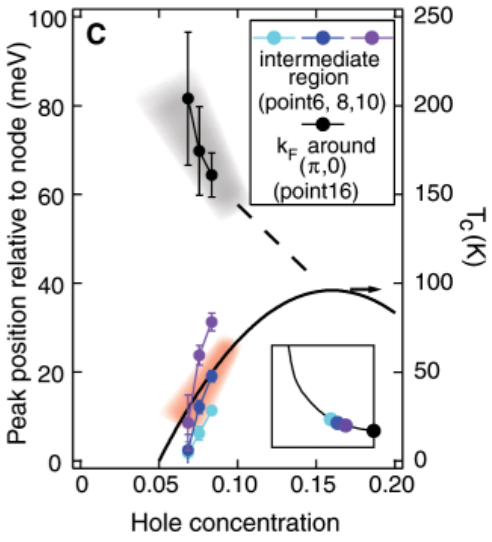

Fig.2.9 Doping dependence of the nodal and antinodal gaps in Bi2212 taken from Ref.[43]

Another antinodal effect in underdoped samples that is associated with the pseudogap is the confinement of Cooper pairs in the antinodal region with underdoping.[50] Here the idea is that due to the competition between superconductivity and the pseudogap, with decreasing doping the Cooper pairs are suppressed and then expelled from the antinode and this is consistent with the tunnelling[51], [52] and the ARPES data[53]–[55]. In this case, in the underdoped side the superconductivity is confined in the nodal and intermediate region.

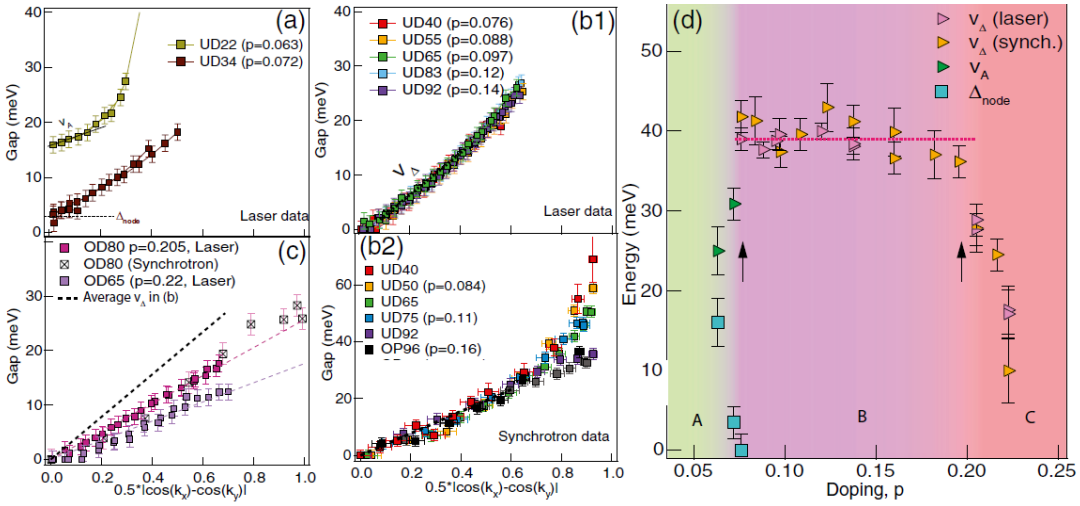

Fig.2.10 Taken from Ref.[2]. **a-c** Bi2212 ARPES gap profiles for samples of doping ranging from strongly underdoped to strongly overdoped. **d** Doping dependence of the nodal gap.

An important parameter for superconductivity is the superfluid density ρ_S. The ability of the superconductor to expel magnetic fields and the rigidity of the phase of the superconducting order parameter are determined by the superfluid density. The temperature over which the phase starts fluctuating is given by $T_\vartheta = \rho_S/m^*$. Where m* is the effective mass. In BCS superconductors ρ_S is equal to the density of electrons and therefore $T_\vartheta >> T_C$, meaning that as soon as the Cooper pair form the phase is stable, and that the fluctuation of the phase are irrelevant. On the other hand in cuprates it was soon understood that the superfluid density is low. Additionally in the underdoped side it was shown to scale with T_c in the so called Uemura plot. [56] Since ρ_S is not so high, in cuprates the phase stability temperature T_ϑ and the pair formation temperature are comparable and therefore phase fluctuation should be relevant.[57] Indeed superconducting fluctuations are observed above T_C, as it will be discussed in section 2.3.5, but it is not established if these are driven by fluctuation of the phase or of the amplitude of the superconducting order parameter.

As it was previously mentioned the nature of the pairing interaction in cuprates is currently unknown and object of debate. The previously mentioned observations regarding the isotope coefficient α (Fig.2.4, Ref[24]–[26]) seem to suggest that the phonon mediated coupling should be ruled out. However there are evidence that both ARPES and STS (Scanning Tunnelling Spectroscopy) spectra are affected by phonons[58] and strong anomalies are observed in the phonon spectra,[59] therefore electron phonon interaction cannot be completely ruled out.

A purely repulsive interaction could also lead to pairing, though this is not trivial. This can be seen in the framework of the Hubbard model in the unrealistic weak coupling limit ($U<<W=8t$, where U is the on-site electron repulsion W is the band width and t is the hopping parameter) as shown in Ref [60].Here a renormalized two particles vertex function $\Gamma(\mathbf{k})$ is used as interaction. In the case of purely repulsive interaction if $\Gamma(\mathbf{k})$ is sufficiently momentum dependant, a sign changing superconducting order parameter (where $\Delta(\mathbf{k})$ and $\Delta(\mathbf{k}+\mathbf{Q})$ have opposite sign) results. In this, interactions with small momentum transfer are pair breaking, but the one with large momentum

transfer (near **Q**) promote pairing. Interestingly in the case of antiferromagnetism a peak in *Γ* at the antiferromagnetic ordering vector **Q** = $\mathbf{Q}_{AF}$ is expected, [61] and this vector is also the perfect vector for scattering between the antinodal regions where the gap is the largest. This is striking even if the antiferromagnetic order disappears with doping. The reason being that even if the superconducting order disappears with doping it does survive in the form of dynamical magnetic fluctuations, as it was shown by inelastic neutron scattering and resonant X ray scattering.[62]–[65] However as stated earlier the source of pairing is still controversial.

2.3.3 Pseudogap

The pseudogap was firstly discovered by nuclear magnetic resonance as a reduction of the low frequency spin excitations, and was therefore initially thought to be a spin gap.[66], [67] It was subsequently observed by multiple techniques including *c*-axis optical conductivity[68], STS[69] and ARPES.[40], [70] Since its discovery the pseudogap was object of intense debate.[71] Two main kind of opposite theories existed at the center of the discussion, one attributing the pseudogap to a precursor state of superconductivity, where pairs are formed but lack long range coherence,[57] and the other attributing the pseudogap to a different order parameter than superconductivity.[72]–[74]

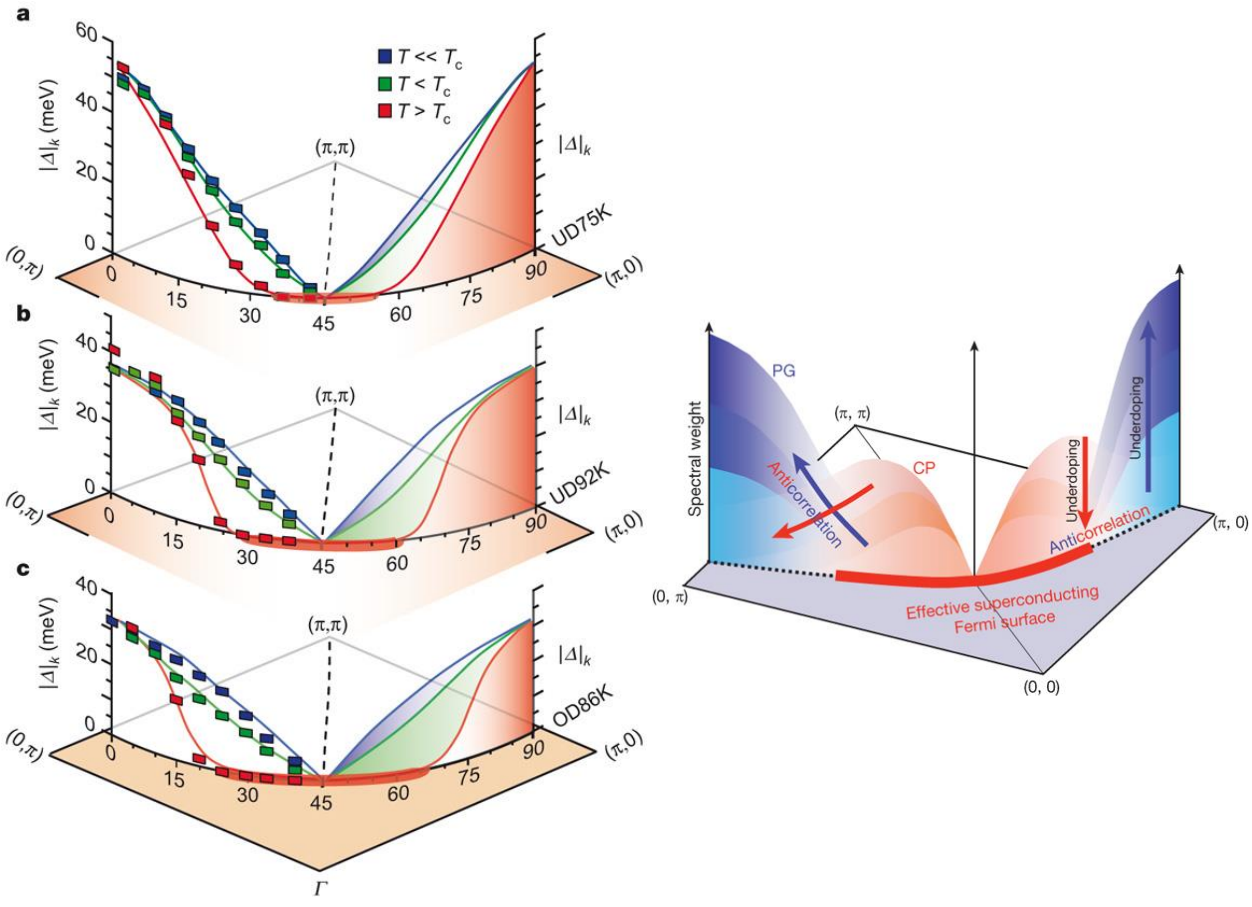

Fig.2.11 Pseudogap as seen by ARPES. Taken from Ref[75] and Ref. [44]

The pseudogap as seen by ARPES is shown in Fig.2.8 and Fig.2.11. Above T_C a gap persists in the antinodal region. The first particular feature of the pseudogap is that the Fermi surface is not completely gapped: only the antinodal region is gaped. The ungapped nodal region was named Fermi arc. [70] The concept of Fermi arc is highly unusual in classical physics, where the Fermi surface were considered to be a closed contour, that, no matter how complicated, could not terminate abruptly.

The pseudogap is an antinodal phenomenon and is stronger in the underdoped side. As seen in Fig.2.5 the pseudogap onset temperature T* increases with lower doping. Additionally with lower doping the maximum value of the pseudogap gap increases and the pseudogap expands towards the node, making the Fermi arc shrink,[2] and this can be seen in Fig.2.8 and Fig.2.11

More recent experimental ARPES studies seem to suggest that the pseudogap origin is to be attributed to a different order than superconductivity,[1], [76] and not to the formation of pairs, even though it is still unknown exactly what kind of order can be associated to the pseudogap. These experimental observations include the previously mentioned deviation from the *d*-wave gap [43], [44] or more generally the so called nodal-antinodal dichotomy [1], the non-monotonic temperature dependence of the size of the antinodal gap[76] and the breaking of particle hole symmetry.[77], [78] However this controversial issue is not yet resolved since contrasting and opposite results have also been reported. These include absence of deviation from the *d*-wave gap [45], [79] (which, as said before, is attributed to cation substitution, and regarded as material dependent), a smooth evolution of the pseudogap into the superconducting gap[69] and particle-hole symmetry.[80]–[82] In Fig.2.12 (d) the particle-hole symmetry breaking in Bi2201 is shown. Here the band dispersion is extracted above T* and below T_C and the back-bending momenta k_G below T_C is shown to be different from the Fermi vector k_F above T* indicating that the particle-hole symmetry is broken. Additionally, from this figure the coexistence of superconductivity with the pseudogap can be seen. The multiple features observed in the antinode below T_C (green and blue dots in Fig.2.10 (a) and (c)) cannot be explained by a superconducting gap alone. Instead the authors were able to reproduce these multiple features in calculations assuming coexistence of *d*-wave superconductivity and checkboard density wave, as shown in Fig.2.12 (e).

The relationship between the pseudogap (considered as a different order than SC) and the superconducting gap is commonly believed to be of competitive nature.[44], [83] In this picture superconductivity and the pseudogap coexist below T_C[84] and with decreasing doping the pseudogap becomes stronger in the antinode confining the Cooper pairs in the intermediate and nodal region.

2.3.4 Competing orders.

Several different competing orders have been observed in the phase diagram of cuprates, which break the symmetry of the crystal. The first of these that was discovered was the stripe order in

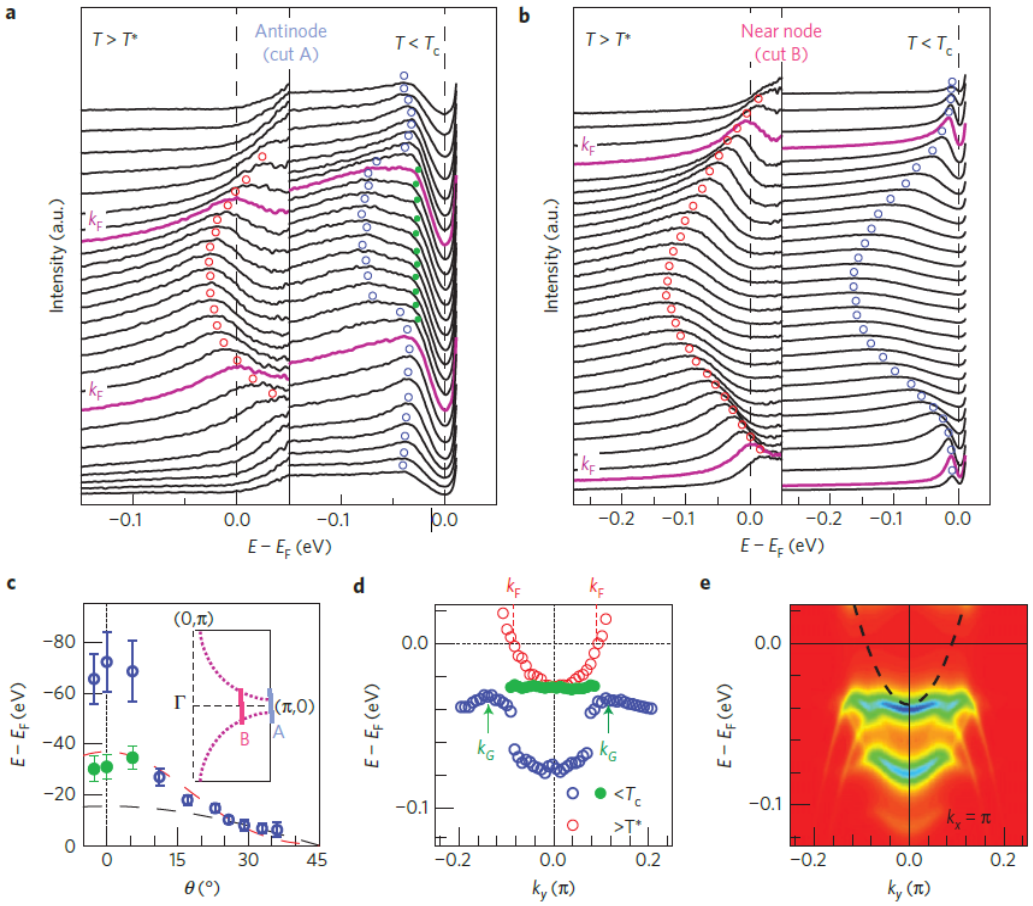

Fig.2.12 Taken from Ref.[78] **a, b** Antinodal and nodal Bi2201 ARPES spectra divided by the Fermi Dirac function. **c** Energy of the observed features. **d** Dispersion of the observed antinodal features. e Calculated band dispersion assuming coexistence of *d*-wave superconductivity and checkboard density wave

the $La_{2-x}Sr_xCuO_4$ LSCO family.[85] Doping the AFM Mott insulator produces holes on the Cu sites that can move through different Cu sites, but, doing so, they produce frustration of the spins of the electrons. To avoid this, the stripe order shown in Fig.2.13 (b) is formed. Here both charge and spin are modulated. The stripes are local AFM domains in which the order is reversed from stripe to stripe. The holes accumulate at the boundaries between stripes to reduce the spin frustration. Due to the reversal of the AFM order between stripes the spin modulation has double the periodicity of the charge modulation. The stripe order was shown to be stabilized by the Low Temperature Tetragonal LTT phase.[85]

The stripe order competes with superconductivity and this can be seen from the right panel in Fig.2.13 showing the phase diagram of LSCO. Here the maximum onset temperature T_m of the stripe order corresponds to the drop of T_C observed at x=1/8, indicating competition between the two orders.

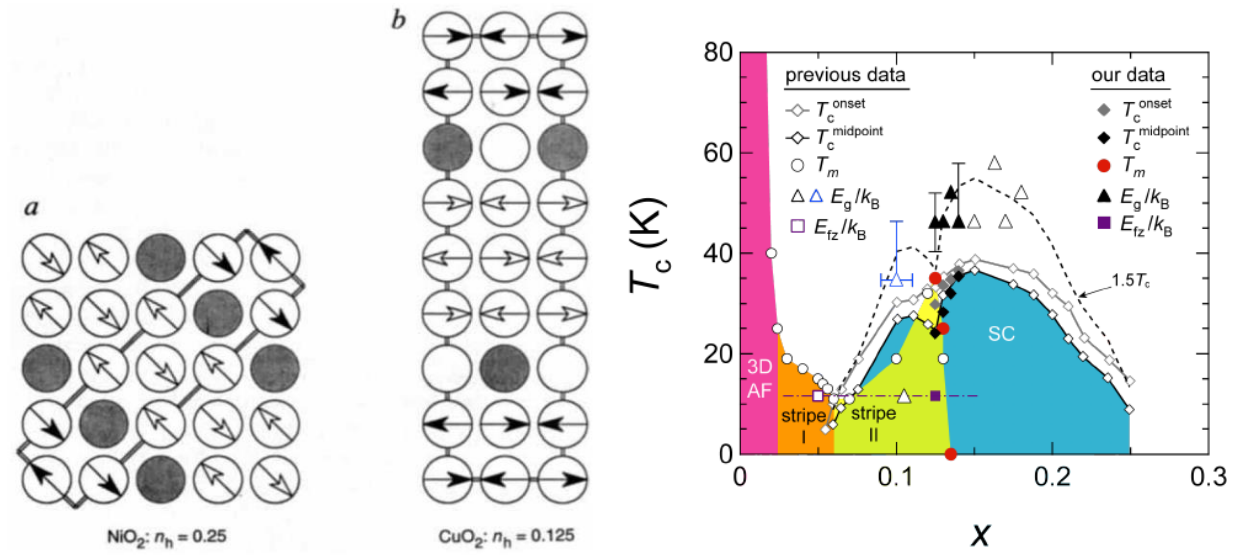

Fig.2.13 Taken from Ref. [85] and from Ref.[86] Representation of the stripe order in: **a** the parent compound La_2NiO4 and in **b** LSCO. Only the Cu sites are shown and the holes are represented with filled circles. **left panel** The phase diagram of LSCO.

A highly unusual feature of the stipes is that, even if they involve crystallization of the electrons, they stay metallic and even superconduct at low temperature. The material can be therefore viewed as a highly unusual crystallized superconductor.[87], [88]

For years the stripe order seemed to be confined in the LSCO family, until charge ordering was discovered in YBCO,[89] bismuth and mercury based cuprates.[90]–[92] Using X-ray scattering a short range incommensurate charge modulation was found, and it was shown to appear gradually between 200K and 100K. [93], [94] Unlike LSCO, here only charge is modulated, and there is no sign of spin modulation. This charge density wave was shown to compete with superconductivity, as the stripe order does, and, as in LSCO case, the dip where T_C is suppressed at p=0.12 corresponds to the maximum onset temperature of the CDW, as it can be seen in Fig.2.5. The modulation appears along two perpendicular directions along a* and b* axis. STM measurements showed that the CDW organizes in disordered domains where the modulation along a* or b* direction prevails.[95].

Another interesting and fundamental difference between the stripe order in LSCO and the CDW in other cuprates is that the modulation wavevector has an opposite doping dependence of the.[96] In LSCO the wavevector increases with doping, as it would in a real space driven behaviour, while in YBCO and Bi-based cuprates it decreases with doping, as expected in a reciprocal space picture involving vectors on the Fermi surface.

Theoretically a CDW with modulation in 2 directions is expected to cause reconstruction of the Fermi surface, where the Fermi arc could be half of the electron pockets that would form from the reconstruction. This has never been observed. However In YBCO with p=0.1, with magnetic field, quantum oscillation in Hall signal, with period 1/B were observed.[97] These point to a defined Fermi surface, and are not consistent with truncated Fermi arc. It is possible that this signal could

originate from a reconstruction of the Fermi surface caused by a biaxial CDW, though this was not confirmed.

The so called “quantum nematic liquid crystal” is yet another order that was reported in cuprates. Unlike the stripe order and the CDW order, nematicity does not break the translational symmetry, but breaks only the four-fold rotational symmetry. This nematic order was shown by transport measurements[98], [99] and by inelastic neutron scattering measurements.[100]

Interestingly some STS studies were also able to pick up nematicity. Here the O site STS sub-image shows, alongside the charge modulation, a *d*-wave form factor dFF-DW.[95], [101] Here according to the author, nematicity causes the oxygen sites along x and y directions to be inequivalent, and this gives a phase difference of π between the modulation on the Ox and Oy sites giving the dFF-DW. The obtained O site STS sub-image and the schematic of the dFF-DW are shown in Fig.2.14.

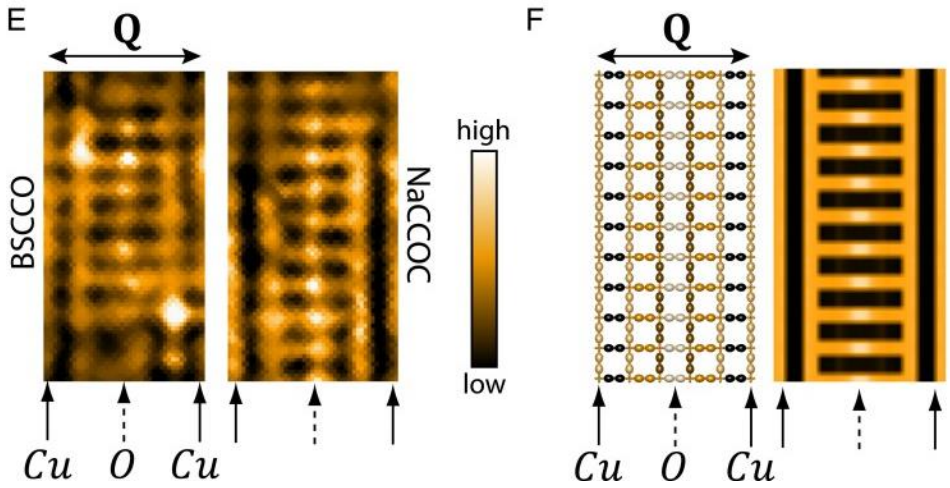

Fig.2.14 Taken from Ref.[101] **e** O site STS sub-image showing the dFF-DW in BSCCO and NaCCOC. **f** Schematic of the dFF-DW, the colour of the oxygen orbital represents the phase of the modulation. A phase difference of π exists between the modulation on the Ox and Oy sites.

Lastly a new exotic order may be present in cuprates. This would be the magnetic analogue of the charge nematicity, involving magnetic moments on the oxygen sites. Like nematicity this novel order would break rotational but not translational symmetry.[102]

2.3.5 Superconducting fluctuation

Signatures of pairing above T_C have been observed by many different techniques including transport and thermodynamical studies[103]–[106] and more recently by spectroscopic studies.[76], [107], [108] As discussed before, it is commonly believed that due to the low superfluid density of cuprates, pairing appears at a higher temperature than T_c, but that pairs lack long range phase coherence. Therefore these superconducting fluctuations are believed to be different than the normal BCS superconducting fluctuations, where the amplitude of the

superconducting order becomes zero at T_C causing the fluctuations. Instead in cuprates the amplitude of the pairing order would be non-zero above T_c and the phase disorder would be responsible of the absence of macroscopic superconductivity.[109] However it is still controversial whether the fluctuations in cuprates differ from the conventional fluctuations or not. Perhaps the most convincing evidence phase disorder scenario comes from the upper critical field deduced from Nernst effect[109] and torque magnetometry.[104] The upper critical field is supposed to become zero at T_c in case of vanishing pairing amplitude, but in these studies it was shown that the upper critical field remains large at T_c and above T_c, and this hints to the phase disorder scenario.

As previously mentioned, the pseudogap was interpreted as a state of performed pairs by some groups, and these studies showing pairing above T_c were thought to be supporting this idea. However the onset temperature of pairing was found to be smaller than T* and in some cases a different doping dependence (decreasing in the underdoped side) was shown, and this can be seen in the phase diagram of LSCO and $Bi_2Sr_{2-y}La_yCuO_6$ obtained from torque magnetometry and Nernst effect measurements in Fig.2.16.

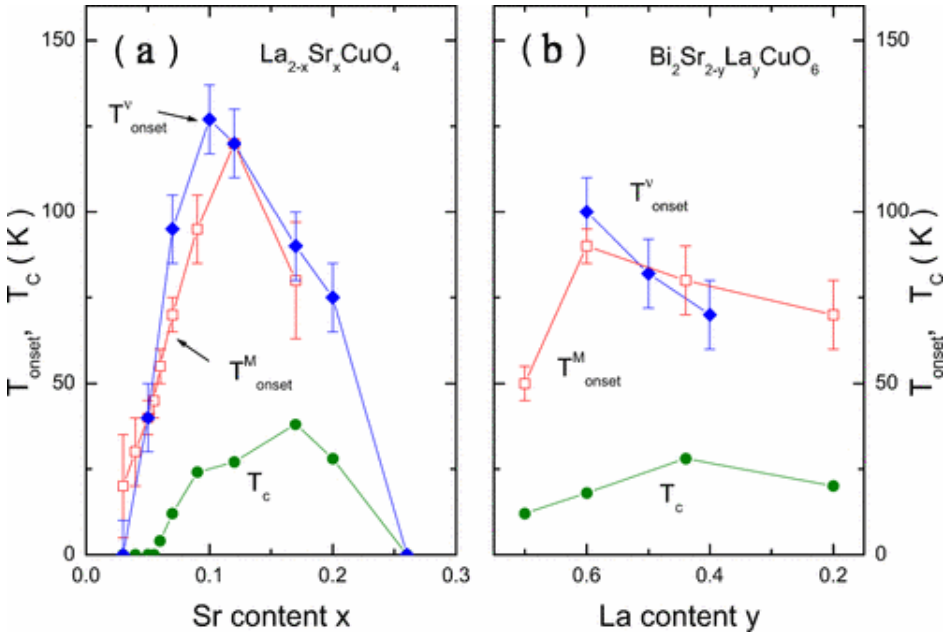

Fig.2.16 Taken from Ref.[104] Doping dependence of the onset temperature of superconductivity in LSCO and $Bi_2Sr_{2-y}La_yCuO_6$ where T^v comes from Nernst effect and T^M from torque magnetometry measurements.

Pairing above T_C is inconsistent with the Fermi arc: if pairing exists a *d*-wave gap should be observed. However early studies showed a linear dependence of the Fermi arc length with temperature[110] and this was interpreted as effect of the strong scattering that exist above T_c hiding the *d*-wave gap.[111] If the scattering rate exceeds the value of the gap, the ARPES spectra appear ungapped, hiding therefore the *d*-wave gap at the nodes where it is smaller, and creating a false Fermi arc. Quantitative analysis of ARPES data proved instrumental in solving this issue,[76],

[107] showing that below the pair formation temperature T_{pair} there is indeed a fully opened *d*-wave gap while at $T_{pair}<T<T^*$ only the antinodal region is gapped and real ungapped Fermi arc are present.

An exceptional case of pairing at extremely high temperature is constituted by the pump and probe experiments in YBCO shown in Ref.[112] Here using laser pulses, superconductivity was induced far above T_c, and up until room temperature. Here the doping dependence of the onset temperature of this induced superconductivity is increasing with lower doping, and follows the pseudogap T*doping dependence. This study may constitute a case in favour of theories that suggest pairing as the origin of the pseudogap, or could point to some kind of connection between the pseudogap and superconductivity, though this is controversial.

2.3.6 Strange metal

The strange metal phase appears at intermediate doping in the "normal" state of the cuprates, as indicated by the violet area in the phase diagram in Fig.2.5. Because of strong correlation effects, even though metallic behaviour is observed, the quasiparticles are absent, and this was shown with in-plane resistivity[113] and Hall resistivity measurements.[114] In normal metals the resistivity saturates at high temperature since the mean free path *l* of the electron, determined by electron phonon coupling, can decrease as low as the atomic spacing. However in cuprates the in-plane resistivity remains linear up until as high temperature as measured (800K) [113]. At such high temperature the calculated *l* would be smaller than the de Broglie electron wavelength λ and this would violate the Heisenberg uncertainty principle.

A theory that was partially successful in describing these experimental anomalies is the "marginal Fermi liquid" theory.[115] The idea is that the electron in the Fermi gas are coupled to a continuum of excitation. This continuum of excitation is assumed as spatially featureless and has a spectral density that is constant for $\omega>T$ but proportional to T for $\omega<T$. This was indeed confirmed by ARPES measurements but only in the nodal region, while the antinodal region behaves incoherently.[116]

Another idea that was proposed to explain the strange metal is that the strange metal phase originates from a quantum critical wedge associated with a quantum critical point QCP under the superconducting dome and this is shown in the phase diagram in Fig.2.5. The QCP is associated with a phase transition between an ordered state and a disordered phase, as a function of a tuning parameter (doping pressure etc.). In the phase diagram with the tuning parameter and temperature, above the QCP a wedge should open, and the strange metal phase was proposed to be originating from this wedge. One problem of this idea is that the quantum critical wedge should disappear at high temperature but the strange metal phase is observed up to extremely high temperature.

2.3.7 Overdoped regime

Increasing the doping until the overdoped regime, signatures of a real Fermi liquid, consistent with the one electron band theory, start to appear. This is shown in the phase diagram in Fig.2.5 by the white area. In this region quantum oscillations are consistent with a large Fermi surface.[117] ARPES shows that a coherent peak is present on the whole fermi surface, including in the antinodes which are incoherent at lower doping, supporting the recovery of a real Fermi liquid.[118], [119]

Interestingly in this regime inelastic neutron scattering indicates that the spin fluctuation disappear gradually. The intensity of the spin excitation peak was shown to decrease linearly with T_c with increasing doping,[120] indicating that superconductivity and spin fluctuations may have a cooperative relationship and this could be a point in favour to the idea of spin fluctuation as pairing glue.

2.4 Multilayer cuprates

The multilayer cuprates are another fascinating aspect of the field. The main reason for this is that the T_c of the cuprates strongly depends on the number of Cu-O plane per unit cell *n*. In Fig.2.16 the crystal structure of some example families of multilayer cuprates is shown. Going from the left *n* is increased from one, in the single layer member of the family, to five. Here the difference in crystal structure with increasing number of layers can be seen. In the single layer component the copper atom forms an octahedron with the neighbouring oxygen atoms. The double layer component has two identical CuO_2 layers in which the copper atoms are in pyramidal configuration with the neighbouring oxygens. Finally for $n \geq 3$ the interesting situation where unequal CuO_2 layers are present arises. The layers next to the charge reservoir layer have coper atoms in the pyramidal configuration, as in the double layer component, and these layers are named Outer Planes OP. On the other hand the layers that are not adjacent to the CRL are called inner planes IP, and these have the copper atoms in planar configuration with no apical oxygen. The two kinds of planes are chemically inequivalent. The fact that the inner planes are not directly adjacent to the CRL makes it more difficult for carrier coming from the dopant atoms in the CRL to reach them. As a result the inner planes are less doped than the outer planes which are adjacent to the CRL. Therefore for $n \geq 3$ the interesting situation where layers with different doping coexist in the same samples arises. In this situation one difficulty is to determinate the layer doping of the two kind of planes OP and IP, which is different from the average sample doping. One way to measure this layer doping comes from the Cu NMR Knight shift peaks, which is sensible to the carrier concentration in the surrounding of the copper atom. A linear empirical relation between the hole concentration *p* and the temperature dependent spin part of the Knight shift K_s was proposed.[9]

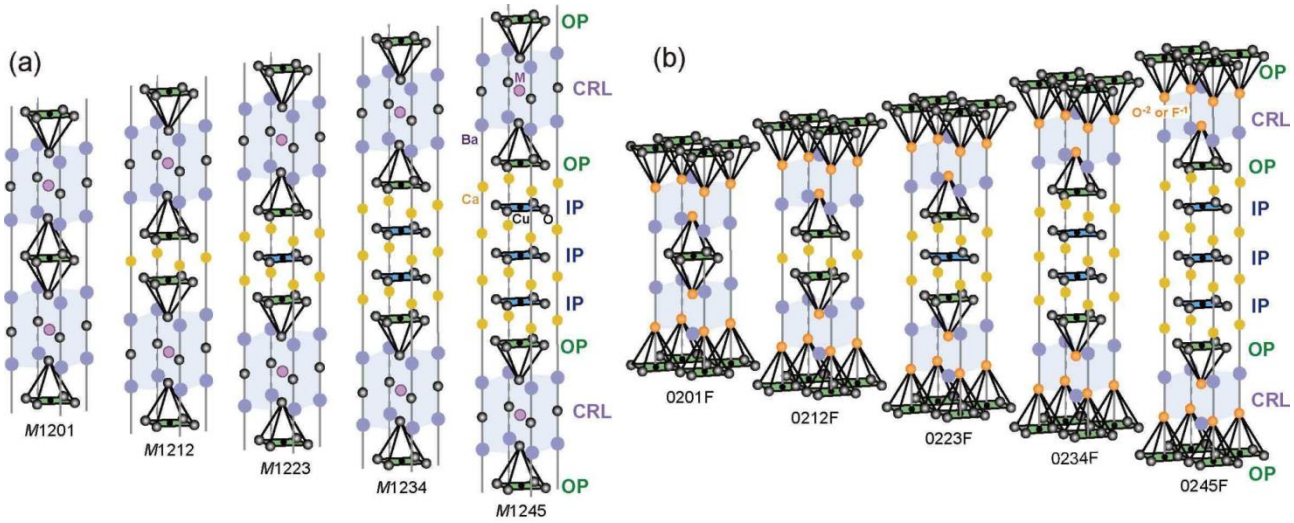

Fig.2.16 Taken from Ref.[9] Examples of crystal structure of families of cuprates with different number of copper plane *n* per unit cell. **a** $MBa_2Ca_{n-1}Cu_nO_{2n+2+\delta}$ (M=Hg, Tl, and Cu) M12(*n*-1)*n* crystal structure. **b** $Ba_2Ca_{n-1}Cu_nO_{2n}(F_yO_{1-y})_2$ 02(*n*-1)*n* crystal structure.

Multilayer band splitting is another effect that is expected to arise with increasing number of CuO_2 layers. According to $t–t'–t''–J$ model calculations, the bands of different layers should hybridize forming a number of bands equal to the number of copper layers.[121] Therefore in the double layer cuprates, two bands should appear: a bonding and an antibonding band, and this was indeed observed by ARPES. [122] In the case of $n \geq 3$ the doping imbalance between the OP and IP is the main source of band splitting. In the case of the triple layer for example a large splitting exists between the OP and IP bands.[123] Here only two band were observed, but the OP band was shown to be much broader than the IP band, and therefore two OP bands could be overlapping and not resolved.

The critical temperature of the cuprates strongly depends on the number of CuO_2 layers per unit cell. T_c increases when *n* increases from *n*=1 to *n*=3, where it reaches its maximum, and then decreases for $n \geq 4$ [5] and this trend is shown in Fig.2.17. Up to date the cause of this T_c enhancement is not clear, with several possible factors being proposed. Firstly the tunnelling of Cooper pairs between different layers could enhance T_C.[6] The next-nearest neighbour hopping parameter t' was also shown to correlate with T_C. This correlation is valid both considering only single layers cuprates and considering cuprates with different number of layers, since t' increases with the number of layers.[7] Finally another factor that could greatly enhance T_C is the disorder protection that the OP offers to the IP.[8] Disorder next to the apical oxygen was shown to be a drastic cause of T_C suppression, causing buckling of the OP. Disorder coming from the dopant could appear in principle anywhere in the unit cell, however the absence of any apical oxygen in the IP makes disorder next to this layer much less severe than disorder next to the apical oxygen of the OP layer. In $n \geq 4$ cuprates with increasing *n* the AFM order becomes stronger[9] and this could be the reason why T_C decreases after *n*=3.

Since the doping level of the OP and IP is different it is possible that two different T_C may be associated with the two kinds of layers. It is therefore unclear if superconductivity appears at the same temperature on the IP and on the OP or not. It is possible that the superconductivity originates on one of the two kind of layers and then propagates in the other layer or drives it to be superconductive by proximity effects.[9], [124]

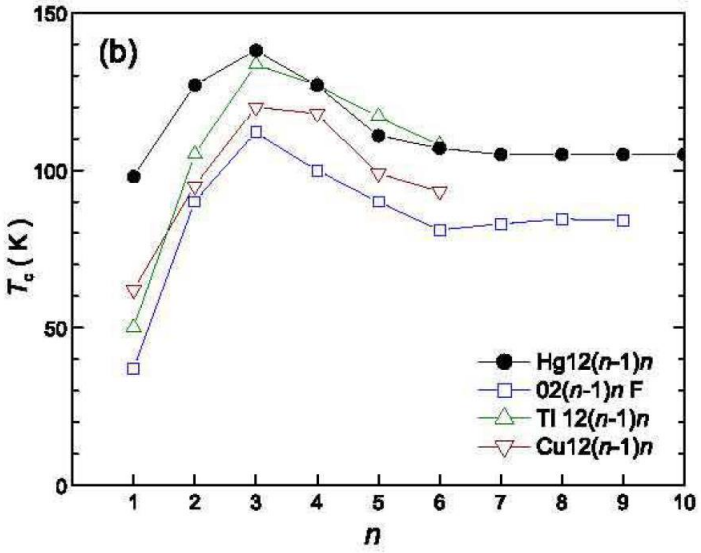

Fig.2.17 Taken from Ref.[9] Relationship between T_C and *n* for different families of multilayer cuprates.

2.5 BSCCO

The bismuth strontium calcium copper oxide, or BSCCO (pronounced "bisko"), are a family of high-T_C cuprate superconductors. They share a common chemical formula $Bi_2Sr_2Ca_{n-1}Cu_nO_{2n+4}$ where *n* is the number of CuO_2 layers per unit cell. *n* can go from 1 to 3, from the single to the triple layer component. The three component of the family are summarized in Table 2.1 and their crystal structure can be seen in Fig.2.18.

Chemical formula	Notation	Max. T_C (K)	*n*	Crystal structure
$Bi_2Sr_2CuO_6$	Bi-2201	20	1	Tetragonal
$Bi_2Sr_2CaCu_2O_8$	Bi-2212	95	2	Tetragonal
$Bi_2Sr_2Ca_2Cu_3O_{10}$	Bi-2223	110	3	Tetragonal

Table 2.1 Summary of the BSCCO

In the present work we focused on the double layer Bi2212 and on the triple layer Bi2223.

The BSCCO are hole doped cuprates and their hole content can be modified by adding excess oxygen. In this case the chemical formula becomes $Bi_2Sr_2Ca_{n-1}Cu_nO_{2n+4+\delta}$ where δ is the excess oxygen content. One advantage of the BSCCO is that their oxygen content is stable at room temperature and ambient pressure. As other cuprates the BSCCO are almost 2D materials, and their layers are only weakly bound to each other by Van der Waals forces. This makes these samples extremely easy to cleave, and therefore they have the advantage that it is easy to obtain a clean surface. As described in the previous section, going from the single to the triple layer material the configuration of the copper atoms with the neighbouring oxygen changes, and this can be seen in Fig.2.18. The copper atom form octahedron with the neighbouring oxygen in the single layer Bi2201, are in pyramidal configuration in the double layer Bi2212 and are in pyramidal configuration or in planar configuration, on the OP and IP respectively, in the triple layer Bi2223. The crystal structure of the BSCCO is tetragonal, and they belong to the D4h group (*I*4/*mmm*). The BSCCO unlike other cuprates do not undergo structural transitions at low temperature. The *a* and *b* axis have the same length 5.4Å, which is also common for all the BSSCO from the single to the triple layer. The c-axis on the other hand increases with *n* and is 30.8 Å and 37.1 Å in Bi2212 and Bi2223 respectively.[125]–[127] The BSCCO are rather inhomogeneous materials as compared for example to YBCO. The BiO layer are buckled and periodically modulated along the *b* axis, with an incommensurate period of 4.8*b*. [128] This modulation causes ghost images of the bands to appear in the ARPES spectra of BSCCO.[129]

ARPES and Raman share the requirement of a good sample surface and therefore the BSCCO, being extremely easy to cleave, are suitable samples for these techniques. The surface in these samples is non-polar which is a requirement for ARPES. The inhomogeneity of these samples

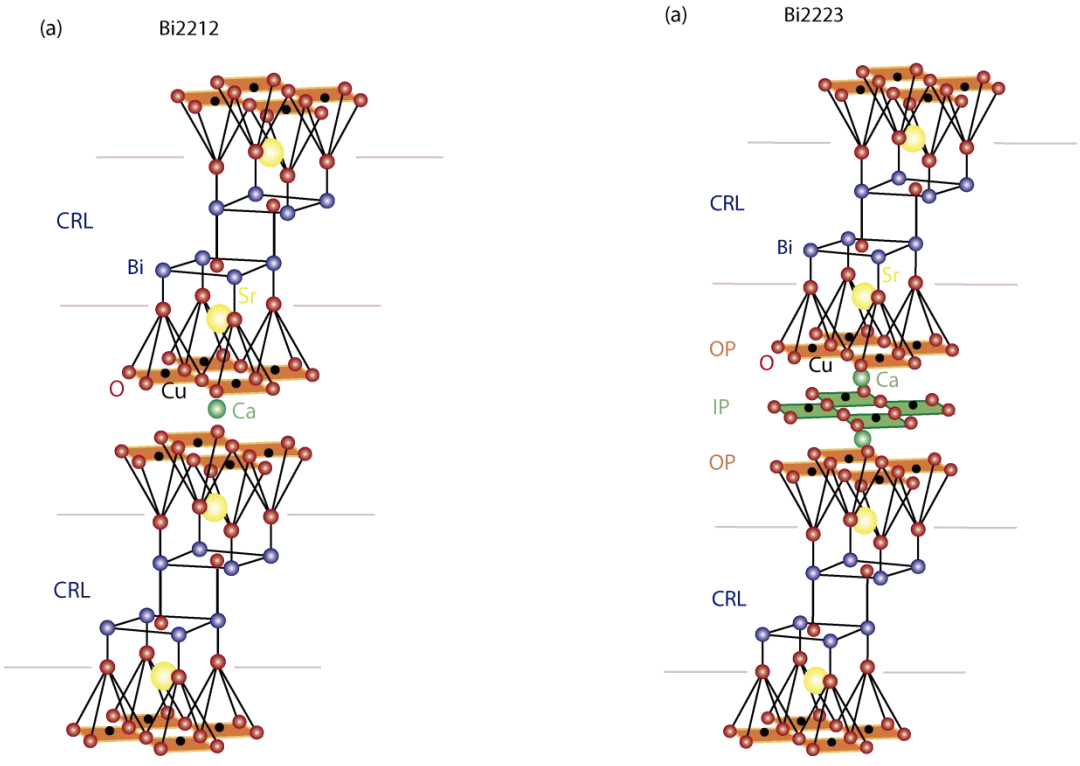

Fig.2.18 Crystal structure of **a** the double layer BSCCO Bi2212 and **b** the triple layer BSCCO Bi2223

however, is a disadvantage and may broaden the spectral features. The modulation of the BiO layer is also a disadvantage.

Bi2212 and Bi2223 are multilayer cuprates and, as discussed in the previous section, multilayer band splitting is expected to occur. In the double layer Bi2212 the two identical layer bands hybridize, forming a bonding and an antibonding band.[122] The triple layer Bi2223 has unidentical CuO_2 layers, two OP and one IP, who do not contain the same amount of carrier. The doping imbalance between the two kind of layer has been investigated by NMR and the layer doping has been extracted (p(OP)≈0.203 and p(IP)≈0.127).[130] Here the doping imbalance between the layers was found to be much larger than the one in other triple layer cuprates like Hg1223. The band splitting in Bi2223 was observed by ARPES,[123] and a large splitting was revealed between the IP and OP bands, however only a single OP band was found, which was very broad and was therefore suggested to be composed of 2 unresolved OP bands. More importantly the superconducting gaps of the two bands were found to have two distinct values, and this is shown in Fig.2.19. The difference in the value of the superconducting gaps is reasonable considering the different doping in the two layers.

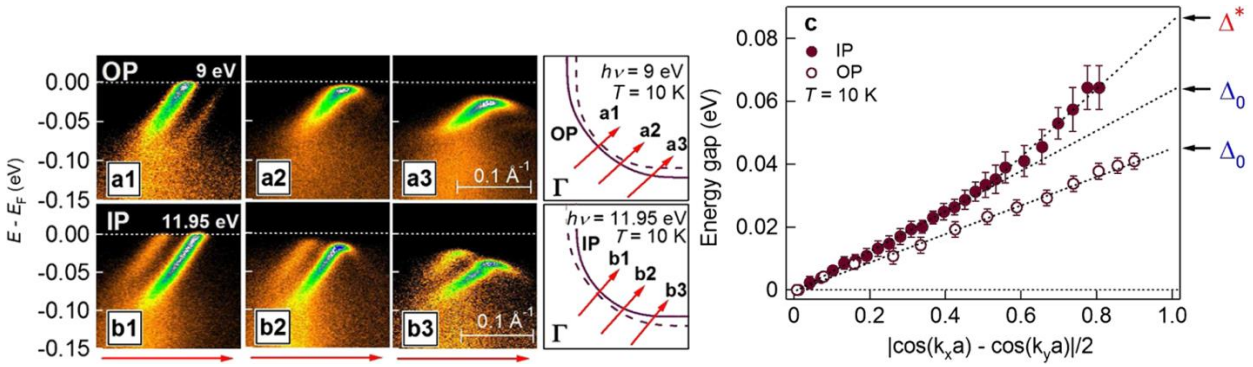

Fig.2.19 Taken from Ref. [123] **a,b** ARPES cuts at 10K going from the node (**1**) to the antinode (**2**), in **a** and **b** a different photon energy is used. **c** OP and IP extracted gap value momentum dependence.

The gap is larger in the underdoped IP than in the OP, additionally the IP gap shows a larger deviation from the *d*-wave function extrapolated from the nodal gap (dashed line leading to Δ_0 in Fig.2.19.) The greater gap deviation in the IP is consistent with the one found in the underdoped double layer components, that was discussed in section 2.3.2.

One particularity of Bi2223 is that T_C does not decrease in the overdoped side. This was uncovered by determining the *c*-axis of samples with various doping by X-ray diffraction XRD.[131] Since the *c*-axis of the BSCCO decreases with increasing oxygen content this parameter is a good indicator of the sample doping. Here it can be seen that with decreasing *c*-axis (increasing doping) the T_C of Bi2223 does not decrease from the optimally doped sample, unlike the T_C of Bi2212. The T_C reaches the maximum value at the optimally doped sample and then saturates. Up to date it is unclear what causes the constant T_C in the overdoped side of Bi2223, however this is most likely a multilayer effect. Unfortunately many factors may come into play in the determination of the triple layer cuprates T_C, like the protection of the IP from disorder, the tunneling of Cooper pairs

between layers etc., and additionally it is not certain that the triple layer gaps have the same doping dependence shown by the double layer. Therefore this problem cannot probably be solved until more clarity is made regarding the triple layer cuprates.

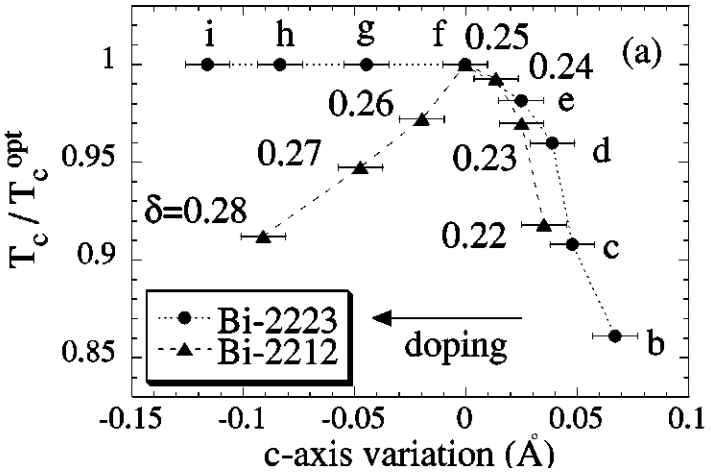

Fig.2.20 Taken from Ref. [131] Renormalized T_C potted against the *c*-axis variation from the optimally doped sample for Bi2212 and Bi2223 samples with various doping.

2.6 Previous Raman Experiments

The cuprates have been extensively studied by Raman spectroscopy. Raman was one of the techniques that were instrumental in determining the *d*-wave gap function in the early days of the

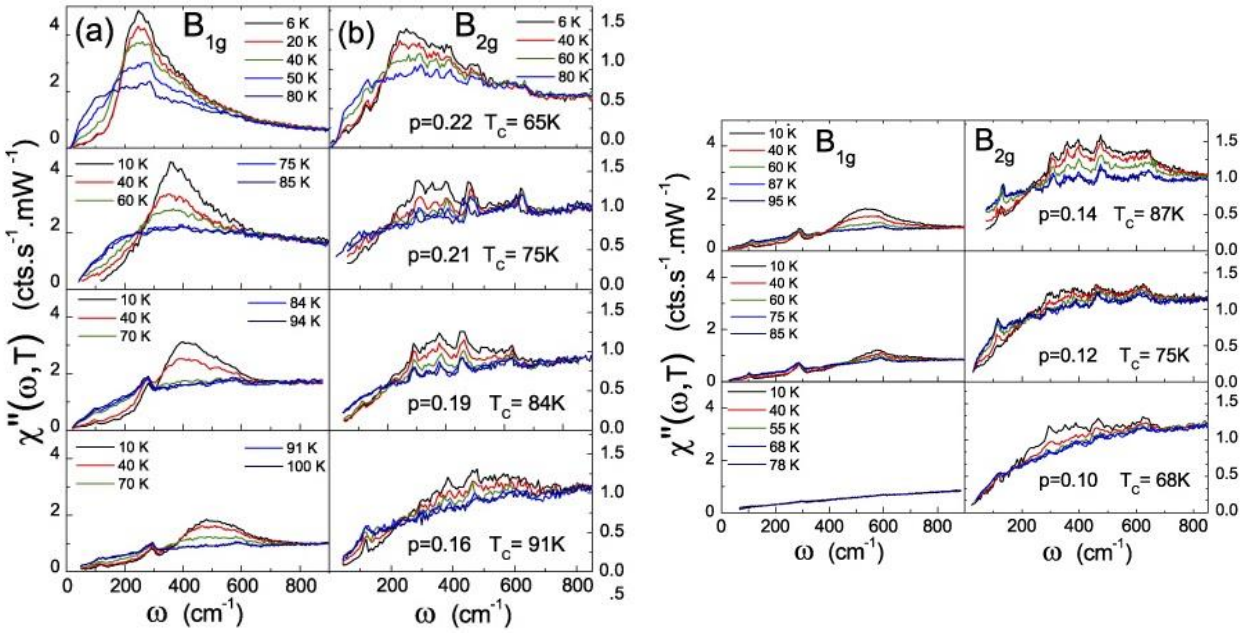

Fig.2.21 Taken from Ref.[132] Temperature dependence of the Raman spectra. **a** and **b** Raman spectra, of Bi-2212 single crystals for several doping levels in B_{1g} (antinodal) and B_{2g} (nodal) geometries.

cuprates. [38], [39] In these early studies it was shown that if the gap has a *d*-wave symmetry, the intensity of the B_{2g} nodal probe has a linear dependence in ω, while the antinodal B_{1g} probe has a cubic dependence in ω.

In Fig.2.21 the B_{1g} and B_{2g} Bi2212 Raman spectra are shown for samples of various doping. By cooling the sample below T_C a gap appears at low frequency and a peak at higher frequency, and these are the Raman signatures of superconductivity. The loss of spectral weight at low frequency is caused by the opening of the superconducting gap, while the peak is a pair breaking peak, associated with the breaking of a Cooper pair and a transition across the superconducting gap.

The nodal B_{2g} and antinodal B_{1g} superconducting pair breaking peaks in Raman have a different doping dependence that can be seen in Fig.2.22. This different doping dependence is also observed in other techniques like ARPES, and is commonly known as two energy scale[46]–[49]. However there are differences in the two energy scale seen by ARPES and Raman. The antinodal B_{1g} Raman peak monotonically increases going towards lower doping. This same doping dependence is found in the antinodal ARPES gap Δ^* as seen in Fig.2.9. However the antinodal ARPES gap is not commonly associated with superconductivity, since it is in fact a deviation from the *d*-wave function normally associated with the pseudogap, in the two gap pictures discussed previously. The nodal ARPES gap Δ_0 , which is associated with superconductivity, stays constant for a wide range of dopings. Therefore an interesting question is why the pair breaking antinodal B_{1g} Raman peak energy increases with lower doping while the nodal ARPES gap Δ_0 remains constant? One possibility is that the energy of the superconducting gap is partially enhanced by the pseudogap, however this is just a speculation at this point. One way in which the pseudogap certainly influences the B_{1g} Raman peak is by suppressing its intensity in the underdoped region, as it can be seen in Fig.2.22 (b). This is due to the fact that the pseudogap confines the Cooper pairs in the nodal region at low doping[50] and this causes the gradual disappearance of the B_{1g} peak. The nodal B_{2g} peak intensity on the other hand stays constant. The B_{2g} Raman peak energy doping dependence follows the superconducting dome, as shown in Fig.2.22. However the nodal ARPES gap Δ_0 does not follow precisely the dome, since, as said before, it is constant in a wide range of dopings, and decreases only in the strongly overdoped or underdoped side, as seen in Fig.2.10. This is therefore another discrepancy between the nodal Raman and ARPES probes, and one may wonder why the former follows the superconducting dome even if the gap is constant. In the underdoped side this may also be due to the confinement of Cooper pairs in the nodal region caused by the pseudogap. If superconductivity is confined more and more towards the node the effective gap that must be considered for the Raman B_{2g} peak may decrease, even if the gap slope Δ_0 does not change.

Bi2212 [48], [49], [133]–[135] and the other double or single layered cuprates [46], [47], [136] have been studied extensively by Raman, however this is not the case for the triple layer cuprates. Previous works on the triple layered cuprates are mostly quite old [137]–[141], but most importantly, no signature of the double superconducting gap due to the two inequivalent layer IP and OP has been found so far. The difference in energy between the IP and OP reported by ARPES in Bi2223 is quite large, [123] and therefore a signature of the double gap should be observed in

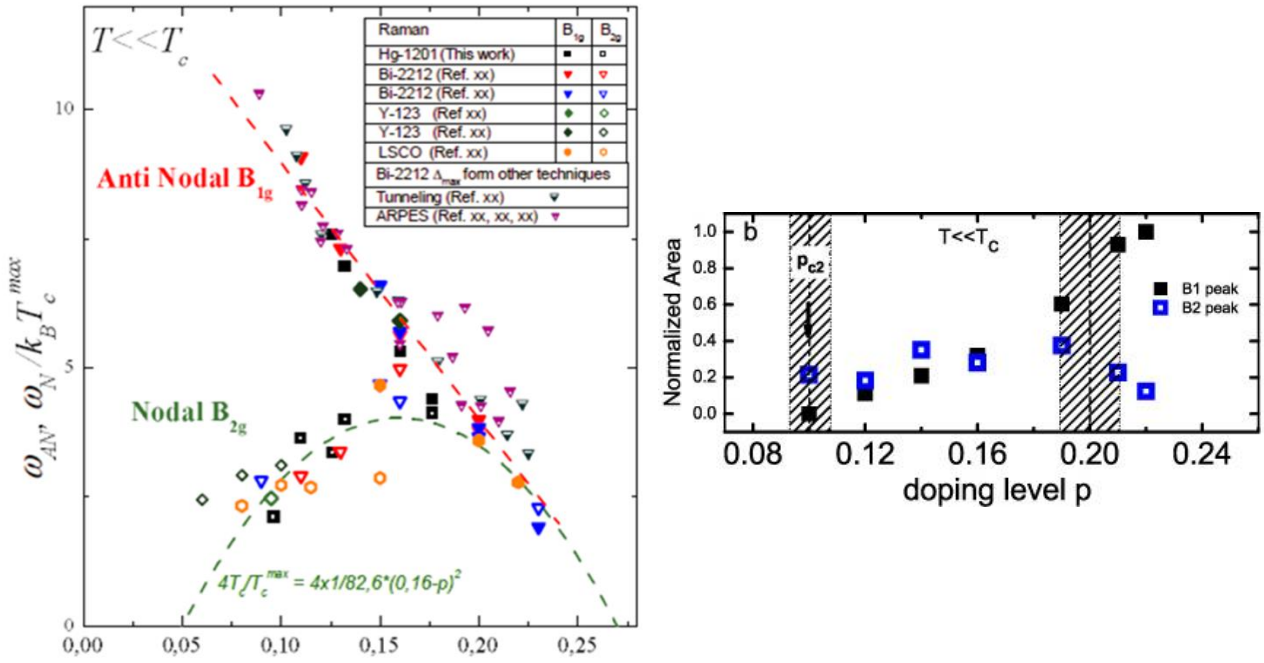

Fig.2.22 Taken from Ref. [47], [142] **a** Renormalized nodal B_{2g} and antinodal B_{1g} energy of the superconducting pair breaking peak seen by Raman, for various single and double layer cuprates. **b** Doping dependence of the intensity of the B_{1g} and B_{2g} Raman pair breaking peak.

principle, however no such signature has been previously found. This may be due to sample quality and instrumental resolution limits.

In Ref. [47] it was shown that dividing the peak energy by the maximum sample T_c causes the doping dependence of many single and double layer cuprates B_{1g} and B_{2g} peak energies to collapse on a universal doping dependence, which is shown in Fig.2.22 (a). In this plot no triple layer cuprates have been inserted. A signature of the double gap of the triple layer cuprates has not yet been shown by Raman, therefore even if the triple layer were added in this plot, it would be of little significance to plot an energy that is a mixed contribution of two gaps of different values coming from two layers with different doping. However if a signature of the double gap was to be observed by Raman and if the correct layer doping was to be used, it would be interesting to know if the triple layer Raman energy does scale or not on this universal doping dependence.

2.7 Previous Raman calculations

Previous Raman calculations are mostly base on the kinetic theory, and were quite successful in reproducing the ERS spectra of cuprates. The early calculations showed that the B_{1g} peak appears at 2Δ, where Δ is the maximum gap. Additionally, as mentioned before, these calculation proved instrumental in showing the *d*-wave gap anisotropy, and showing how this gap function gives a B_{2g} intensity linear in ω and a B_{1g} cubic in ω.[38], [39]

One challenge for the following calculations was to reproduce the two energy scale that was discussed in the previous section. Sacuto group was quite successful in this. [47], [49], [142], [143] In these calculations the Raman susceptibility was calculated as:

$$\chi''_{B_{1g}B_{2g}}(\Omega) = \frac{2\pi N_F}{\Omega}\langle \gamma^2_{B_{1g}B_{2g}}(\phi)(Z\Lambda)^2(\phi)\frac{\Delta^2(\phi)}{\sqrt{\Omega^2-\Delta^2(\phi)}}\rangle \qquad (2.3)$$

Where N_F is the sensity of states at the Fermi level, γ is the B_{1g} or B_{2g} Raman vertex, ϕ is the angle in the momentum space, and the braket describes the integration on the Fermi surface. Here the gap shown in Fig.2.23 was assumed. In these calculations the assumptions on the quasiparticle spectral weight $Z\Lambda$ are fundamental to obtain the two energy scale correctly. Following the consideration of the confinement of the Cooper pairs in the nodal region with lower doping the $Z\Lambda$ profile shown in Fig.2.23 bottom left panel is assumed. This assumed profile gives more intensity to the nodal area and suppresses the antinodal intensity. This assumption gives the two energy scale as it can be seen in the results in Fig.2.23 right panels. Here the energy doping dependence is opposite for B_{1g} and B_{2g} and the B_{1g} intensity decreases with lower doping, as in the experimental spectra. However additional assumptions on the gap doping dependence must be made. In this work in Ref.[142] a simple *d*-wave gap, increasing with lower doping was assumed. The increasing antinodal gap is a requirement to obtain an increasing B_{1g} energy, and this is connected to the problem of the ARPES antinodal gap discussed in the previous section: if Δ^* is connected with the pseudogap, why is it necessary to assume its doping dependence (increasing

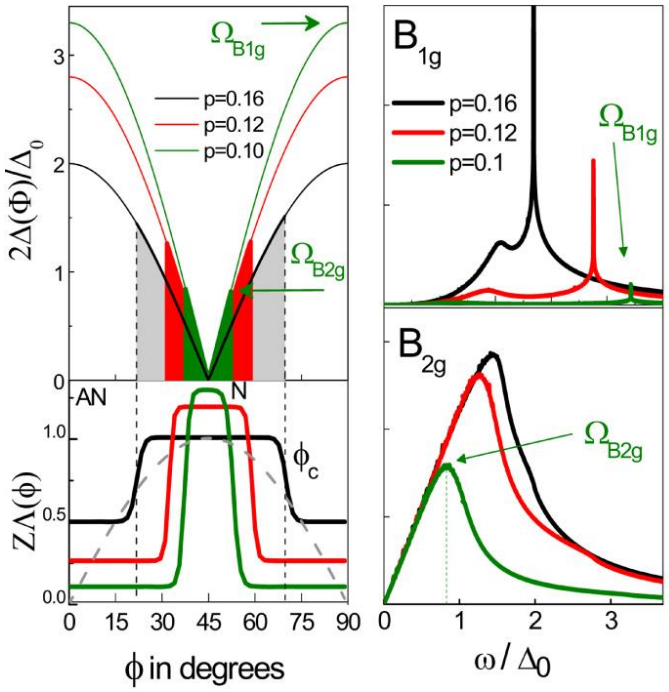

Fig.2.23 Taken from Ref.[142] On the left the assumed gap function and quasiparticle spectral weight is shown. On the right the calculated B1g and B2g Raman spectra.

with lower doping) to calculate correctly the pair breaking (superconducting) peak position in B_{1g} Raman configuration? As discussed before a possible explanation is that the pseudogap may influence the superconducting energy, though this is just a speculation at this point.

Previous calculation were performed to reproduce mainly single or double layer cuprates, So far no Raman experimental evidence of the double superconducting gap of triple layer cuprates has been presented, and therefore there was no need to calculate the Raman spectra of a triple layer cuprates with a double superconducting gap. It would be therefore interesting to calculate a triple layer cuprate Raman spectra originating from a double superconducting gap.

2.8 Purpose of this work

Since, as discussed in the previous section, the double superconducting gap of Bi2223 was observed by ARPES,[123] but not by Raman. Therefore the center of this work is the Raman measurement of Bi2223 samples, with the main goal of finding a Raman signature of this double gap. This would be the first observation of a Raman signature of the double gap, not only in Bi2223, but also in cuprates. Such a observation could help clarify the complex situation of the multilayer cuprates, and give us hints on how the layers interact with each other, or which parameter enhances the T_C, or how the pseudogap modifies in the case of multiple layer cuprates and how it affects superconductivity. Since it is possible to study easely the temperature dependence of the Raman spectra, it would be interesting to observe if one of the two gaps opens at a higher temperature due to the different doping of the layer, or if some intereaction between the two layers occurs, giving superconductivity at the same temperature. An added bonus in exploring such a triple layer cuprate is that we have the additional advantage that we can study multiple doping levels in one sample.

The second goal of this work is to reproduce Bi2212 and Bi2223 samples Raman spectra using the experimental ARPES data as an input. Starting from experimental ARPES data could help giving a better reproduction of the Raman spectra whose experimental shape are not well reproduced by previous calculations using the kinetic theory. In addition this could help to clarify the differences in how Raman and ARPES wiew the two energy scale and understand if there are inconsistencies between the two probes. Finally, studying multiple Bi2212 samples allows us to establish the calculation method, and verify its validity, so that we may apply it on the triple layer Bi2223, which is the main focus of the experimental part of this study.

For the Bi2223 calculation case, since a double superconducting gap is observed by ARPES on the IP and OP bands, we are interested, not only in reproducing the experimental spectra, but also in calculating the separate contribution of these two bands, and investigate if these two band should give a different contribution to the calculated Raman spectra or not, and therefore understand better the origin of each part of the Raman spectra.

3:Methods

3.1 Sample growth & annealing

The double layer Bi2212 can be grown with different methods, like self-flux or KCl flux method. However the method that gave the best sample quality and allowed to grow successfully large Bi2223 sample is the Travelling Solvent Floating Zone method. This method advantage consists in the high temperature spatial gradient that can be reached. This allows growing the crystal in a fixed point in the temperature-composition phase diagram, making it possible to grow materials with a narrow crystallization field like Bi2223.[126] An additional advantage of the TSFZ method is that it does not use a crucible, and this allows to avoid contaminations of the sample and the delicate procedure of removing the grown sample from the crucible without breaking it.

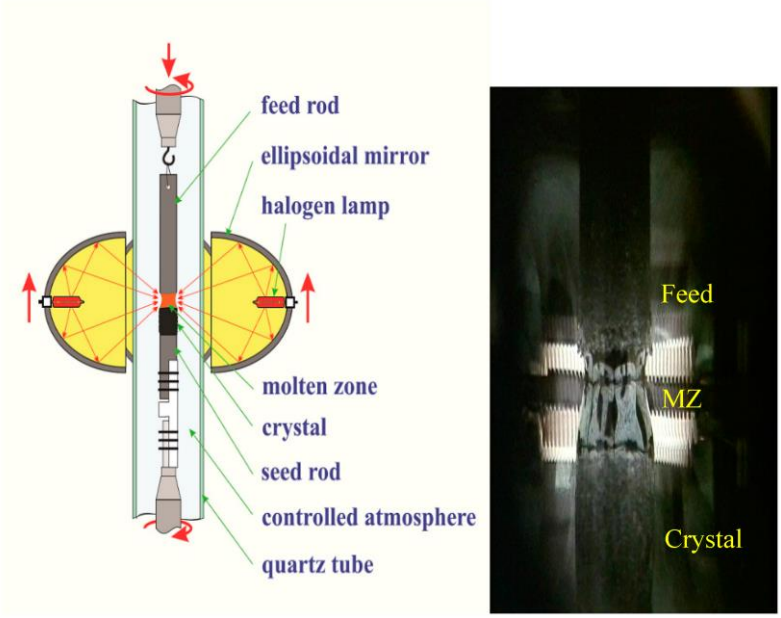

Fig.3.1 Taken from Ref.[144] On the left schematic of the TSFZ principle. On the right picture of the rods during the growth process.

In Fig.3.1 a schematic of the TSFZ set-up is shown. The method is based on the use of halogen lamps that emit IR radiation. This IR light is focused by ellipsoidal mirrors on the feed rod which melts and the crystal grows on the seed rod. The mirrors or the rod is moved slowly so that the focusing point of the mirrors, and therefore the molten zone, scans the entire length of the rod. To maintain the temperature uniform the feed and seed rods are rotated in opposite directions.

The first step in the growth process of BSCCO samples is the preparation of oxide powders of Bi_2O_3, $SrCO_3$, $CaCO_3$ and CuO of high purity (99.99%). These must be weighted and added in the right proportions to obtain Bi2212 and Bi2223 samples. The desired chemical reactions are:

$$Bi_2O_3 + 2SrCO_3 + CaCO_3 + 2CuO + O_2 \rightarrow Bi_2Sr_2CaCu_2O_{8+\delta} + O_2 \quad (3.1)$$

$$Bi_2O_3 + 2SrCO_3 + 2CaCO_3 + 3CuO + O_2 \rightarrow Bi_2Sr_2Ca_2Cu_3O_{10+\delta} + O_2 \quad (3.2)$$

for Bi2212 and Bi2223 respectively. In the above chemical relationship oxygen is not balanced, a controlled mixed gas flow (for example in Ref.[126] for Bi2223: 80% Ar, 20% O_2) is set to supply oxygen during the growth process. The BSCCO are stable in a non-stoichiometric, slightly Bi rich composition, therefore a slightly Bi rich ratio for the oxide powders is used. Usually Bi_2O_3 and $SrCO_3$ are weighted to obtain a Bi/Sr ratio of 2.1/1.9. The obtained mixture is then grinded and calcinated at high temperature (≈800°C) for 12-24 hours. After the first calcination the compound is reground and calcinated again. The obtained mixture is grinded again and then hydrostatically pressed to form a rod. This rod is then sintered at ≈850°C for 48 hours. The obtained sintered rod is polycrystalline. This polycrystalline rod is fed to the TSFZ system. First the rod is pre-melted at a higher speed of 20-70 mm/hour. After the first fast scan a much slower scan is performed at speeds ranging from 0.05 to 0.2 mm/hours, and the single crystal is grown in the seed rod. Here a controlled flow of oxygen controls the initial sample doping. The Bi2212 samples were grown in Tajima group at Osaka University while the Bi2223 samples where grown by our collaborators in Watanabe group at Hirosaki University. The readers interested in further details about the sample growth may consult Ref.[127], [145], [146] for the Bi2212 samples and Ref.[125], [126] for the Bi2223.

To change the sample doping, by tuning the oxygen content, the annealing procedure can be performed. This is done by heating the sample in a furnace, and using a controlled atmosphere, usually of oxygen in our case. The temperature, the annealing time and the content of the controlled atmosphere are the parameters that control the final sample doping. The time of cooling after the annealing is finished should be kept as short as possible in order to avoid modifying the oxygen content desired and broadening the sample superconducting transition. To avoid this, quenching can be performed, by immersion in liquid nitrogen or by contact with a copper plate. For further details about the annealing conditions we suggest Ref.[147], [148] for Bi2212 samples and Ref.[125], [131] for Bi2223.

3.2 Raman

The name Raman comes from the Indian physicist C.V. Raman (Nobel Prize 1930) who first showed the Raman effect experimentally. The Raman effect is an inelastic scattering of light, in which the incident photon excites an electron to a higher (often virtual) state, and the scattered photon is emitted by the electron decaying back to a lower state. Here the final state can be a vibrational state at a higher, lower or at the same energy as the initial one giving rise to Stokes anti-Stokes or Rayleigh lines. In the first two cases a vibrational mode is excited to a higher or lower vibrational level. Therefore Raman is a photon in photon out technique, unlike for example ARPES which is a photon in electron out technique. Due to its sensibility to phonon states Raman spectroscopy was widely used to investigate phonon vibration in all sorts of materials.

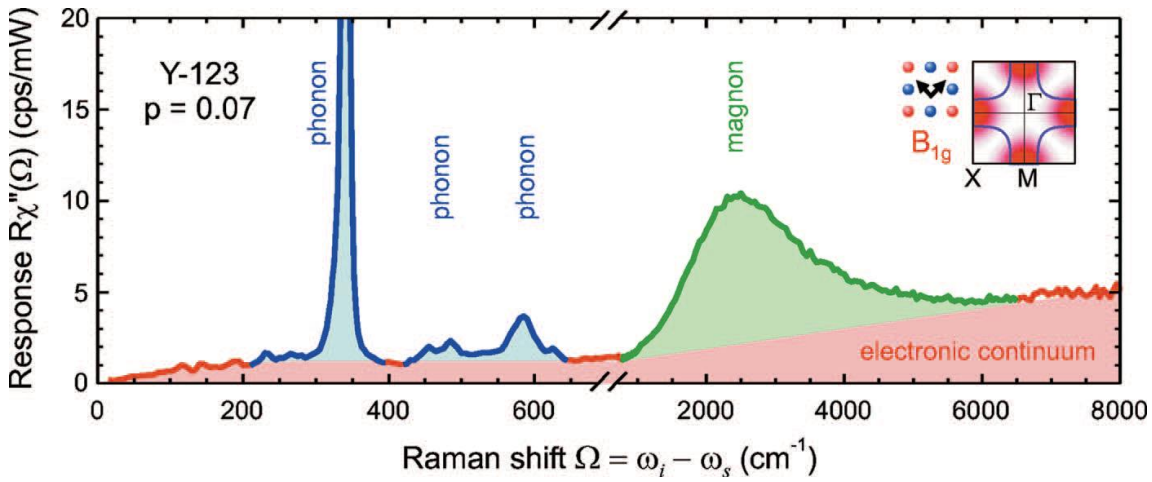

Fig.3.2 Taken from Ref.[149] Characteristic Raman scattering spectrum YBCO. Light scattering contributions from phonons, magnons, and electrons are plotted in blue, green, and red, respectively.

However the Raman effect may occur with excitation different from the phononic ones, as seen in Fig.3.2, excitation of electronic states and of magnons are also possible and these different contribution overlap in cuprates. In contrast to phonon excitations, which originate from distinct vibrational levels that give sharp peaks, the electronic contribution is broad, since a continuum of state is available for the excitation, as it can be seen in Fig.3.2.

Electronic Raman scattering ERS has multiple advantages such as being sensible to both occupied and unoccupied states, being momentum resolved and sensible to the bulk of the sample. For these reasons it is a powerful technique to study the electronic states in cuprates superconductors.

As in the case of phononic excitation, ERS involves a transition to a higher level caused by the incident light and the emission of a scattered photon when the electron decays to a lower level,

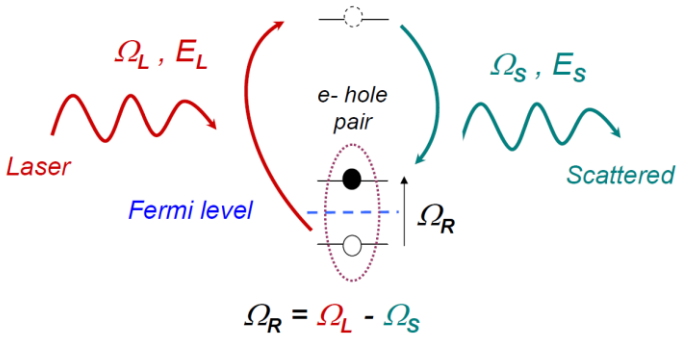

Fig.3.3 Taken from Ref.[143] Electronic Raman scattering process (Stokes process): a crystal is irradiated by a monochromatic wavelength of a laser beam and the scattered light is collected. The difference in frequency between the laser and scattered frequencies (Ω_L and Ω_S respectively) is called the Raman shift, Ω_R and corresponds to the energy of an electron-hole pair excitation around the Fermi level.

and this is shown in Fig.3.3 in the case of a Stokes process. The difference between the incident and scattered light frequencies (Ω_L and Ω_S respectively) is called the Raman shift, Ω_R. In the superconducting state the final and initial state can be states across the superconducting gap and this can cause the breaking of a Cooper pair, with the creation of Bogoliubov quasi-particles. This gives a contribution to the Raman spectra at the energy of the superconducting gap.

Being a two photon process ERS is a second order process in the electromagnetic field. This means that in the interaction Hamiltonian between electron and the radiation originates both from the second order term and from the first order term perturbation up to the second order. It was shown[150] that both these terms can be gathered in a single effective second order Hamiltonian in the form:

$$H_R = \frac{e^2}{m}\langle A_S A_L\rangle e^{-i\Omega t}\hat{\rho}_q \qquad (3.3)$$

Where A_S and A_L are the scattered and laser (incident) light vector potentials and the bracket indicates the proper matrix element over the photon states. Ω indicates the Raman shift (= Ω_L - Ω_S) and q the difference between the photon momenta is $q = k_L - k_S$. The operator $\hat{\rho}_q$ is given by:

$$\hat{\rho}_q = \sum_{n_f,n_i,k} \gamma_{n_f,n_i,k} c^{+}_{n_f,k+q}\, c_{n_i,k} \qquad (3.4)$$

Here k is the initial electronic momentum, and n_f and , n_i indicate the final and initial electronic states respectively. $\gamma_{n_f,n_i,k}$ is the Raman vertex and is given by:

$$\gamma_{n_f,n_i,k} = e_S^* \cdot e_L \delta_{n_f,n_i} + \frac{1}{\hbar m} \sum_{n_m} \frac{\langle n_f, k+q|e^{-ik_S\cdot r} e_S^* \cdot p|n_m, k+k_L\rangle\langle n_m, k+k_L|e^{-ik_L\cdot r} e_L \cdot p|n_i, k\rangle}{\varepsilon_{n_i,k} - \varepsilon_{n_m,k+k_l} + \Omega_L + i\eta} + (L \leftrightarrow S) \qquad (3.5)$$

e_L and e_S are respectively the incident and scattered field polarization and $\varepsilon_{n,k}$ are the electronic states energies.

The Raman vertex in (3.5) depends on the band structure of the material and is difficult to calculate explicitly. However some simplifications can be made. The photon momentum transfer q in the visible range is much smaller than the electronic momentum and it can therefore usually neglected. Under this approximation the Raman vertex can be decomposed using the group theory. This is extremely useful to highlight the momentum dependence of ERS and to show how this depends on the chosen incident and scattered light polarization. In the case of cuprates, since they have a slightly distorted tetragonal phase they belong to the D_{4h} space group and the Raman vertex can be decomposed on the irreducible representation of this group:

$$\tilde{\gamma}(q \to 0) = \sum_{\mu} \gamma_\mu \Phi_\mu \qquad (3.6)$$

Geometry	e_L	e_S	R	Basis Function Φ_μ (k)
xx, yy	x̂,ŷ	x̂,ŷ	$R_{A_{1g}} + R_{B_{1g}}$	$0.5[\cos(k_x a) - \cos(k_y a)] \pm 0.5[\cos(k_x a) - \cos(k_y a)]$
x'x'	(x̂+ŷ) / $\sqrt{2}$	(x̂+ŷ) / $\sqrt{2}$	$R_{A_{1g}} + R_{B_{2g}}$	$0.5[\cos(k_x a) + \cos(k_y a)] + \sin(k_x a)\sin(k_y a)$
x'y'	(x̂+ŷ) / $\sqrt{2}$	(x̂-ŷ) / $\sqrt{2}$	$R_{B_{1g}} + R_{A_{2g}}$	$0.5[\cos(k_x a) - \cos(k_y a)]\,[1 + \sin(k_x a)\sin(k_y a)]$
xy	x̂	ŷ	$R_{B_{2g}} + R_{A_{2g}}$	$\sin(k_x a)\sin(k_y a)\{1 + 0.5[\cos(k_x a) - \cos(k_y a)]\}$
LR	(x̂+iŷ) / $\sqrt{2}$	(x̂+iŷ) / $\sqrt{2}$	$R_{B_{1g}} + R_{B_{2g}}$	$0.5[\cos(k_x a) + \cos(k_y a)] + \sin(k_x a)\sin(k_y a)$
LL	(x̂+iŷ) / $\sqrt{2}$	(x̂-iŷ) / $\sqrt{2}$	$R_{A_{1g}} + R_{A_{2g}}$	$0.5\{\cos(k_x a) + \cos(k_y a) + [\cos(k_x a) - \cos(k_y a)]\sin(k_x a)\sin(k_y a)\}$
xz	x̂	ẑ	$R_{E_{1g}}$	$\sin(k_x a)\sin(k_z c)$
yz	ŷ	ẑ	$R_{E_{1g}}$	$\sin(k_y a)\sin(k_z c)$
zz	ẑ	ẑ	$R_{A_{1g}^{(2)}}$	$\cos(k_z c)$

Table 3.1 Taken from Ref.[149] Elements of the transition rate R for experimentally useful configurations of polarization orientations e_L and e_S (given in Porto notation) along with the symmetry projections for the D_{4h} point group relevant for the cuprates. Here we use notations in which x and y point in directions along the Cu-O bonds in tetragonal cuprates, while x' and y' are directions rotated by 45°. L and R denote left and right circularly polarized light, respectively.

Where μ represents the irreducible representation of the point group of the crystal and Φ_μ are the basis functions of said irreducible point group of the crystal. This means that the contraction of the Raman vertex tensor $e_S^* \cdot \tilde{\gamma} \cdot e_L$ will depend only on the terms in the summation in (3.6) that are selected by the scattered and incident light polarization vector. Table 3.1 summarizes the most commonly used incident and scattered light configurations in cuprates. Here the x and y are along the Cu-O bonds, while x' and y' are directions rotated by 45°. Additionally here the basis function Φ_μ relative to each scattering configuration is shown. The configurations mainly used in this study are $\bar{z}(x'y')z$ and $\bar{z}$ (xy)z in the Porto notation. In this notation A(BC)D, A and D indicate the direction of the incident and scattered light wavevector respectively and B and C indicate the incident and scattered light polarization direction. These two configurations mainly probe the B_{1g} and B_{2g} modes respectively, with a small A_{2g} contamination, and are for simplicity referred as B_{1g} and B_{2g} configurations in Raman studies. As it can be seen from Table 3.1 and Fig.3.4 these two configurations probe mainly the antinodal and nodal region respectively.

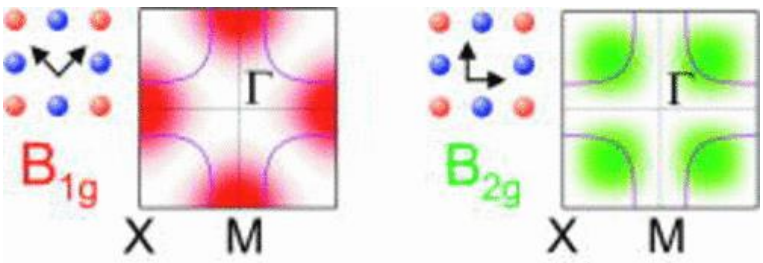

Fig.3.4 Taken from Ref.[149] Schematic weighting of the light-scattering transition for polarization orientations probing B_{1g} and B_{2g} for a D_{4h} crystal. High-symmetry points are indicated. Here a

typical Fermi surface for optimally doped cuprates is represented by the solid line, and the orientations of the incident and scattered polarization light vectors are shown with respect to copper-oxygen bond directions.

Raman probes directly the Fourier transform of the density-density correlation function called the "dynamical structure factor" which is given by: [151]

$$S(q,\Omega,T) = \int \frac{dt}{2\pi} e^{i\Omega t} \langle \hat{\rho}^{\dagger}(q,t)\hat{\rho}(q,0)\rangle_T \qquad (3.7)$$

where the bracket denotes the thermal average. According to the fluctuation dissipation theorem,[152] $S(q,\Omega,T)$ is related to the imaginary part $\chi''(q,\Omega,T)$ of the response function $\chi(q,\Omega,T)$ as follows

$$S(q,\Omega,T) = \frac{\hbar}{\pi}(1+n(\Omega,T))\chi''(q,\Omega,T) \qquad (3.8)$$

Here $n(\Omega,T)$ is the Bose Einstein factor given by $n(\Omega,T) = \left(e^{-\frac{\hbar\Omega}{k_B t}} - 1\right)^{-1}$. The imaginary part of the response function is related to the electronic density fluctuations induced by the electric field of the incident light into the crystal, and is therefore the wanted signal. For this reason the experimental spectra is usually divided by $(1+n(\Omega,T))$.

In Fig.3.5 a schematic of a typical experimental electronic Raman scattering set-up is shown. The incident Radiation is produced by a laser, in our case an Ar^{+}-Kr^{+} gas laser is used. This laser can emit light at different frequency, and for the present work the emission line that produces green radiation with a wavelength of λ = 514.5 nm was selected. Different choices of incident light energy influence the intensity of the phonons in the spectra, and in general light energies that strongly enhance the phonon peaks should be avoided when interested in the electronic contribution. The emitted light is reflected and passes through different optical components on its way to the sample space. These include pinholes to decrease the radial dimension of the laser beam and polarizers to select the incident radiation polarization direction. The sample space is equipped, in our case, with an oil pump and a turbomolecular pump that allows to obtain a vacuum in the sample space, with pressures as low as $P = 5 * 10^{-6}\ torr$. The vacuum is not needed for Raman spectroscopy, since the emitted photons can travel through air, unlike for example ARPES where the emitted electrons need vacuum to propagate. The vacuum is needed for cooling the sample at low temperature, as low as 5K, to avoid the deposition of all sort of particle and the formation of ice. The lower the sample space pressure, the longer the sample surface will maintain clean even at low temperature, allowing the experiment to last longer without the need to cleave the sample. Cooling of the sample is done with a cryostat connected to a helium compressor. The PID controller of the cryostat stabilizes the sample temperature to the desired value. Even though we ideally desire to measure in the back-scattered configuration, this should be avoided, since the reflected laser light would enter the spectrometer directly and this

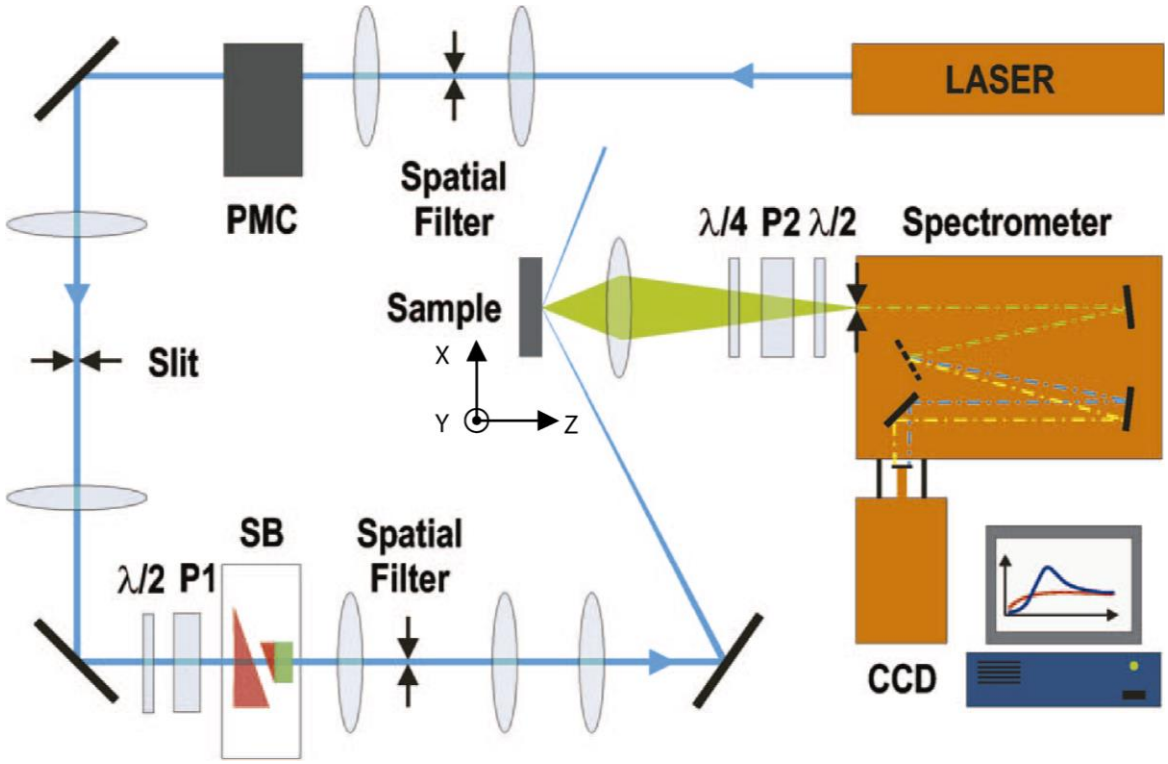

Fig.3.5 Taken from Ref.[149] Schematic of the light path in a typical ERS spectrometer.

could cause damage to the detector. Instead quasi-back scattered geometry is used with the incident radiation at about 30-45° with the *c*-axis of the sample. The sample is mounted with the *c*-axis along the Z direction in Fig.3.5, and the a and b axis (which correspond to x' and y' in Table 3.1) are oriented along the X or Y direction when measuring the B_{1g} configuration and at 45° degrees with the X and Y axis when measuring the B_{2g} configuration. The first polarizer sets the incident light polarization to be along the Y direction and therefore the second polarized must be set to collect the scattered light with a polarization along the X direction in order to measure the B_{1g} and B_{2g} configurations. However the sensitivity of the grating is highest in the Y direction, therefore a λ/2 wave plate is used to rotate the collected scattered light polarization from the X direction to the Y direction. As mentioned before ERS is a bulk technique. The penetration length in cuprates is of the order of 100 nm, spanning therefore numerous unit cells of the sample, unlike other techniques such as ARPES where the electron penetration length can span only few atomic layers. The laser spot size on the sample has a diameter of approximately 50-100 μm. To avoid local heating of the sample the power of the incident laser was kept as low as P=3mW. Local heating of the sample can, not only foul the measurement by changing the local temperature, but it can also damage the sample surface, and therefore it must be avoided.

The spectrometer used for the present study is a Jobin-Yvon T64000 located at the Graduate school of Science at Osaka University. This spectrometer is equipped with a triple monochromator system with a grating density of 1800 gr/mm. The first two grating of the system can be coupled in two different ways in the additive or subtractive mode shown in Fig.3.6. In the additive mode all of the gratings separate the different wavelengths, and this allows reaching extremely high energy resolution, as good as 0.1 cm^{-1}, however this will allow measuring only a small spectral window. In

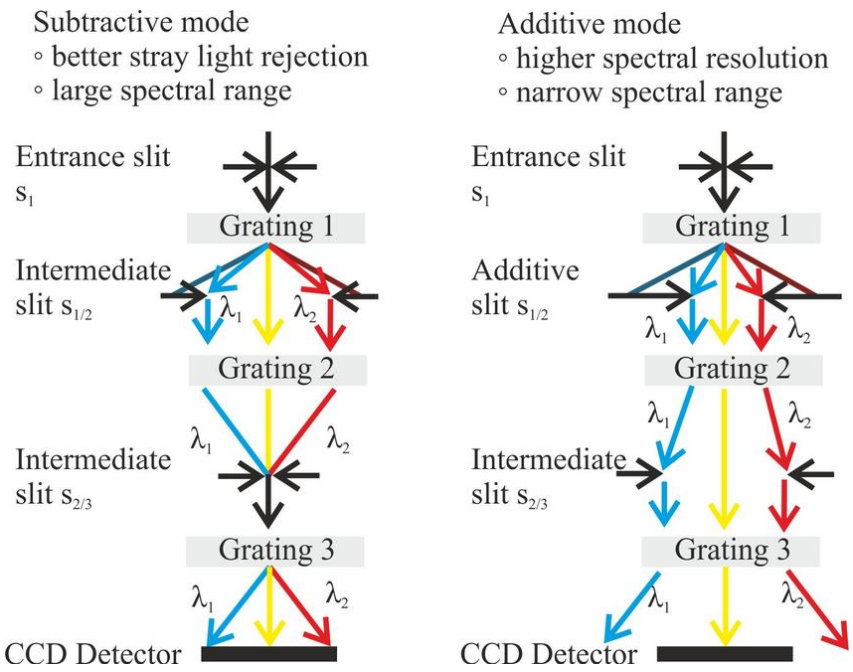

Fig.3.6 Taken from Ref.[153] Schematic sketch of the additive and subtractive mode for triple monochromators

the subtractive mode the first grating splits the different wavelengths, which are filtered in the first intermediate slit, and then the second grating recomposes the different frequencies. This allows having a very efficient rejection of the frequency outside the window selected by the first intermediate slit and therefore a very good rejection of the Rayleigh scattering is obtained. The resolution of the subtractive mode can be as good as 0.3 cm^{-1}. In this study, since a good rejection of the elastically scattered light is needed, but high resolution is not, the subtractive mode is used. The electronic features are extremely broad as seen in Fig.3.2, therefore the highest resolution of the subtractive mode is also not needed. Opening the entrance slit and the second intermediate slit can increase the signal at the cost of losing resolution. In our study these slits were set to 500 µm which is a good trade off between signal intensity and resolution, giving a resolution of approximately 5 cm^{-1}. This may seem large, but it is not as compared to the scale of the electronic features.

After passing through the monochromator the light enters the detector, a Charge Coupled Device CCD, which is cooled by liquid nitrogen. The CCD can be damaged if exposed to the strong Rayleigh scattering radiation and therefore rejection of this strong contribution is extremely important. This is achieved, as said before, by the subtractive mode of the triple monochromator, but, additionally, a good sample surface is also needed. If the sample surface is degraded strong scattering originates from the surface defects preventing the measurement. In those cases it is necessary to cleave the sample and obtain a good surface with few defects.

3.3 Kubo calculations

To calculate the Raman spectra an equation much simpler than the one presented in the previous section can be used, and this is the Kubo formula given by: [149]

$$\chi''_{\gamma\Gamma} = \frac{2}{\pi V}\sum_{\boldsymbol{k}} \gamma_{\boldsymbol{k}}\Gamma_{\boldsymbol{k}} \cdot \int_{-\infty}^{\infty} (f_\omega - f_{\omega+\Omega})\, G''_{\boldsymbol{k},\omega} G''_{\boldsymbol{k},\omega+\Omega} \left(1 - \frac{\Delta_{\boldsymbol{k}}^2}{(\omega+\xi_{\boldsymbol{k}})(\omega+\Omega+\xi_{\boldsymbol{k}})}\right) \qquad (3.9)$$

that gives the Raman susceptibility $\chi''_{\gamma\Gamma}$. In this equation f_ω is the Fermi Dirac function, $G''_{\boldsymbol{k},\omega}$ is the Green function, $\Delta_{\boldsymbol{k}}$ is the superconducting gap, $\xi_{\boldsymbol{k}}$ is the bare band in the normal state and $\gamma_{\boldsymbol{k}}$ and $\Gamma_{\boldsymbol{k}}$ are the bare and renormalized Raman vertices. The goal of the calculation performed in this work is to obtain more realistic calculated spectra by using the experimental ARPES intensity as an input. Therefore, we want to obtain the Green function from the ARPES intensity. This can be done using the formulas:

$$I_{\boldsymbol{k},\omega} = I_0 \cdot M_{\boldsymbol{k}} \cdot f_\omega \cdot A_{\boldsymbol{k},\omega} \qquad (3.10)$$

$$G''_{\boldsymbol{k},\omega} = -\pi A_{\boldsymbol{k},\omega} \qquad (3.11)$$

The equation (3.10) gives the ARPES intensity where $A_{\boldsymbol{k},\omega}$ is the spectral function and $M_{\boldsymbol{k}}$ is the matrix element. The equation (3.11) gives the relationship between the Green function and the spectral function. Here to directly obtain the Green function from the ARPES intensity we make the approximation that the matrix element does not depend on the momentum ***k***. Calculation of the ARPES matrix element is complicated, however it was shown that it has often a weak momentum dependence, and therefore the approximation can be justified

As it will be discussed more in detail in the next section the ARPES spectra have a background that originates from the inelastically scattered electrons during their propagation through the sample, and this contribution must be subtracted. One way to do so is to use the empirical Shirley background which is given by:

$$bg_{Shirley}(\omega) = c\int_{\omega}^{\infty} P(\omega')\, d\omega' \qquad (3.12)$$

Here $P(\omega')$ is the spectrum after the background subtraction. The calculation of the Shirley background is done in an iterative way assuming that the signal at $\omega = \infty$ is completely background and using an initially small c, this Shirley constant is gradually increased until the spectrum at the highest binding energy is all composed by background, and this iterative procedure is shown in Fig.3.7

In the case of band splitting, to calculate separately the contribution of each band to the Raman spectra the ARPES intensity of these bands must be separated. This can be done by fitting the Energy Distribution Curves (EDC) with multiple Gaussian functions. This is done using 3 Gaussian peaks: one for each band and an additional one for the incoherent part at higher binding energy.

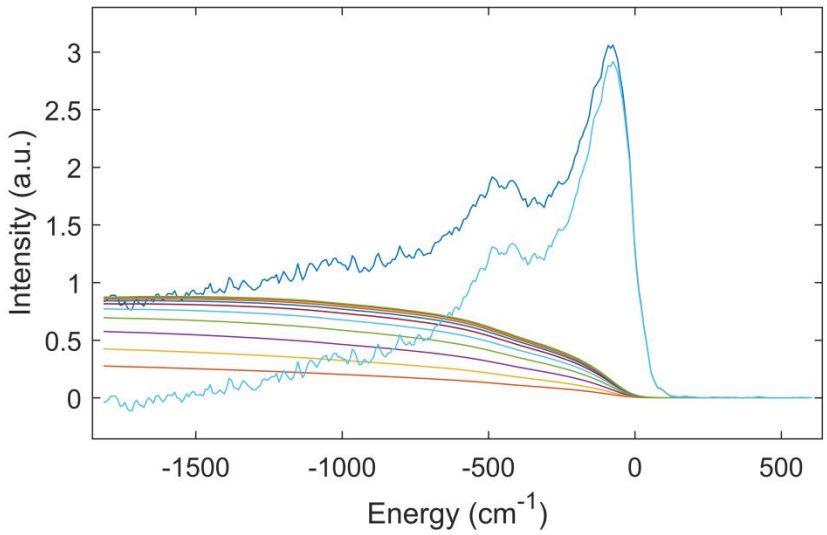

Fig.3.7 Example of iterative Shirley background subtraction on an EDC in optimally doped Bi2223

The bare-band can be obtained from tight binding fitting using the equation:

$$\xi_{\boldsymbol{k}} = -2t\left(\cos k_x a + \cos k_y a\right) + 4t' \cos k_x a \cos k_y a - 2t''\left(\cos 2k_x a + \cos 2k_y a\right) - \mu \quad (3.13)$$

Here t, t' and t'' are the nearest, the next nearest and the next-next nearest hopping integral and μ is the chemical potential. Here we are interested in the normal state band dispersion, but to perform the fit it is still possible to extract the fitting points from the superconducting low temperature data. This is done by using as fitting points the Fermi vector k_F at zero energy. The k_F position does not change in the case of a superconducting gap opening, which is particle-hole symmetric. An additional fitting point used in the fit is the experimental band bottom at Γ. For simplicity and in order not to add too many free parameters t'' is fixed to be half of t'. Therefore the fitting free parameters are t, t' and μ. In the case of multilayer band splitting multiple bands must be fitted. In the case of Bi2223 the OP and IP bands have been fitted separately but in the case of Bi2212 a multilalyer splitting term was added to (3.13) to fit simultaneously the anti-bonding band AB and the bonding band BB:

$$E_{bi} = -\frac{t_\perp}{4}\left(\cos k_x a - \cos k_y a\right)^2 \quad (3.14)$$

This is the simplest form of bilayer splitting term, and is not ideal for realistic calculations,[21] however it can be used in this case, since we are simply interested in a small momentum region where the superconducting gap opens. This tight binding fitting is not only used in (3.9) but is also used to calculate the gap size $\Delta_{\boldsymbol{k}}$ in the ARPES cut between k_F and the momentum where the gap starts opening.

As shown in the previous section, explicit calculations of the Raman vertex is not trivial, and the calculation of the renormalized Raman vertex is not trivial either, with several possible correlation terms contributing. For simplicity, in the present work we use the Raman vertices calculated from

the assumption of single band given by the tight binding formula in a tetragonal lattice. These are used both for the bare and renormalized Raman vertex and are given by:

$$\gamma_{B_{1g},\boldsymbol{k}} = \boldsymbol{\Gamma}_{B_{1g},\boldsymbol{k}} = ma^2t(\cos k_x a - \cos k_y a) \qquad (3.15)$$

$$\gamma_{B_{2g},\boldsymbol{k}} = \boldsymbol{\Gamma}_{B_{2g},\boldsymbol{k}} = 4ma^2t' \sin k_x a \sin k_y a \qquad (3.16)$$

for B_{1g} and B_{2g}, respectively. The assumption of identical bare and renormalized Raman vertex is likely a poor approximation for strongly correlated cuprates, but we expect it to be sufficient for the present study.

3.4 ARPES

Angle Resolved Photoemission Spectroscopy (ARPES) is the best technique to experimentally observe the band dispersion, since it can directly image the occupied electron band with momentum and energy resolution. ARPES is a photon-in and electron-out technique and since the electron must diffuse out of the sample in order to be detected, the probed area is limited by the electrons mean free path to a few atomic layers making ARPES surface sensitive. ARPES, unlike Raman, can only probe occupied electronic states. Regardless these two limitations, the direct momentum and energy resolved image of the electron bands makes it an extremely valuable technique.

The ARPES process can be described in the framework of the three step model where the steps are:

1. An incident photon is absorbed by an electron in the sample which is excited to the final free electronic state.
2. The excited electron travels without losing energy nor changing momentum to the surface of the sample.
3. The electron escapes from the sample by overcoming the work function ϕ and enters the vacuum states.

However, this is an approximation since the excited electrons do interact sometimes with the lattice and other electrons, losing energy. Nonetheless, a good amount of electrons will not interact with anything as postulated by the three steps process and in that case conservation of energy applies and is given by:

$$E_{kin} = h\nu - \phi - |E_B| \qquad (3.17)$$

where $h\nu$ is the incident photon energy and E_B is the emitted electron former binding energy, and this is shown in the schematic in Fig.3.8 (b). From this conservation of energy comes the energy resolution of ARPES, while the momentum resolution comes from the momentum conservation.

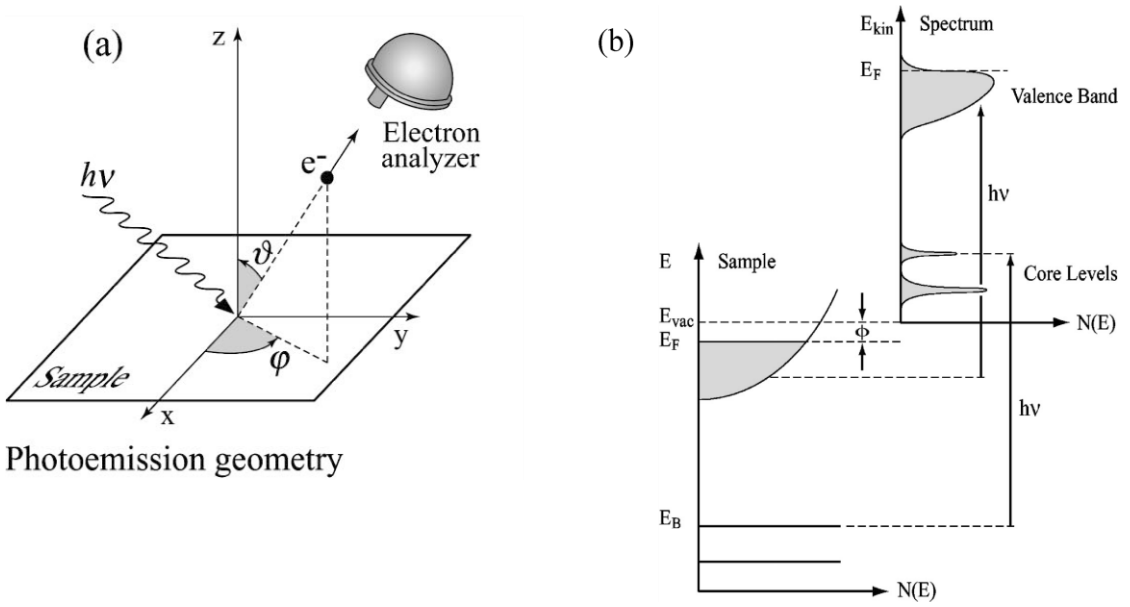

Fig.3.8 Taken from Ref.[33] **a** diagram of the ARPES process. **b** Schematic the conservation of energy in the ARPES process. **c**

Normally the electron momentum is much larger than the photon momentum which can be therefore neglected. The momentum along the sample plane is conserved according to:

$$k_{\parallel} = \frac{\sqrt{2mE_{kin}}\sin(\vartheta)}{\hbar} \qquad (3.18)$$

Where ϑ is the angle between the vector normal to the sample surface and the electron trajectory. However the momentum normal to the sample surface is modified by the sample surface potential step, called inner potential V_0. Therefore the momentum of the electron in the direction normal to the plane surface is given by:

$$k_{\perp} = \frac{\sqrt{2mE_{kin}cos^2(\vartheta) + V_0}}{\hbar} \qquad (3.19)$$

Using the hemispherical analyser in the configuration in Fig.3.8 (a), E_{kin}, can me measured and the electron emission angles are known. Therefore considering the equation from (3.17) to (3.19) we can obtain the original binding energy and the momentum of the electron in the sample, and this makes ARPES a extremely viable momentum and energy resolved technique.

In the sudden approximation, where the emitted electron does not interact with the sample, the ARPES intensity can be written as:

$$I_{\boldsymbol{k},\omega} = I_0(\boldsymbol{k}, \nu, \boldsymbol{A}) \cdot A_{\boldsymbol{k},\omega} \cdot f_{\omega} \qquad (3.20)$$

where $\boldsymbol{A}$ is the vector potential, $A_{\boldsymbol{k},\omega}$ is the spectral function and f_{ω} is the Fermi-Dirac distribution. This shows how ARPES is sensible only to occupied states. Here the intensity $I_0(\boldsymbol{k}, \nu, \boldsymbol{A})$ is proportional to:

$$I_0(\boldsymbol{k}, \nu, \boldsymbol{A}) \propto \left|M_{\mathrm{f,i}}^{\boldsymbol{k}}\right|^2 \propto \left|\left\langle \phi_f^{\boldsymbol{k}} \middle| e \cdot r \middle| \phi_i^{\boldsymbol{k}} \right\rangle\right|^2 \qquad (3.21)$$

where $\left|M_{\mathrm{f,i}}^{\boldsymbol{k}}\right|^2$ is the squared module of the matrix element, $\phi_f^{\boldsymbol{k}}$ and $\phi_i^{\boldsymbol{k}}$ are the the initial and final electronic state and e is the unit vector of the incident light polarization. Here it can be seen, by discussion of parity of these functions, how ARPES sensibility is influenced by the parity of the initial state $\phi_i^{\boldsymbol{k}}$ orbitals

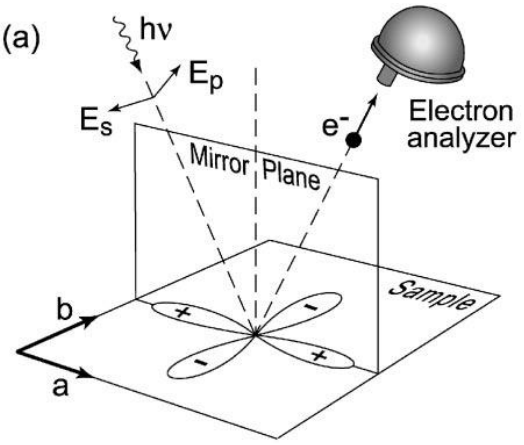

Fig.3.9 Taken from Ref.[33] the mirror plane in the ARPES experiment. The parity with respect of this plane can be considered to make prediction on the matrix element intensity.

and this is the orbital selectivity of ARPES. The parity with respect to the mirror plane, which is defined by the incident light and the scattered electron trajectories as seen in Fig.3.9, can be considered to evaluate quickly the intensity of the matrix element. Here the final state $\phi_f^{\boldsymbol{k}}$ can be approximated with the wavefunction of a free electron in vacuum $e^{i\boldsymbol{k}\cdot\boldsymbol{r}}$ and will always be even with respect to the mirror plane since $\boldsymbol{k}$ is in plane. The parity of $\phi_i^{\boldsymbol{k}}$ depends on the orbital character of the band the electron is in, and the parity of $e \cdot r$ can be selected by choosing the incident photon polarization, where with in-plane polarization the term will be even and with out of plane polarization it will be odd. Therefore by observing the dependence of the ARPES intensity on the polarization of the incident light one can guess the parity of the initial state of the electron, and make guesses on the main character of the electron band.

In order to obtain the precise energy value of the Fermi level E_F the sample is usually connected electronically to a metal, often gold, and the ARPES spectrum of this metal is measured. The spectrum of this reference metal is dictated by the Fermi Dirac function near the Fermi level, whose value can be therefore extracted.

There are various possible source of the exiting radiation. In the field of cuprates, recently the most popular choices are synchrotron radiation and laser radiation. The latter has the advantage that high momentum resolution can be obtained. Since the electrons cannot propagate in air, the whole electron path from the sample to the detector must be in vacuum. Usually the sample can be cleaved in vacuum in order to obtain the best possible sample surface, free from contaminations. The emitted electrons pass through electrostatic lenses and are collected by a hemispherical analyser usually equipped with a CCD detector. The hemispherical analyser can

collect electron with different momentum direction, which are allowed through a slit elongated along one direction, the analyser separates the electrons according to their energy in the perpendicular direction. Therefore the CCD collects a 2D image in which one direction is proportional to the energy and the other to the angle of emission, which is related to the momentum. Therefore the ARPES data are usually 3D, the dimension being momentum, energy and intensity, and represent cuts along a certain curve in the momentum space of the 5D space

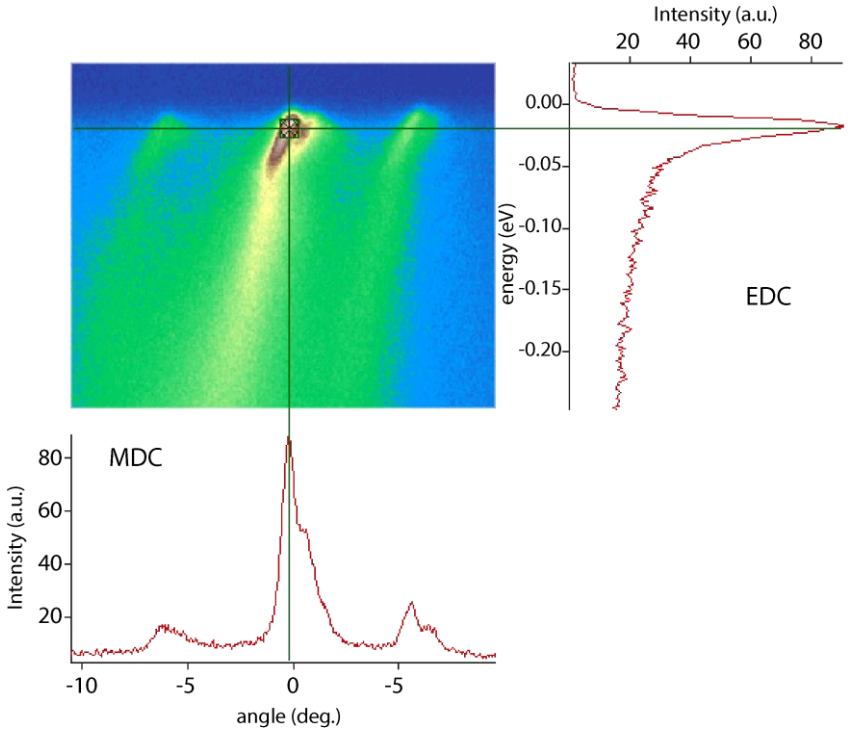

Fig.3.10 Example of ARPES cut for the Bi2212 overdoped sample OD85K. An ARPES cut can be viewed as a 2D image where the colour scale is associated with intensity and one axis (vertical here) is associated with binding energy and the other with momentum (angle of emission of the electron). These images can be furtherly cut at a certain momentum, obtaining the EDC on the left, or at a certain energy, obtaining the MDC in the bottom of the figure.

constituted by momentum, energy and spectral function. These cuts can be viewed by 2D images where the colour is associated to the intensity, or can be furtherly cut restricting to a specified energy or momentum and viewed as spectra, and these are called Momentum Distribution Curves MDC and Energy Distribution Curves EDC respectively. The EDC are generally used to extract the energy value of a certain band or the value of an energy gap and the MDC are generally used to establish the momentum position of a certain band or spectral feature.

The ARPES Bi2212 data for the samples UD75K and OP92K, used as an input in the Kubo calculations in this study, have been carried out at Stanford Synchrotron Radiation Lightsource beamline 5-4 using 22.7 eV photons with an energy resolution of 5 meV and an angular resolution of 0.1° degrees, with polarization along the Cu-O directions (out of the mirror plane). The ARPES Bi2212 data for the sample OD85K were measured at Institute for Solid State Physics at Tokyo University, using a He lamp with a photon energy of 21.2 eV without polarization. For these the

energy resolution was 10 meV and the angular resolution was 0.1° degrees. These experiments have been carried out by a colleague of my same laboratory. (Tajima Lab. Osaka University)

Bi2223 ARPES data where obtained on a slightly underdoped (but almost optimal doped) sample (T_C=108K) grown by Uchida group in Tokyo University. The experiment was performed at UVSOR facility beamline number 7 in the National Institute for Molecular Science in Japan. Radiation with energy of *hv*=8eV was used. The data were taken at a sample temperature of T=12K. The polarization of the incident radiation was outside of the mirror plane (S polarization) and the energy resolution was ΔE=7meV. These experiment have been carried out by S.Ideta (National Institute for Molecular Science)

3.5 Others: SQUID & XRD

To evaluate the sample critical temperature the susceptibility of the sample can be measured. This was done using a Quantum Design Magnetic Property Measurement System (MPMS) located at Tajima group at Osaka University. This is a SQUID (Superconducting QUantum Interference Device) magnetometer. The SQUID magnetomer employs a superconducting ring with two Josephson junctions and detects the variations in magnetic flux through this ring. This can be used to measure the magnetic susceptibility of the sample, and the onset of the diamagnetic signal due to the Meissner effect marks the onset of superconductivity. A magnetic field of 10 Oe was applied along the *c*-axis of the sample and the temperature dependence of the susceptibility was measured. Here both Field Cooling FC and Zero Field Cooling ZFC susceptibility was measured, where in ZFC the sample is cooled and then the magnetic field is applied, and in FC the opposite order is used, by cooling with an already applied magnetic field. Here the T_C of the sample was defined by the onset temperature of the Meissner effect, additionally the sharpness of the superconducting transition was defined as the difference between the onset temperature and the temperature where the 90% value of the low temperature FC susceptibility was reached. Good samples where the oxygen content is homogeneous are expected to have sharp superconducting transitions.

X-ray diffraction is a powerful technique for determining the structure of a crystal. By illuminating the sample with a monochromatic beam of X-rays, the photons will be scattered by the atoms of the sample and will produce a diffraction pattern. This diffraction pattern is named Laue image and since it originates from the spatial Fourier transform of the scattering centers is a way to image the reciprocal lattice of the crystal. In this study a four-axis X-ray diffractometer located in Osaka University was used. The Laue image can be used to locate the orientation of the crystal axis. The BSCCO sample break more easily along crystallographic axis, therefore the sample borders are usually crystallographic axis, however these can be both the *a* and *b* axis or the axis rotated 45° (along the Cu-O bonds). Measuring the Laue image gives a more precise esteem of the axis orientation and solves this uncertainty. Additionally the X-ray diffraction pattern can be used to determine the crystal parameters. Since a decrease in oxygen content increases the *c*-axis, the *c*-

axis length is a measure of the sample doping.[131] Therefore in this study X-ray diffraction was used to obtain the *c*-axis length of the Bi2223 samples, using the formula of the d-spacing formula for a tetragonal crystal given by:

$$\frac{1}{d^2} = \frac{h^2 + k^2}{a^2} + \frac{l^2}{c^2} \qquad (3.22)$$

Where *h k* and *l* are the Miller indices, *a* and *c* are the *a* and *c*-axis length respectively. Using the (00*l*) peaks, knowing the *l* indices and given the Bragg law that connects the scattering angle to the d spacing, the value of the *c*-axis can be determined. This was done, in this work, for the Bi2223 samples, in order to estimate the average sample doping of the overdoped Bi2223 sample. Since, as discussed before, the T_C of Bi2223 does not decrease in the overdoped side, and therefore the relationship between the hole doping and T_C, valid for most cuprates, cannot be used in this case.

4:Experimental Results and Discussion

4.1 Sample Preparation

The Bi2223 sample received from our collaborators in Hirosaki University were multiple samples of two different doping levels: optimally doped and underdoped samples with T_C of ≈109K and ≈88K, respectively. However, to study the doping dependence of the Raman spectra, having more than two sample doping is preferred. Therefore, we performed annealing to obtain samples with different doping levels. The annealing conditions for the samples we received from our collaborators were: 40 hours under O_2 flow at 600 ˚C[131] for the optimally doped sample and 1-3 hours under P_{O2}≈2Pa at 600°C[125] for the underdoped sample.

Since the underdoped sample was quite strongly underdoped, our first goal was to produce a slightly underdoped crystal with a doping intermediate to the doping levels of the samples received. Since there was no previous laboratory expertise in doping Bi2223 sample, few steps with trial and error where involved. Annealing in a mixed argon and oxygen flow is a possible way to change the oxygen content of the samples. However, annealing in air can also be used.[154] Therefore, for simplicity, starting from one of the underdoped samples received from the sample grower, we firstly annealed in air, at 400°C for 40 hours. The T_C increased to 97 K, however the superconducting transition was found to be broad (37K). As discussed in the previous section, the T_C was obtained from the onset of the Meissner effect, while the broadness was obtained by the

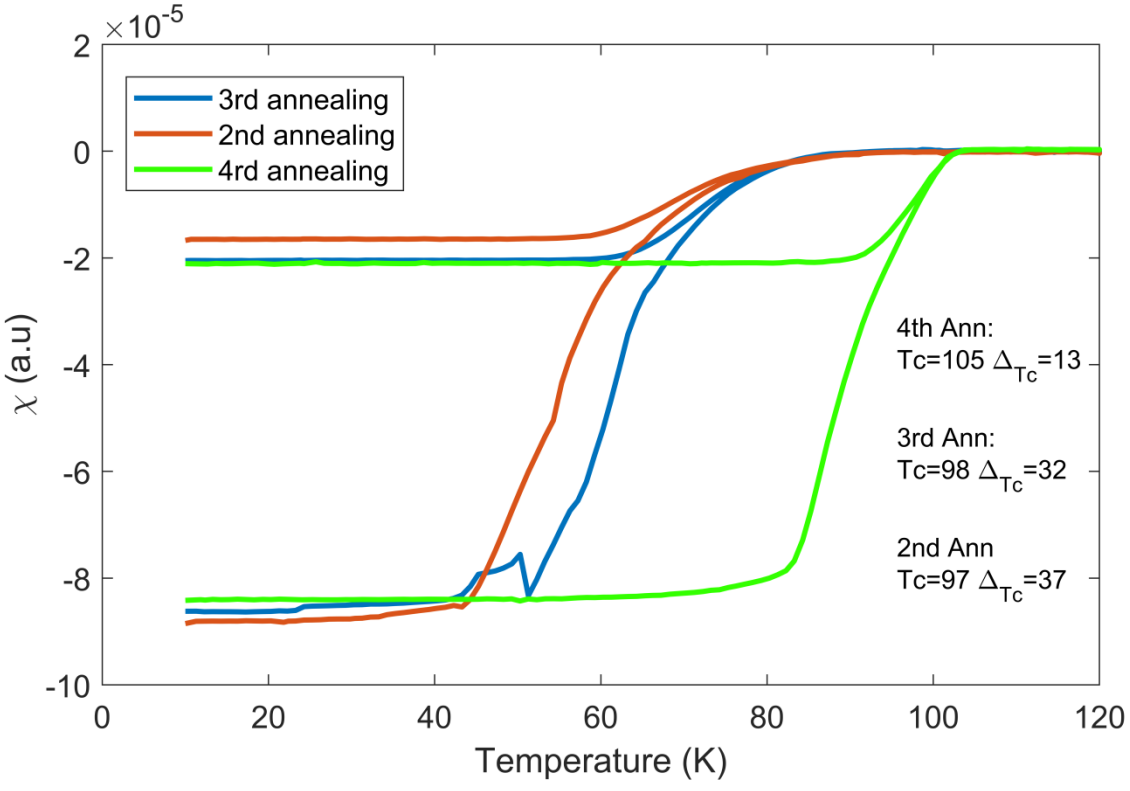

Fig.4.1 Magnetic susceptibility of the slightly underdoped sample after each of the annealing steps.

difference between T_C and the temperature where the 90% value of the low temperature susceptibility was reached.

To try improving the sharpness and slightly increase T_C we annealed again in air, for longer time, 3 days, at a lower temperature, 370°C. However the T_C increased by just one degree and the sharpness got just slightly better. We therefore decided to anneal in oxygen atmosphere, at 700°C, for 5 days, and quenched by immersing the sample in liquid nitrogen at the end of the process. After this anneal we obtained a T_C of 105K and a quite sharp transition (13K). A slightly underdoped sample was therefore obtained, whose susceptibility can be seen in Fig.4.1.

To investigate also the overdoped side of Bi2223, we attempted to obtain an overdoped sample. Firstly an optimally doped sample was obtained from the underdoped sample received from the sample grower, by annealing in O_2 atmosphere at 500 ˚C for 40 hours. Then the annealing was done in two other steps, always in O_2 atmosphere, but at lower temperature to increase the oxygen content: firstly at 450°C for 3 days and lastly at 400°C for 5 days. In this case, since the annealing temperature was lower to begin with, and the needed time to modify the oxygen content is long at lower temperature, the quenching process is not strictly needed, and was therefore skipped. In Fig.4.2 the magnetic susceptibility after these 2 annealing steps is shown together with the one of an optimally doped sample obtained from the sample grower. As it can be seen the T_C of the 3 is almost identical, and this is expected, since as said before, the T_C of Bi2223 does not decrease in the overdoped side.[131] The superconducting transition (values in Fig.4.2) is sharp in both cases, indicating that the sample quality is preserved and that the oxygen

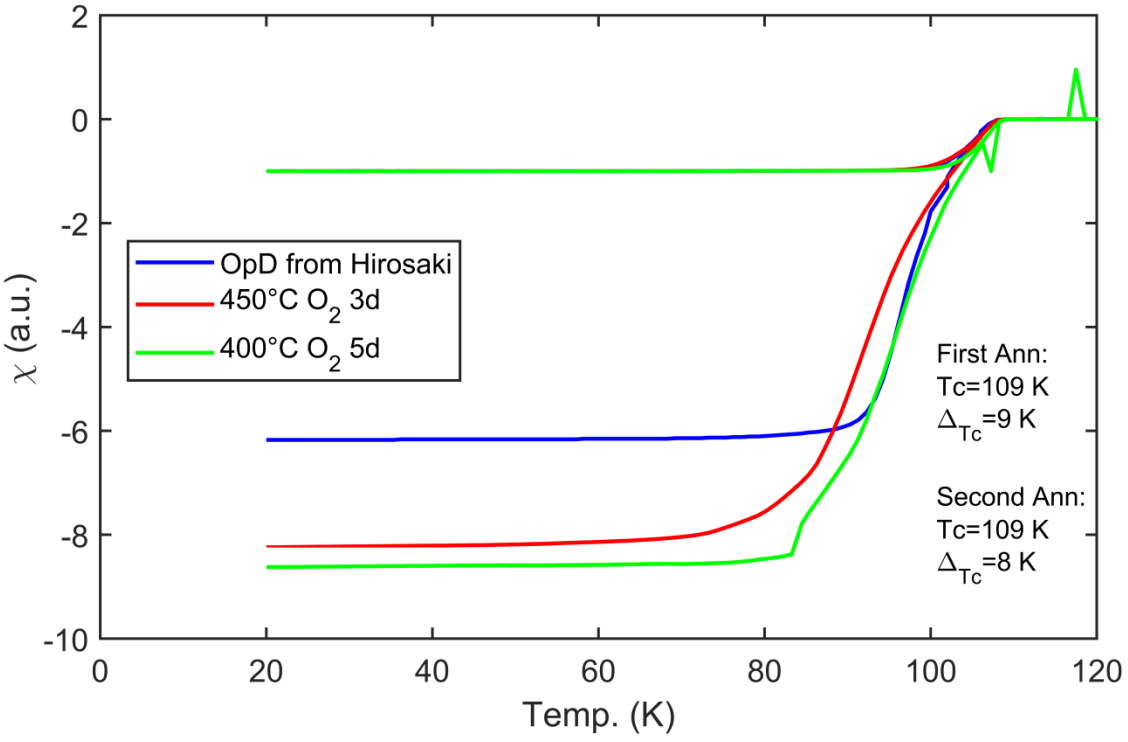

Fig.4.2 Magnetic susceptibility of the overdoped sample after each annealing step, compared with the one of an optimally doped sample received from the sample grower in Hirosaki University.

content is homogeneous enough. However, since the T_C does not change from the optimally doped sample, to make sure that the doping level is changed, a separate measurement with a different technique is needed, and this will be confirmed later with the XRD and Raman results.

With this, Bi2223 samples with four different doping levels were obtained, ranging from the overdoped to the underdoped side. The magnetic susceptibility of all the samples is shown in Fig.4.3, and the T_C and the final annealing condition are summarized in Table 4.1. The T_C was determined from the onset temperature of the Meissner signal as 109K for the slightly overdoped and optimally doped samples, 105K for the slightly underdoped sample and 88K for the strongly underdoped sample.

These samples will be referred as OvD109, OpD109, UnD105 and UnD88, respectively, from now

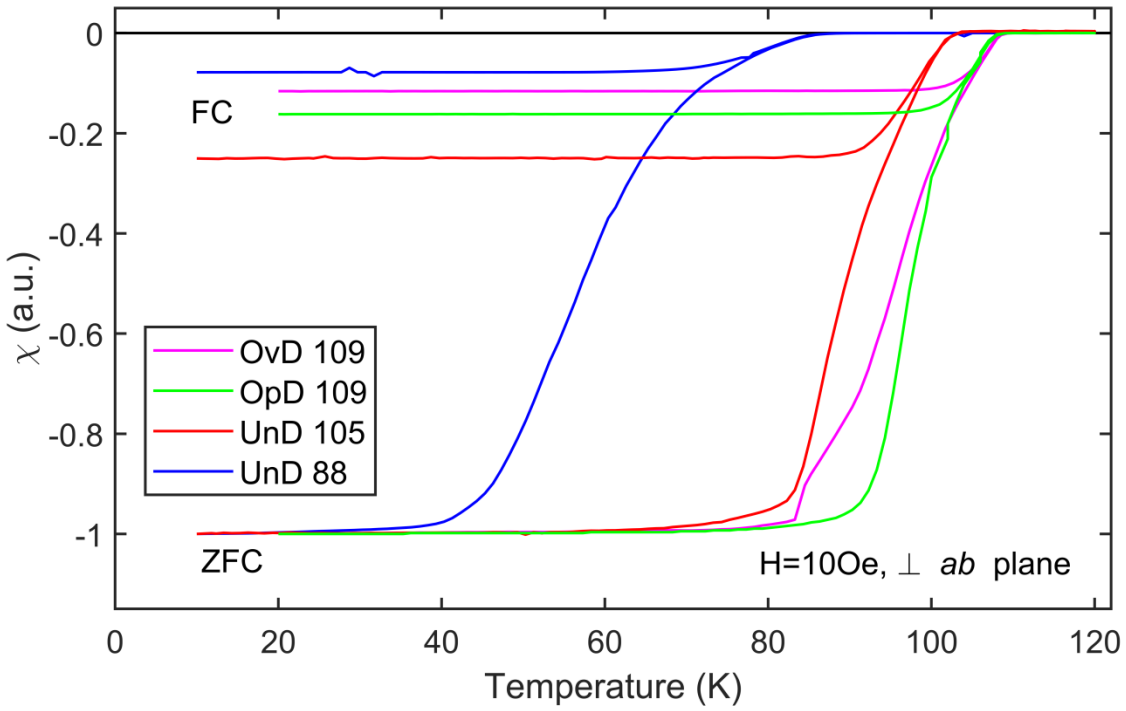

Fig.4.3 Magnetic susceptibility of all the Bi2223 samples measured. The susceptibility values have been normalized by the low temperature ZFC value. In the legend the chosen nomenclature for the samples is used.

Sample Name	T_C (K)	Δ_{Tc} (K)	$T_{ANNEALING}$ (°C)	O_2	Ann. Time
OvD109	109	8	400	100%	5 days
OpD109	109	9	500	100%	50 hours
UnD105	105	13	700	100%	5 days
UnD88	88	18	600	P_{O2}≈2Pa	1-3 hours

Table 4.1 Summary of the Bi2223 samples measured. The assigned sample names together with T_C, broadness of the transition and annealing condition are shown.

on. The superconducting transition is sharp for the OvD109, OpD109 and UnD105 samples, but it is a little broader in the more strongly underdoped sample UnD88, and this can be seen in Table 4.1. The broadness increases monotonically from the overdoped to the more underdoped sample and this may be due to the difficulty in obtaining homogeneous underdoped sample.[125]

Fig.4.4 Shows the XRD pattern for all the samples examined. The visible peaks correspond to the Bi2223 peak previously reported in the literature [125], [126] and are all assigned to (0 0 *l*) peaks. The more intense peaks are labelled on the optimally doped sample XRD spectrum in the second panel of Fig.4.4. From these spectra using the formula (3.22) the *c*-axis length can be extracted. The value was extracted from the 4 most intense peaks: (0 0 10), (0 0 12), (0 0 14) and (0 0 24) peak. These give slightly different values of the *c*-axis length; therefore the value was averaged between them. The obtained *c*-axis length for each peak and the averaged value for each sample are summarized in Table 4.2. As it can be seen, the value monotonically increases in the four samples for all of the examined peaks and therefore also in the average value. Since the *c*-axis length increases with decreasing oxygen content,[131] these values testify that the doping level

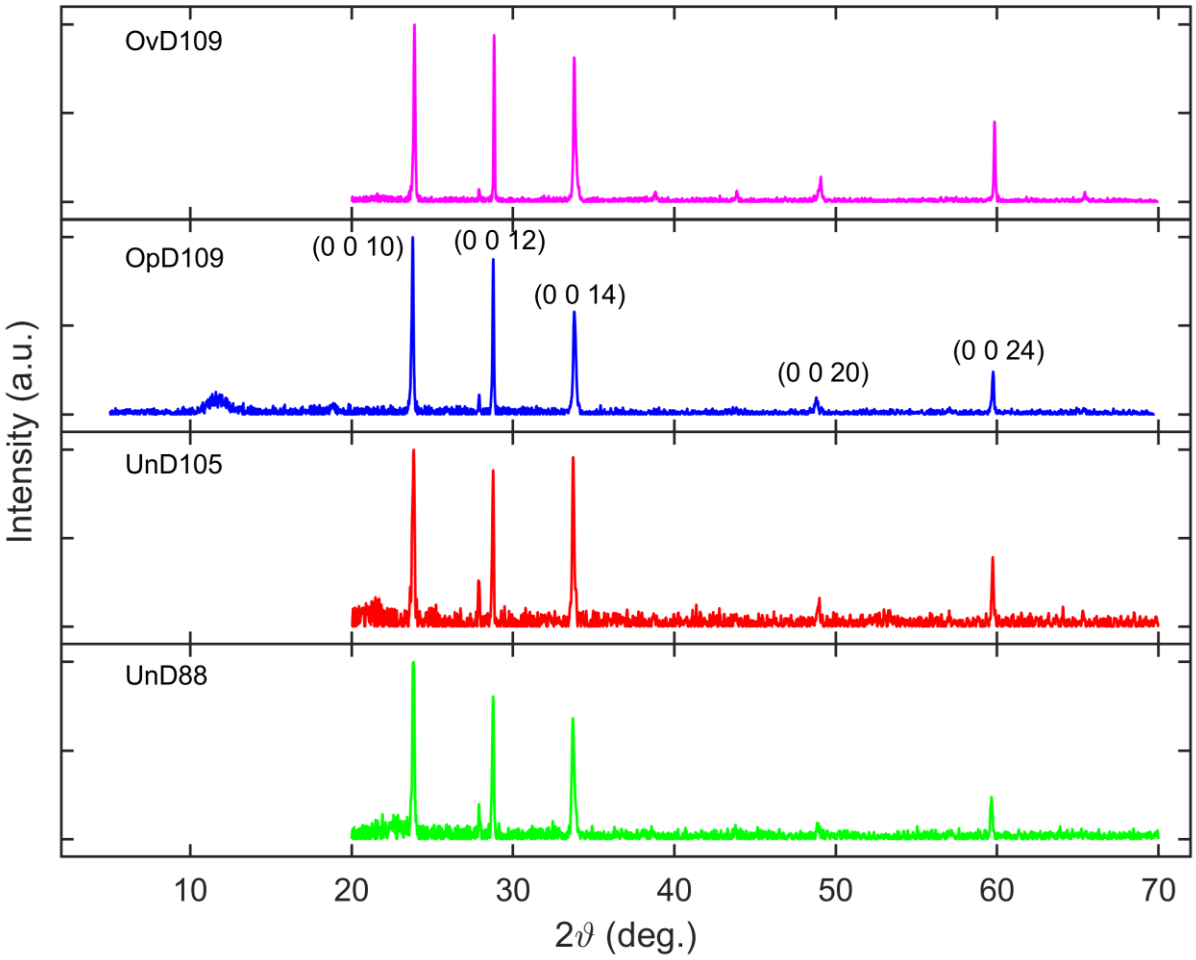

Fig.4.4 XRD diffraction pattern for all the Bi2223 samples examined, going from the overdoped sample above to the most underdoped one on the bottom.

Sample Name	(0 0 10) (Å)	(0 0 12) (Å)	(0 0 14) (Å)	(0 0 24) (Å)	Mean *c*-axis (Å)
OvD109	37.236	37.154	37.127	37.092	37.152
OpD109	37.251	37.168	37.143	37.102	37.166
UnD105	37.313	37.230	37.201	37.157	37.225
UnD88	37.340	37.237	37.222	37.202	37.250

Table 4.2 Extracted *c*-axis values, for all the samples, from the different peaks and average *c*-axis value obtained.

truly decreases as expected from the annealing condition and the magnetic susceptibility measurement. In particular, the overdoped sample *c*-axis is shorter than the optimally doped sample one. Therefore, even though the T_C of these two samples is the same, the oxygen content and the doping level is different. The obtained mean *c*-axis length range from 37.152 Å in the overdoped sample to 37.250 Å in the underdoped sample and these values are roughly consistent with the previous reports for Bi2223. [125], [126], [131] A more detailed analysis of the XRD pattern is outside of the goal of this work and has already been done by the sample grower, [125], [126] therefore we will not discuss a more precisely peak assignment and the width of the peaks.

4.2 Raman Results

The ERS spectra for the optimally doped sample are shown in Fig.4.5 (a,b). Here as explained before, the electronic and phononic contributions overlap, with sharp peaks being due to phonons and the electronic contribution giving the background. In the following discussion, the phonon peaks observed are of little interest. Phononic peaks are observed in both configurations. In B_{1g} we have the phonon peaks at ≈110 cm^{-1}, 255 cm^{-1} (which is the most intense) and 590 cm^{-1}, while in B_{2g} we have the phonon peaks at ≈115 cm^{-1}, 380 cm^{-1}, 460 $cm^{-1}$and 580 cm^{-1}. The lower frequency ones are associated with the heavier Sr or Ca ions vibrations, while the higher frequency ones are associated with the oxygen vibrations.[155]

Moving on to the electronic contribution, for the antinodal B_{1g} configuration in Fig.4.5 (a), going from room temperature (RT) to lower temperature there are two ways the spectrum modifies. The first is a suppression of spectral weight at low frequency below ≈600 cm^{-1}, and the second is the appearance of the two peaks at higher frequency (≈560 cm^{-1} and ≈800 cm^{-1}). As to the former, going from RT to 115K, we have the loss of spectral weight between 200 and 600cm^{-1} that is caused by the pseudogap opening.[134], [143], [156], [157] The pseudogap manifests itself in this manner in the Raman spectra, which is a subtle suppression of the spectral weight in the antinodal B_{1g} configuration starting from the pseudogap energy value ω_{PG}. Since this suppression is so minute, in this study we cannot draw strong conclusions on the value of the pseudogap energy. The suppression is evident at ≈600 cm^{-1}, but it could start at higher energy such as 800 cm^{-1}. For a better discussion on the pseudogap value by Raman, spectra with better signal to noise ratio must be taken at temperatures above and below T*, but this is outside the scope of this work.

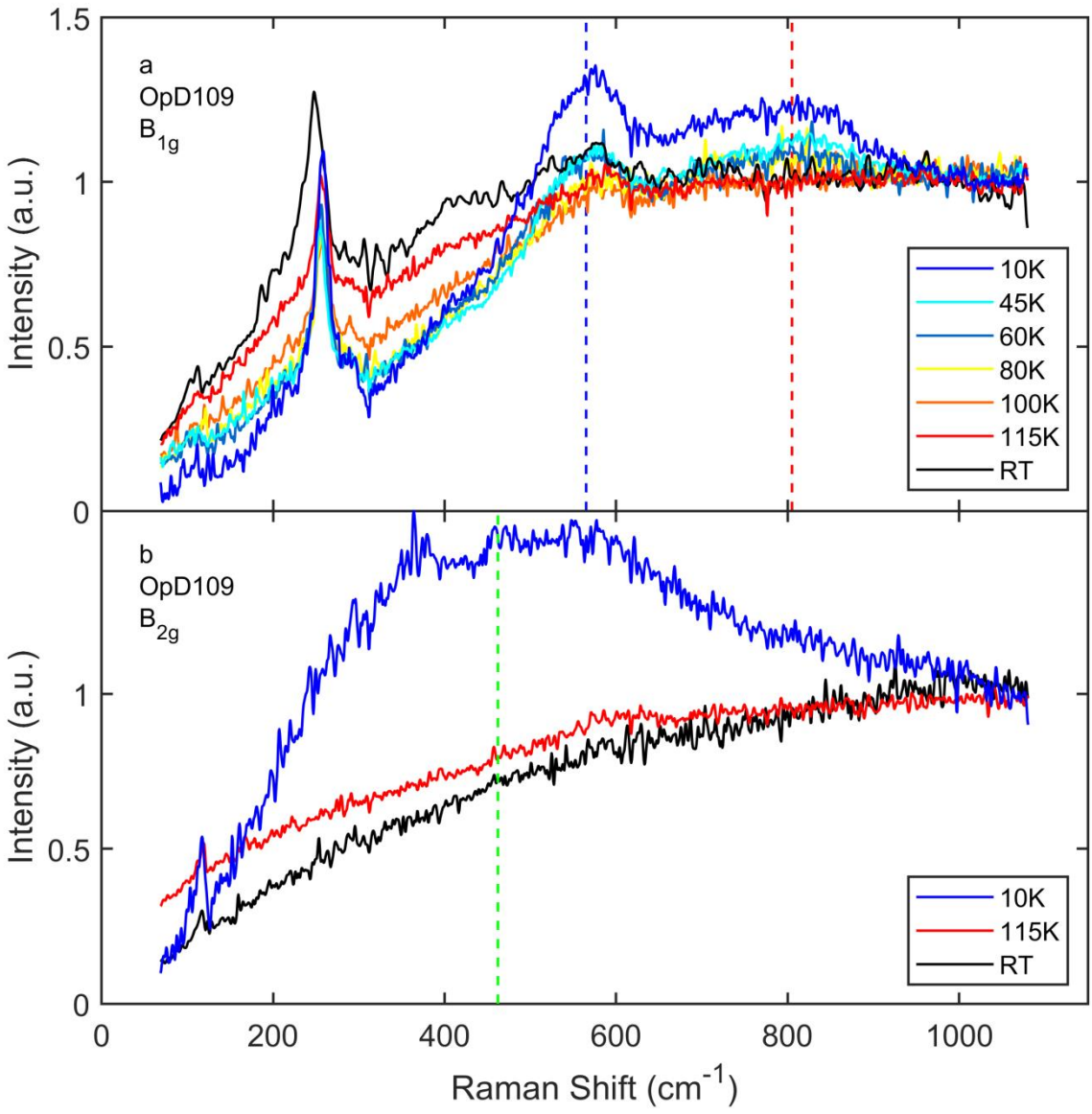

Fig.4.5 Bi2223 Raman spectra for the OpD109 sample with T_C=109K. **a** Antinodal B_{1g} spectra. At low temperature a double pair breaking peak is visible. **b** Nodal B_{1g} spectra. At low temperature a single pair breaking peak is visible.

At $T<T_c$(=109K), a more dramatic suppression is observed below 500cm^{-1}, which is due to the superconducting gap opening.

The second change in the spectra is the appearance of the two peaks at ≈560 cm^{-1} and ≈800 cm^{-1} below T_C. As discussed before this kind of peaks are associated with the Cooper pair-breaking into two Bogoliubov quasiparticles with a transition across the superconducting gap, and are therefore associated with superconductivity. The new observation in this work is that, not one but, two pair breaking peaks are visible, and we attribute this to the double superconducting gap of Bi2223. Basing on the other techniques that found a signature of the double gap in Bi2223, which are ARPES[123] and NMR[130], the peak at lower energy is assigned to the pair-breaking peak in the

outer plane (OP) and the one at higher energy is assigned to that of the inner plane (IP). Such a double peak structure has never been reported so far in Raman spectra, and is in clear contrast with the single peak shown by the double layered $Bi_2Sr_2CaCu_2O_8$ Bi2212, [48], [49], [133]–[135] and the other double or single layered compounds[46], [47], [136]. As discussed in section 2.6, triple layer cuprates have been examined before by Raman,[137]–[141] but no signature of a double gap has been reported. Most of these work are quite old, therefore this may be due to sample quality issues or instruments limitations. However we note that in some recent data on the triple layer Hg1223 a double pair braking peak could be visible, although it was not identified by the authors[138].

Unfortunately the oxygen phonon present at ≈590cm^{-1} is quite close to the OP superconducting peak at ≈560 cm^{-1} and this may create some confusion. For example it may mislead to think that the OP pair-breaking peak does not disappear above T_C, even though this is not the case. Also it could lead to the idea that the double peak is an artefact, and that the lover peak is in fact just a phonon peak. However we strongly believe that this is not the case for multiple reasons. Firstly, the difference in frequency between the phonon peak above T_C and the peak at low temperature is quite large, too large to be a simple phonon shift induced by temperature. Secondly, the peak at low temperature is too broad (≈100 cm^{-1}) to be a phonon peak. In general, phonons become sharper, not broader with lower temperature. Finally the intensity of this peak is too big with respect to the small phonon peak above T_C and this is even more evident in the overdoped sample, which is discussed later and shown in Fig.4.6 (a).

We have carefully measured the temperature dependence of the spectra to check whether the two peaks start to develop at different temperatures or not (see Fig.4.5 (a)). However, within our measurement resolution, no clear difference was observed in the onset temperature for the peak development. The density of Cooper pairs at temperature just below T_C is low, making the signal weak, and therefore no peak is visible at 100K, and at 80K the two peak are both visible even if extremely weak. This assessment is furtherly complicated by the oxygen phonon at ≈590cm^{-1} which may conceal the appearance of the OP peak. Therefore the simultaneous appearance of these two peaks may be an artefact created by experimental limitation; however it may also be the real behaviour of the sample. In that case it indicates that the two superconducting gaps open simultaneously, although the doping is different in the IP and in the OP. In NMR data on different multilayer samples it seems that even though the T_C of the two layer is different, the layer with higher T_C drives the other layer to superconductivity.[9] However, since these data are on powder samples, and not single crystal, it is still an open problem to understand if superconductivity appears at the same temperature on the two layers.

On Fig.4.5 (a) the peak position is marked with red and blue dashed lines for the OP and IP respectively. These peak positions have been extracted from the subtracted intensity plot, which will be discussed later on, in Fig.4.7. These energy values found for the B_{1g} peak positions in the optimally doped sample are roughly in good agreement with the ARPES data from Ref. [123].

The nodal B_{2g} spectrum for the optimally doped sample is shown in Fig.4.5 (b). Here at 10K a double pair–breaking peak is not visible. Instead a single, very broad peak appears. It is expected

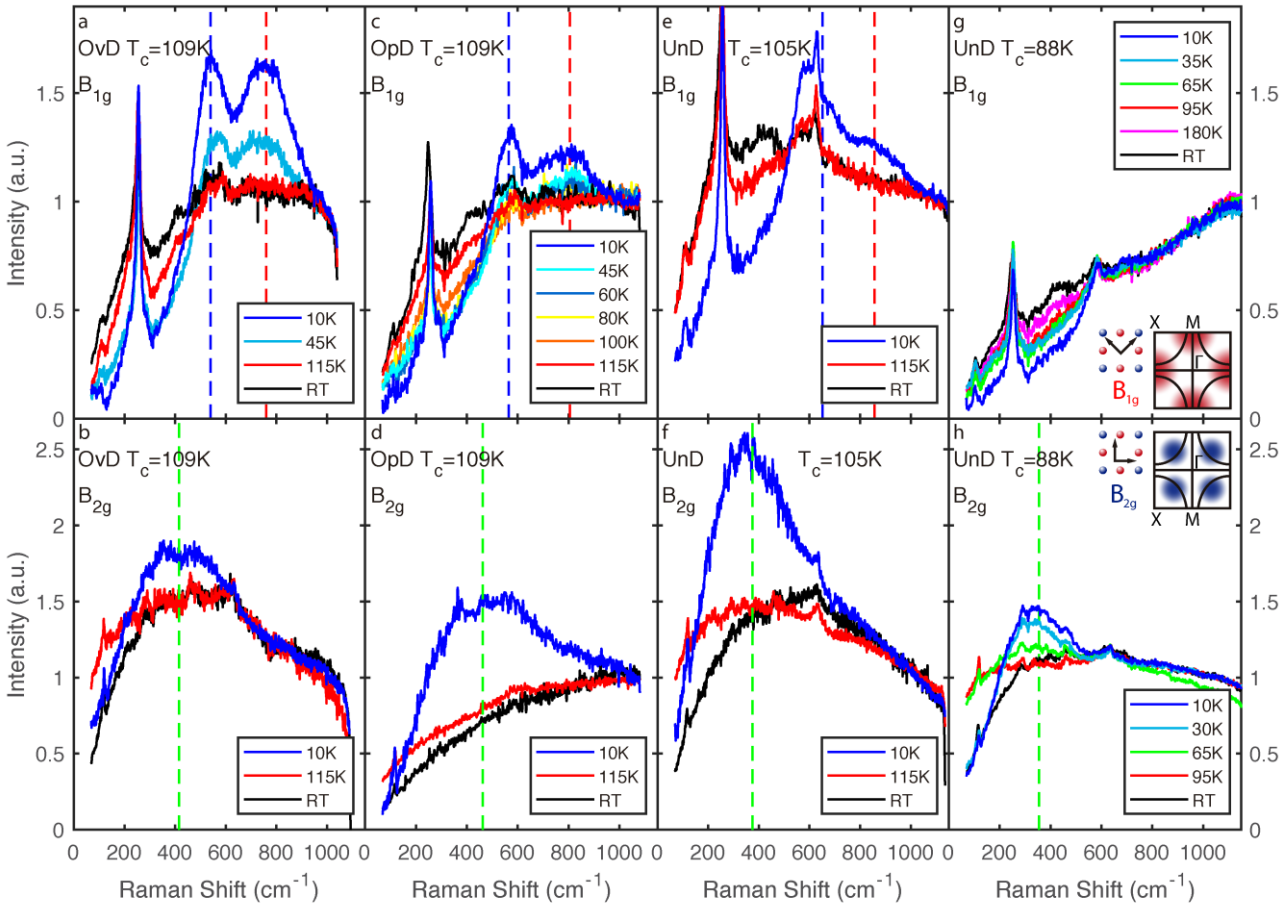

Fig.4.6 B_{1g} and B_{2g} Raman spectra of Bi2223 for OvD109 (a,b), OpD109 (c,d), UnD105 (e,f) and UnD88 (g,h) samples. The OP and IP peak positions are indicated by blue and red dashed lines, respectively in panels a, c and e. The single peak observed in the B_{2g} configuration is indicated by a green dashed line in panels b, d, f and h. The precise peak positions have been extracted by the subtracted intensity plot in Fig.4.7

that due to the smaller values of the superconducting gaps in the nodal region and the originally broad feature for B_{2g}, the two peaks, even if they exist, overlap with each other, forming a single broad peak.

In Fig.4.6 the B_{1g} and B_{2g} Raman spectra for all the samples examined are shown, going from the overdoped sample (OvD109) on the left to the strongly underdoped one (UnD88) on the right. In Fig.4.6 (a) the antinodal B_{1g} spectra for the OvD109 sample is shown. Here the double pair breaking peak structure is observed and is even more intense and clearer than the one in the optimally doped sample. When the doping level slightly increases, the double B_{1g} peaks are observed at slightly lower energies than the ones of the optimally doped sample (see Fig.4.6 (a) dashed lines compared with Fig.4.6 (c) dashed lines). The pseudogap opening is still visible in the overdoped sample going from RT to 115K, as a small suppression of the low energy spectral weight. In B_{2g} configuration also in the overdoped sample a single pair breaking peak appears, and this is visible in Fig.4.6 (b). In contrast with the B_{1g} peaks, the B_{2g} peak appears at almost the same energy or a slightly lower energy than in OpD109, as shown in Fig. 4.6 (b). The differences

between the spectra of OpD109 and OvD109 proves, together with the differences in the *c*-axis length extracted from XRD, that the doping levels of these two samples are different although the T_c values are almost the same.

Next, in Fig. 4.6 (e) and (f), the spectra for the slightly underdoped sample (UnD105) are shown. In the low temperature B_{1g} spectrum in Fig. 4.6 (e), the double peak feature is still visible, even though not as clearly as in the optimally and overdoped sample. Again the pseudogap opening is visible as a suppression of spectral weight between 200 and 500cm^{-1}, going from RT to 115K. In the B_{2g} configuration in Fig. 4.6 (f), a strong but broad single peak is visible at 10K.

Figures 4.6 (g) and (h) show the spectra for the strongly underdoped sample (UnD88). Here in the B_{1g} configuration in Fig.4.6 (g) no pair breaking peak seems visible. This is likely to be due to the suppression of the B_{1g} Raman intensity in the underdoped region which was reported in the other cuprates and particularly in the previous reports for Bi2212[47]–[49], [135]. It can be explained with the confinement of Cooper pairs in the nodal region with underdoping[50] which, as discussed previously is likely to be caused by the pseudogap. This is consistent with the tunnelling[51], [52] and the ARPES data[53]–[55]. Here the pseudogap opening is clearly visible when the temperature decreases. Contrary to B_{1g}, the pair-breaking peak in nodal B_{2g} configuration is clear and intense, as it can be seen in Fig.4.6 (h), and this was also shown by previous reports for the other single and double layer cuprates, and is visible in the right panel of Fig.2.22. Since the pseudogap is an antinodal phenomenon it is expected that the suppression with underdoping influences mainly the antinodal B_{1g} peak but little the nodal B_{2g} Raman pair breaking peak.

To better view the redistribution of spectral weight due to superconductivity, we subtract the spectra just above T_c from the 10K spectra. This is shown in Fig.4.7(a) and (b) for the B_{1g} and B_{2g} configuration, respectively. In Fig.4.7 (a) for the B_{1g} spectra the double peak structure can be seen more clearly for most of the samples. For the slightly underdoped sample the double peak structure, which was not so clear from the raw spectra in Fig.4.6 (e), becomes evident. For the strongly underdoped sample although a peak was too weak to be seen in the raw data, it becomes visible in Fig.4.7 (a). On close inspection this peak is visible also in Fig.4.6 (g) even though it is extremely weak. We attribute this to the pair-breaking peak of the outer plane OP. Considering that the inner plane IP should be more underdoped than the OP and therefore suppressed more, it is reasonable that the IP pair-breaking peak does not appear, and only the OP peak is visible. From this figure we can extract the peak positions more precisely, since we are cancelling the phonon contribution, almost entirely, with the exception of their modifications due to the change in temperature, and we are eliminating the electronic contribution not caused by superconductivity. The extracted peaks positions are indicated by the dashed lines. For the B_{1g} configuration the maximum of the subtracted spectra was taken as the peak position, whereas for B_{2g} configuration this approach would lead to big uncertainty due to the broad peak. Therefore for B_{2g} configuration we defined the peak position as the middle point between the two frequencies where the intensity is half the maximum value. From this figure we also defined error bars for the

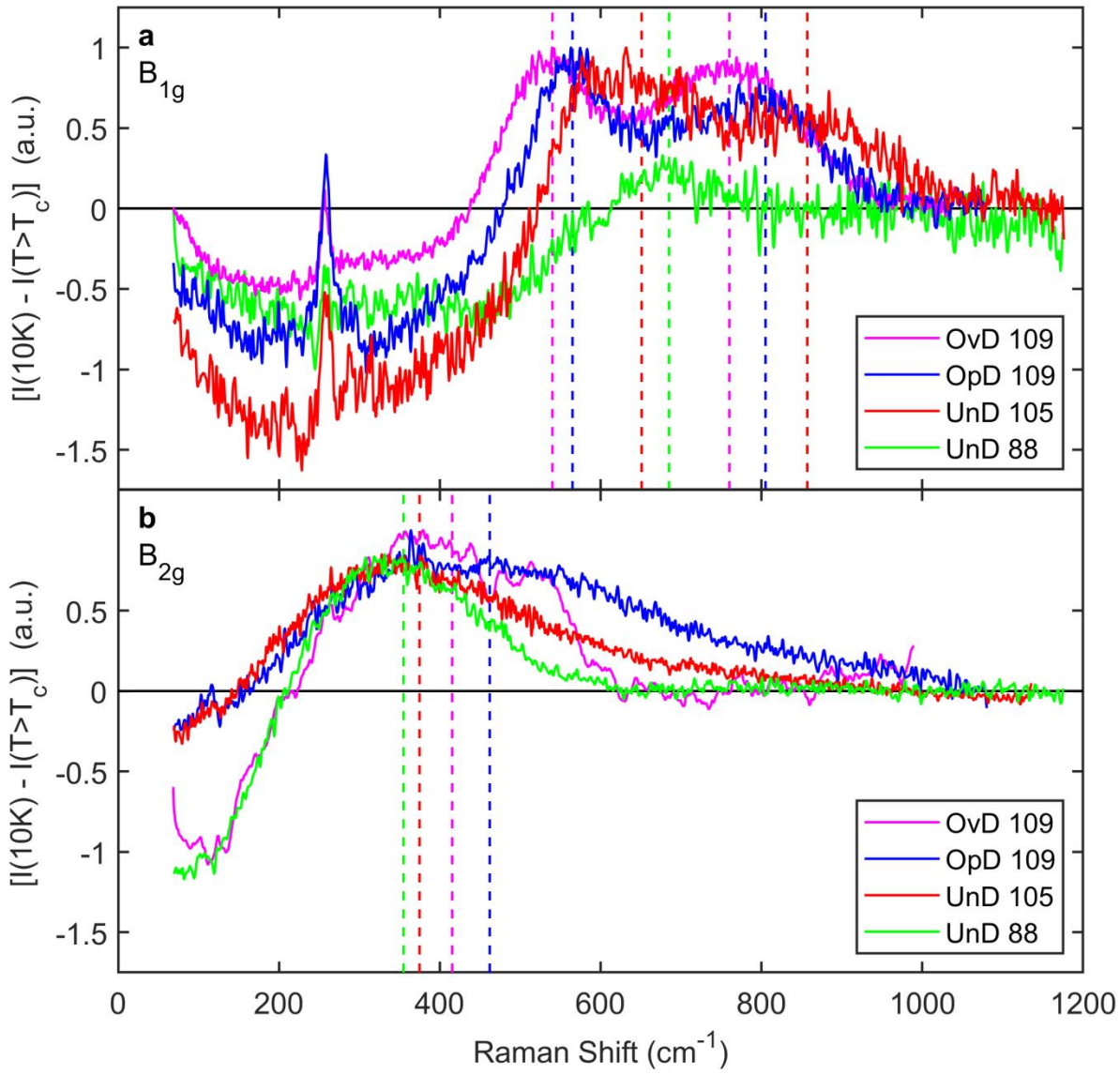

Fig.4.7. Low temperature Raman spectra of all samples after the subtraction of the spectra just above T_C. The peaks positions are extracted from this figure and indicated by the dashed lines. **a** Antinodal B_{1g} high-T subtracted spectra. The double peak structure becomes clear for the OvD109 sample, OpD109 sample and the UnD105 sample. The peak of the OP becomes visible for the UnD88 sample. **b** Nodal B_{2g} high-T subtracted spectra.

peaks positions, as the frequency where the 50% and 75% of the maximum intensity value of the peak is reached, for B_{1g} and B_{2g} respectively. While the B_{1g} peak monotonically shifts to higher energy and loses intensity with lower doping, both for IP and OP, the B_{2g} peak shifts to lower energy when going from the optimal to the underdoped samples. This opposite doping dependence of the peak position in the underdoped regime is consistent with the previous reports for the double and single layer cuprates and is commonly referred as two energy scale behaviour,[46]–[49] which was discussed in the previous sections. However, to better discuss the doping dependence, we need to determine the actual layer doping for each of the IP and OP, and this will be discussed in the next section.

4.3 Average and Layer doping determination

As discussed in the previous sections, in multilayer cuprates with 3 or more Cu-O layers the IP and OP layers doping levels are different and do not correspond to the average sample doping. In order to visualize the doping dependence of the two energy gaps, we need to estimate the doping level of the IP and OP for all the samples. For the optimally doped sample the available NMR data[130] provide an estimate of the IP and OP doping levels, basing on the Cu Knight shift, which depends on the carrier concentration around the Cu atoms. A linear relationship between doping and Cu Knight shift was observed and calibrated for the other cuprates of known doping.[9] This relationship was used to calculate the layer doping of the IP and OP in the optimally doped Bi2223, finding the values of p(OP)=0.203 and p(IP)=0.127, respectively. Therefore for the optimally doped sample these two experimental values can be used.

For the other samples, since such measurements are not available, a way to evaluate the layer doping is needed. For this we start by estimating the average sample doping. For the underdoped samples this can be done from the decrease of T_C. The parabolic relationship between T_C and the average sample doping *p*, was used since the early days of the research on cuprates and is expected to be valid, even if it could be a rough approximation, especially for triple layer cuprates. This is given by: $T_c/T_{c,max}=1—82.6\ (p-0.16)^2$ [35], [36]. From this formula, assuming that the optimally doped sample average doping is $p_{AVERAGE,OpD}=0.16$ we can obtain the average sample doping for the two underdoped samples $p_{AVERAGE,UnD}$. To obtain the layer doping, we assume that the doping shift of each layer from the average doping of the sample does not change with the sample. Therefore we can calculate this shift for the optimally doped sample as: $\Delta p_{OpD}(OP) = 0.203 - 0.16 = 0.043$ and $\Delta p_{OpD}(IP) = 0.16 - 0.127 = 0.033$. Assuming that $\Delta p(OP)$ and $\Delta p(IP)$ are constant, we can calculate the layers dopings as:

$$p_{UnD}(OP) = p_{AVERAGE,UnD} + \Delta p_{OpD}(OP) \quad (4.1)$$

$$p_{UnD}(IP) = p_{AVERAGE,UnD} - \Delta p_{OpD}(IP) \quad (4.2)$$

This may be a rough way to determine the layer doping, but we expect it to be valid as a first approximation.

For the slightly overdoped sample, since the T_c is the same as the optimum value, we cannot use this method to estimate the doping level. As an alternative way, we can use the *c*-axis lattice parameter determined by XRD. Assuming that the *c*-axis length is linearly proportional to the doping level (oxygen content), we can determine the average doping also for the overdoped sample. We firstly plot the $p_{Average}$ value versus the *c*-axis length for the optimally doped sample and the two underdoped sample, and this is shown in Fig.4.8 (blue dots). By fitting these known points with a linear function (red line in Fig.4.8), we can extrapolate the obtained function to the *c*-axis length of the overdoped sample, obtaining the average doping of the overdoped sample (red dot in Fig.4.8). With this estimated value ($p_{Average,OvD} \approx 0.1697$) we can calculate the layers

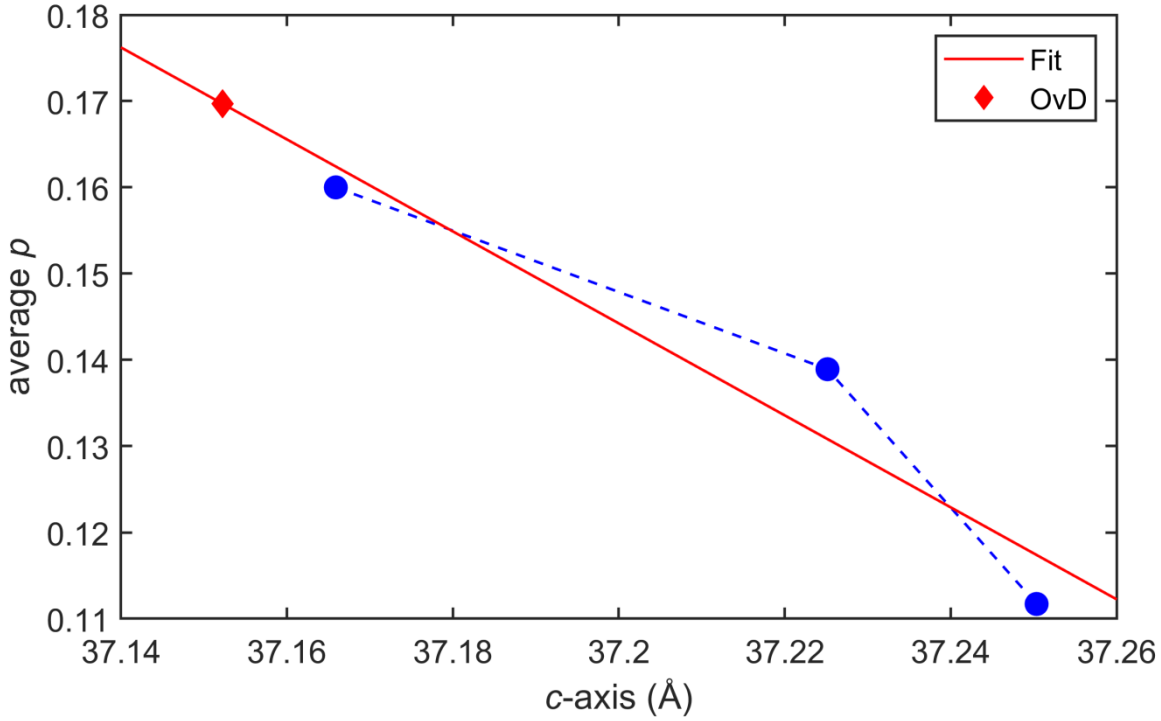

Fig.4.8 Average doping of the samples versus the *c*-axis length. The 3 blue point represent the optimally doped and underdoped samples where the average doping was obtained from the parabolic relationship between T_C and *p*. The red line is the linear fit of these 3 points. The red dot is the average doping of the overdoped sample obtained assuming the linear fit.

Sample Name	$p_{AVERAGE}$	*p*(OP)	*p*(IP)
OvD109	0.1697	0.213	0.137
OpD109	0.16	0.203	0.127
UnD105	0.1389	0.182	0.106
UnD88	0.1117	0.155	0.079

Table 4.3 Summary of all the assumed or calculated dopings for all the samples, including the average doping, the OP and IP layers dopings.

dopings for the overdoped sample using the same formulas (4.1) and (4.2) for the OP and IP, respectively. The doping levels determined for all samples, both the average and the layer dopings, are summarized in Table 4.3. As it can be seen, according to our doping estimation, the outer plane is overdoped in all samples, except for the strongly underdoped one, where it becomes slightly underdoped. The inner plane is underdoped in all samples. In the strongly underdoped one the doping value *p*(IP)= 0.0787 is close to the minimal doping where superconductivity disappears p_{min}=0.05, therefore, it is reasonable that superconductivity is confined in the nodal region and no superconducting IP peak is observed in the antinodal B_{1g} Raman spectra of this sample.

Using these layer doping values we can discuss properly the doping dependence of the double superconducting peak structure observed in the Raman spectra.

4.4 Doping dependence of the Raman peaks

We use the layer doping values determined in the previous section (and summarized in Table 4.3) to plot the B_{1g} pair-breaking peak energy as a function of the Cu-O layer doping in Fig.4.9. Since the double peak structure is not observed in B_{2g}, we can only plot the energy value of the single B_{2g} peak as a function of the average sample doping and not of the layer one.

Both IP and OP B_{1g} peak energies increase with decreasing doping, as expected from the previous reports on different cuprates. [46]–[49] However, here the striking result is that, when the difference in doping between the two layers is taken into account, the B_{1g} peak energies of the IP and OP align on a single line. This is surprising since the two layers are chemically inequivalent, but the peak energy does not seem to be affected by these differences basing on this result. In other words it seems that the doping level is the only parameter determining the peak energy. However this conclusion is based only on the doping values examined here, and a more solid evidence would come if overlapping doping levels for the two layers were available. Nonetheless this unifying picture of the behaviour of both layers is surprising and may not be incidental.

The B_{2g} peak energy seems to be following the superconducting dome, which is the expected behaviour of the single and double layer compounds as discussed in section 2.6. However, this could be an artifact and not the real behaviour for multiple reasons. Firstly, since the double peak structure is not resolved, we cannot separate the IP and OP peaks energies. The different doping levels of these two layers mean that two different doping dependences could be overlapping, giving an artifact doping dependence. Additionally the originally broad B_{2g} peak gives strong uncertainty on the peak position determination, and this can be seen in the large error bars in Fig.4.9. Finally it must be considered that we did not examine a large doping window with our four samples, which is necessary to reveal a clear dome shape in the case of other single and double layer cuprates. For all the above reasons we believe that we cannot draw strong conclusions on the B_{2g} doping dependence.

The present result is, to our knowledge, the first doping dependent spectroscopic study on the triple layer Bi2223. The doping dependence found here is qualitatively consistent with the reports on the single and double layer cuprates [46]–[49]. Namely, the two energy scale behavior discussed in section 2.6 has been confirmed also in the triple layer compound. As discussed in section 2.6, the continuous increase of the superconducting B_{1g} peak energy with decreasing doping is strange, if we consider that the nodal ARPES gap, which is commonly associated with superconductivity, was found to be constant over a broad range of doping[2] (see Fig.2.10). This problem is common for the triple layer and the single and double layer cuprates, since the same doping dependence has been found. A possible explanation for this inconsistency is to assume a

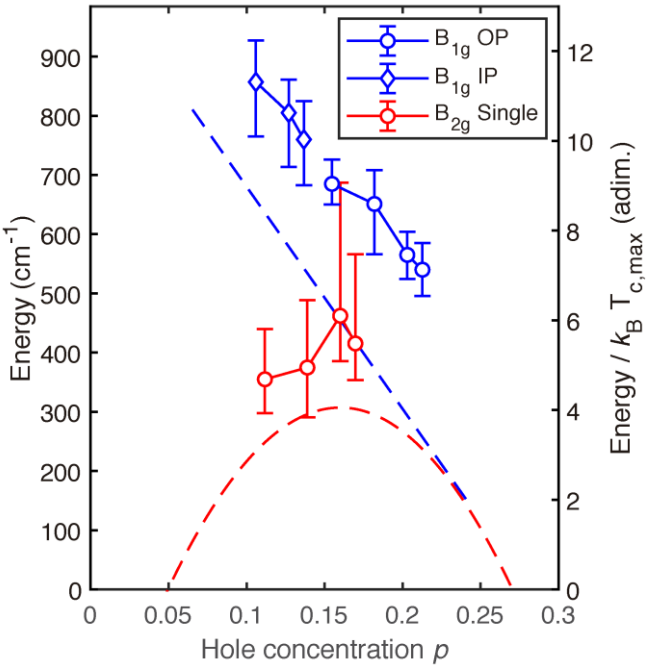

FIG. 4.9 Doping dependence of the pair breaking peak energy. The antinodal B_{1g} energy is plotted using the estimated OP and IP doping. The B_{2g} peak energy is plotted as a function of the estimated average doping. The dashed line and curve are the doping dependence curves taken from Fig.2.22 taken from Ref. [47] where the peak energy of single and double layer cuprates collapse when divided by $T_{c,max}$.

certain degree of positive interaction between superconductivity and the pseudogap or strong correlation called “Mottness”. The deviation from d-wave gap in the antinodal region is normally associated with the pseudogap and, as discussed previously, this deviation and therefore the antinodal gap increases with lower doping, as indicated by ARPES[43], [44]. However, since this deviation is assumed to be due to the pseudogap, it should not influence the superconducting Raman peak energy, and this is supported by the fact that with decreasing doping the B_{1g} peak disappears gradually, due to the competitive relationship with the pseudogap. If, on the other hand, we assume some degree of interaction between superconductivity and the pseudogap, even though superconductivity is suppressed, the superconducting gap value could be enhanced by the increasing pseudogap in the antinodal region, and this could explain the increasing B_{1g} peak energy with lower doping. In this picture superconductivity and the pseudogap do compete with each other, explaining the loss of the B_{1g} peak intensity, but at the same time they have some degree of positive interaction, explaining the increasing B_{1g} peak energy.

Here we also introduce another scale in the right axis of Fig.4.9, the peak energy (PE) divided by $k_B*T_{c,max}$, which should be close to 3.5 in a BCS superconductor if the PE corresponds to a double of the gap energy Δ. In Ref. [47], it was demonstrated that this ratio of various single and double layer compounds collapse on a universal doping dependence, and this plot is shown in Fig.2.22. This universal doping dependence is plotted with dashed lines in Fig.4.9 both for B_{1g} and B_{2g} configurations. It is clear from this figure that for both B_{1g} and B_{2g} the PE/$k_B*T_{c,max}$ ratios are larger

in Bi2223 than the ones for the other single or double layered cuprates. This suggests a larger energy scale of the pair-breaking peak, compared with T_c in Bi2223.

The characteristic feature of Bi2223 with respect to the other single and double layer cuprates of Fig.2.22 is the coexistence of different doping layers in a unit cell, where the lower doping CuO-layer (IP) is sandwitched by the higher doping CuO-layers (OP) as discussed in the previous sections.

The high T_c value and the large gap energy could be attributed to this feature, and are therefore likely to be multilayer effects. Experimentally we observe only a single superconducting transition, but not a double step transition, with the two Raman peaks appearing at the same temperature. It means that the IP and OP are not completely independent but interact with each other, although the result in Fig.4.9 seems to suggest that each layer behaves independently, showing no difference in their doping dependence which seemingly collapse on a single line.

Both of the high T_c (as previously discussed in section 2.4) and the large pair-breaking energy of Bi2223 can be discussed in terms of the multilayer effect. Firstly a high T_c value could be achieved on the IP due to the protection from the blocking layer disorders[8] or due to the appropriate next-nearest-neighbor hopping parameter t'[7], which originally gives a large gap value of the IP in a whole doping range. The IP gap might be further enhanced due to the previously proposed positive interaction with pseudogap, which should be strong on the IP due to the low doping level of this layer. In addition the OP gap could be also enhanced through the interlayer tunneling of Cooper pairs.[158] This effect may increase the OP gap value and decrease the IP gap value which is enhanced by the effects discussed above, and this would average out the two gaps value, giving two enhanced IP and OP gaps that align on a single doping dependence as seen in Fig.4.9. Another effect of this interlayer coupling may be the enhancement of the superfluid density of the underdoped IP, and the combination of these effects may lead to the high T_c of Bi2223, and other triple layer cuprates.

In doing these considerations on the T_C, in addition to these positive effects, we need to consider a negative effect of the pseudogap on superconductivity. Since the T_C is suppressed by the pseudogap in general, it is likely that the bulk T_C of Bi2223 is lowered by the pseudogap which should be strong in the underdoped IP. The combination of these two kind of effects, namely the enhanced gap energy together with the suppressed T_C can explain why the ratio of $PE/k_B*T_{c,max}$ observed in Fig.4.9 is much larger in Bi2223 than in the other single and double layer cuprates of Fig.2.22.

5: Analysis based on ARPES

5.1 Bi2212 Analysis

5.1.1: Calculation Input preparation

To calculate the Raman spectra starting from the ARPES data using the Kubo formalism, described in section 3.3, the first step is the treatment of the ARPES raw data. The samples that were analysed, both by ARPES and Raman, are one overdoped (T_C=85K), one optimally (T_C=92K) and one underdoped (T_C=75K) sample named OD85K, OP92K and UD75K, respectively. The ARPES data are obtained by synchrotron radiation ARPES for the optimally doped and underdoped samples and by He lamp ARPES for the overdoped sample. The ARPES and Raman experiments for the Bi2212 samples were performed by my colleagues from my same laboratory (Tajima Lab. Osaka University). The experimental details of said ARPES experiments have been reported in section 3.4 and will not be repeated here.

Firstly the Fermi vector k_F must be identified, and this was done by inspection of the momentum distribution curves MDC for as many ARPES cuts as possible. This procedure can be successfully performed only in the nodal and intermediate region, since the band is dispersive in these areas of the momentum space. On the other hand this cannot be done in the antinodal ARPES cuts, since the band becomes flat and non-dispersive in these areas of the momentum space due to strong correlation effects, and this can be seen clearly for all the samples ARPES cuts in Fig.5.2, Fig.5.4 and Fig.5.6. For these antinodal cuts the k_F position was obtained later through the tight binding fits. The experimental ARPES angles of acquisition, which determine the positon of the data in the momentum space, are subject to experimental errors, therefore these must be corrected, through the procedure of ARPES mapping. For this procedure a large fast scan over the one whole Brillouin zone was taken, and the angles were corrected by ensuring the correct symmetry of the k_F positions. The higher resolution data which are used for the calculation are corrected to be consistent with the k_F positions of the faster scan.

The result of our ARPES Fermi surface mapping can be seen in Fig.5.1, Fig.5.3 and Fig.5.5 for the optimally doped, underdoped and overdoped samples, respectively. Thanks to the symmetry of the cuprates, only half of a Brillouin zone quadrant must be measured for the calculation, and the present data span this area almost entirely, with only a small area missing close to the nodal region and the Γ point in the dataset for the optimally and underdoped sample.

In Fig.5.2, Fig.5.4 and Fig.5.6 we show all of the ARPES cuts for the optimally, underdoped and overdoped sample, respectively. Here the profile of the bands along the cut, starting from the Γ-M line can be seen, and the evolution of the band from the nodal to the antinodal region is visible. The opening of the superconducting gap can be clearly seen going from the ungapped nodal cuts to the antinodal cuts where the gap is the largest. As discussed earlier, ghost bands which are created by the modulation of the Bi-O layers are present in the ARPES data of Bi2212,[129] and are also observed here. The ghost band intensity must be avoided, and this is easily done by the

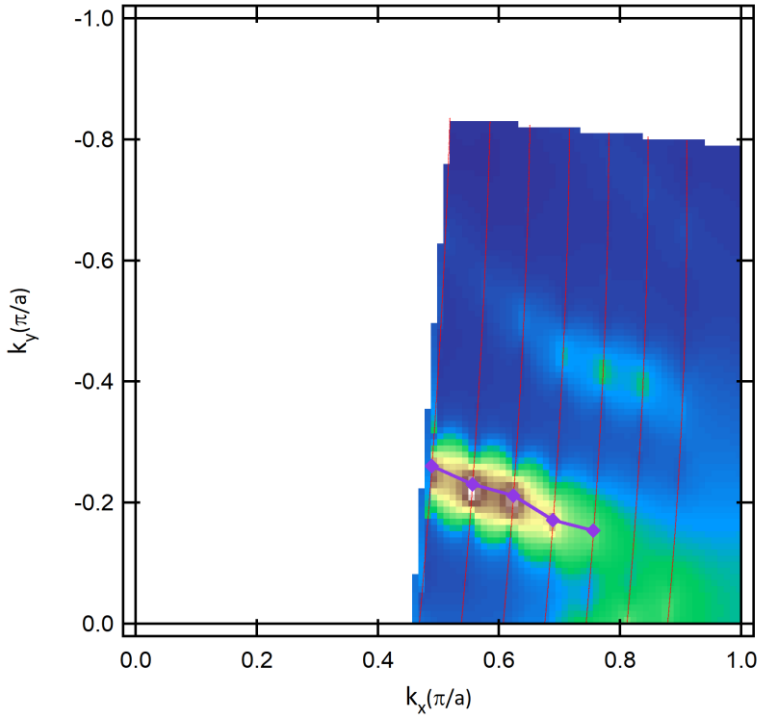

Fig 5.1 ARPES data mapping for the optimally doped sample, the extracted Fermi vectors are represented by the purple diamonds.

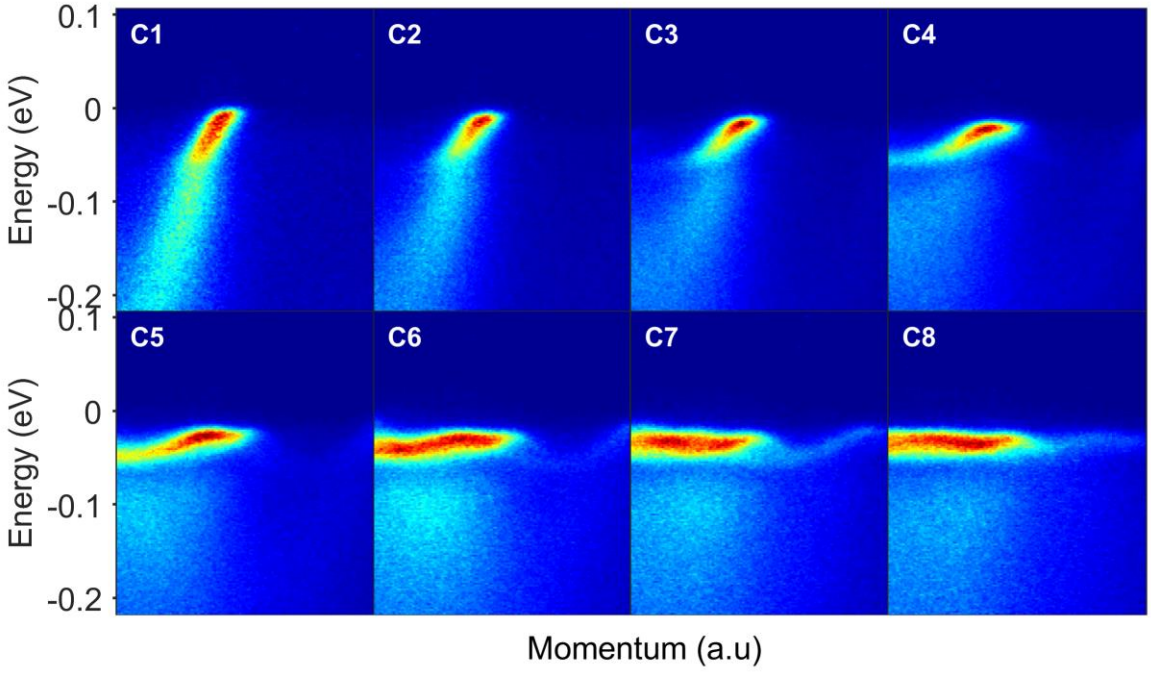

Fig.5.2 ARPES cuts for the optimally doped Bi2212 sample, going from the node in C1 to the antinode in C8

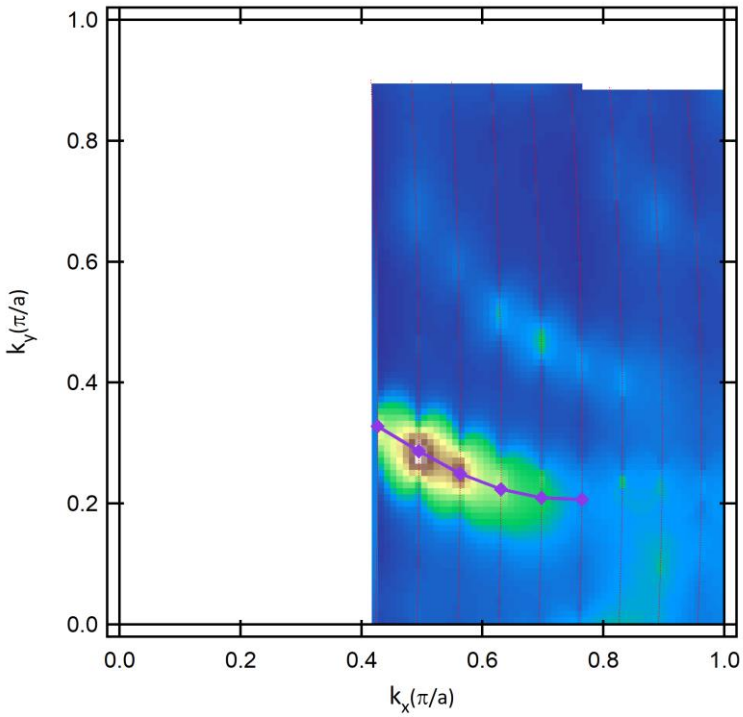

Fig.5.3 ARPES data mapping for the underdoped sample, the extracted Fermi vectors are represented by the purple diamonds.

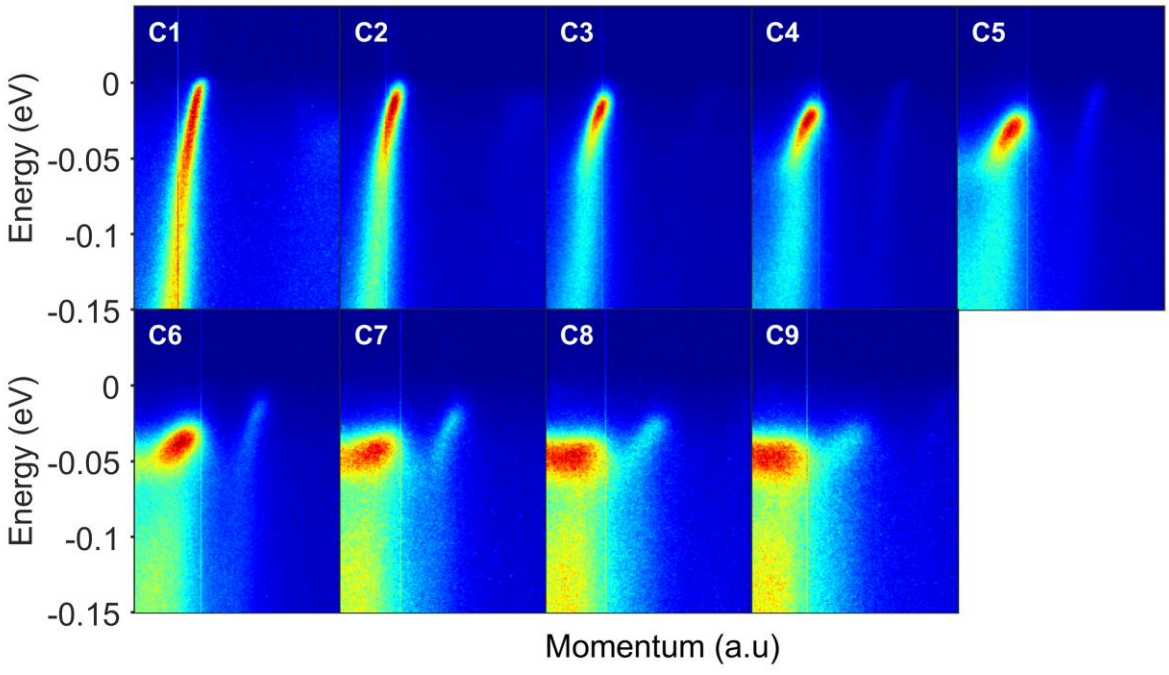

Fig.5.4 ARPES cuts for the underdoped Bi2212 sample, going from the node in C1 to the antinode in C9

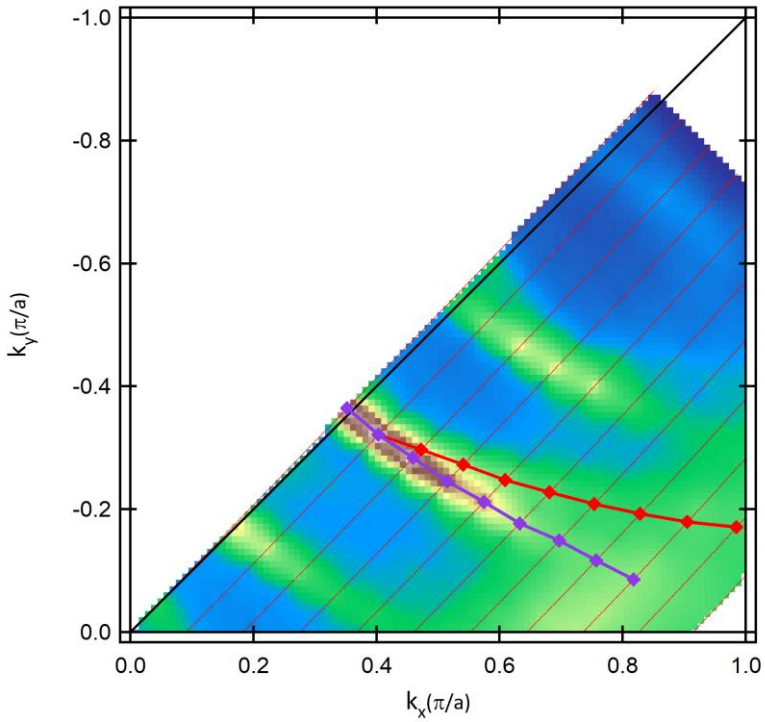

Fig.5.5 ARPES data mapping for the underdoped sample, the extracted Fermi vectors are represented by the purple diamonds for the antibonding band AB and by the red diamonds for the bonding band BB.

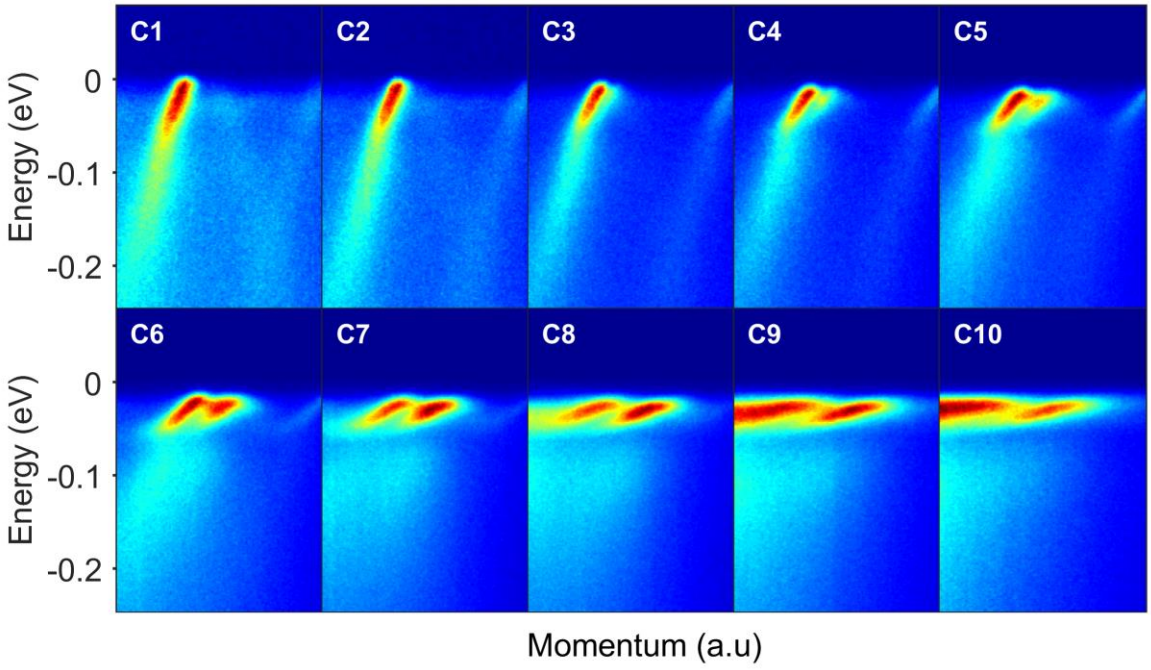

Fig.5.6 ARPES cuts for the overdoped Bi2212 sample, going from the node in C1 to the antinode in C10. Two bands are present due to the multilayer band splitting: the bonding BB and antibonding AB bands.

correct choice of BZ quadrant. Additionally, some of the well-known anomalies of the bands are observed here, like the kinks in the band dispersions and higher energy features below the main band in the antinodal region.[159]–[161] These anomalies are likely to be due to strong correlation effects, and, in the case of the kinks, to electron phonon interaction. These present an obstacle for the calculation since: firstly the tight binding cannot model them, and second since the high energy intensity in the antinodal region will be a mixture of ARPES background and real signal that should contribute to the Raman spectra and these two must be separated for the calculation.

In the overdoped sample the previously discussed band splitting is visible, as it can be seen in Fig.5.5 and Fig.5.6. The lower energy band is the bonding band (BB) while the higher energy band is the antibonding band (AB). Both bands should contribute to the Raman spectra, therefore in this work their contribution to the spectra was calculated separately and then summed up.

Using the k_F determined experimentally from the MCD inspection, we performed a tight binding fitting of the bands. The tight binding function can be used as a rough approximation of the bare band of the superconductor in the normal state above T_C. As previously discussed, the anomalies of the bands caused by strong correlations, like the kinks and the flat dispersionless bands in the antinodal region, cannot be modelled by the tight binding function. However, we expect it to be valid as a first approximation. Recalling here the formula used for the tight binding fit:

$$\xi_{\boldsymbol{k}} = -2t\left(\cos k_x a + \cos k_y a\right) + 4t' \cos k_x a \cos k_y a - 2t''\left(\cos 2k_x a + \cos 2k_y a\right) - \mu \quad (5.1)$$

Here the free parameters are t, t' and μ while the next-next nearest neighbor hopping parameter t'' was fixed for simplicity to be half of the next nearest neighbor hopping parametert'. To fit both band in the overdoped sample the simpliest band splitting term was used:

$$E_{bi} = -\frac{t_\perp}{4}\left(\cos k_x a - \cos k_y a\right)^2 \qquad (5.2)$$

The points used for the fitting are the experimentally determined k_F and a band bottom value at Γ taken from literature. The resulting fit parameters are summarized in Table 5.1.

The obtained band functions are shown along the ARPES cuts in Fig.5.7, and the obtained Fermi surface are shown together with the experimental k_F in Fig.5.8. The obtained fitting parameters are roughly consistent with the previous reports.[21] The bilayer splitting term is quite large compared to the values found in literature. The experimental k_F position is quite well reproduced

	t (eV)	t’ (eV)	t’/t	u (eV)	t’’ (eV)	t ⊥ (meV)
UD fit02	0.27860	0.07535	0.27046	-0.25528	t’/2	n.a.
OP fit08	0.29328	0.073758	0.25150	-0.32714	t’/2	n.a.
OD fit02	0.27551	0.06905	0.25062	-0.29590	t’/2	88.773

Table 5.1 Summary of all the resulting fit parameters for all the Bi2212 samples. t’’ is fixed to be half of t’. The bilayer splitting term was applied only to the overdoped sample, where the band splitting is observed.

a

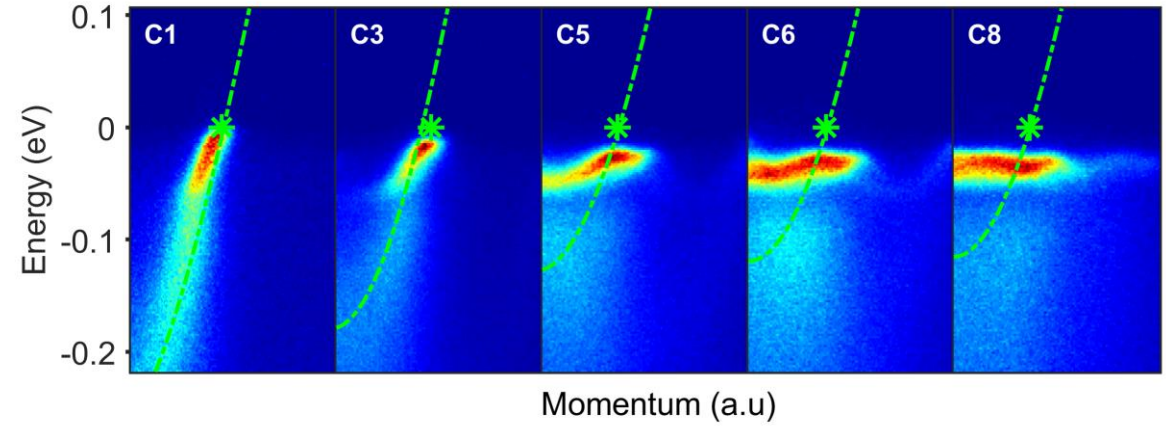

b

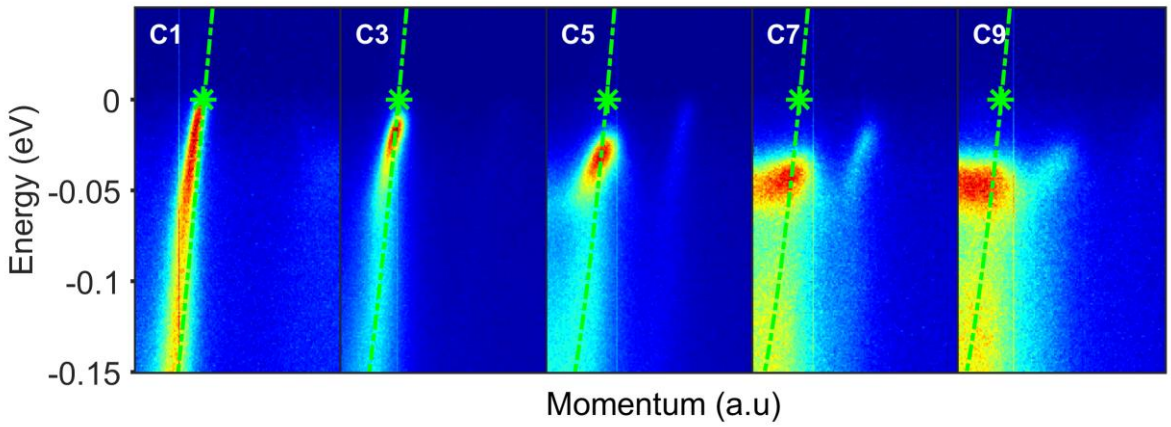

c

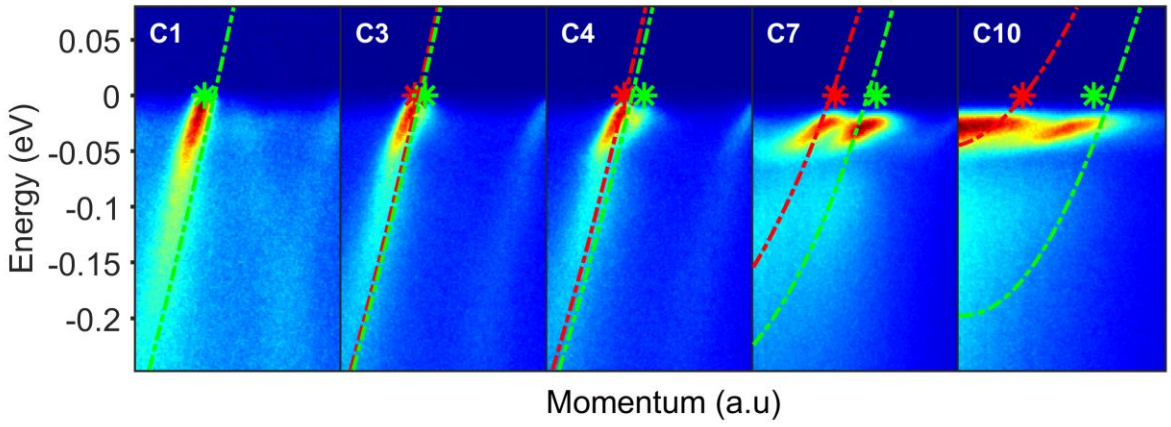

Fig.5.7 Tight binding fit results along the ARPES cuts for **a** the optimally doped, **b** the underdoped **c** the overdoped samples. The k_F displayed are determined experimentally until cut 5, 6 and 9 for the AB and 10 for the BB in the 3 samples. After these cuts the k_F displayed are determined from the tight binding function in the antinodal region.

as it can be seen in Fig.5.7 and Fig.5.8. In Fig.5.7 both the experimental k_F position, in the nodal and intermediate region, and the k_F position determined from the tight binding, in the antinodal region, are shown. The k_F determined experimentally are from the first cut to cut 5, 6 and 9 for the AB and 10 for the BB in the optimally underdoped and overdoped samples, respectively. From this figure it can be seen how the tight binding fails to model the anomalies of the band. In particular, the kink in the band around -0.05 eV and the flat dispersionless band in the antinode cannot be modelled. However this is sufficient for the present calculation.

In Fig.5.8 we can see how the Fermi surface shifts towards the origin of the Brillouin zone with increasing doping, even if there is only a small shift going from the optimally doped to the overdoped sample. In doing this consideration, for the overdoped sample the band with no bilayer splitting term can be considered, since this term shifts the AB band towards Γ and the BB band away from it. This shift of the Fermi surface towards the origin of the BZ with increasing doping is the expected trend and shows that the mapping and the tight binding have a consistent doping behaviour. If we recall the Kubo formula:

$$\chi''_{\gamma\Gamma} = \frac{2}{\pi V}\sum_{\boldsymbol{k}} \gamma_{\boldsymbol{k}}\Gamma_{\boldsymbol{k}} \cdot \int_{-\infty}^{\infty} (f_\omega - f_{\omega+\Omega})\, G''_{\boldsymbol{k},\omega} G''_{\boldsymbol{k},\omega+\Omega} \left(1 - \frac{\Delta_{\boldsymbol{k}}^2}{(\omega+\xi_{\boldsymbol{k}})(\omega+\Omega+\xi_{\boldsymbol{k}})}\right) \qquad (5.3)$$

we see how the tight binding has multiple uses in this calculation. Not only the calculated function enters directly as the bare band function $\xi_{\boldsymbol{k}}$, but it is also used to obtain the k_F positions in the antinodal region. Additionally the tight binding function is also used to determine the superconducting gap value along the cut $\Delta_{\boldsymbol{k}}$. This is done by obtaining the position of the band at low temperature and calculating $\Delta_{\boldsymbol{k}}$ as the quadratic difference between the tight binding and the low temperature band. This is seen in Fig.5.9 where the calculated $\Delta_{\boldsymbol{k}}$ is shown along the ARPES cut by the green curve, together with the tight binding function and the experimental low temperature band. Here it is again evident how the tight binding fails to model the flat dispersion towards the antinode. However this is not problematic for the calculation, since the tight binding enters in the Kubo formula (5.3) only when $\Delta_{\boldsymbol{k}} \neq 0$ as the bare band $\xi_{\boldsymbol{k}}$. Therefore by using a $\Delta_{\boldsymbol{k}}$ function as the one shown in Fig.5.9, which is non-zero only between k_F and the point where the superconducting experimental band and the tight binding band have the same value, the limitations of the tight binding will not influence the calculation. The tight binding function enters in the equation only in a limited region of the momentum space, where the superconducting gap opens, therefore even if the tight binding is not a good model the real band, we can expect it to be a valid first approximation of the bare band in this limited momentum region.

The calculation is done for each ARPES cut between the Fermi vector and the point where the cut reaches the (0,0)-(π,π) line in the momentum space. This calculation interval is shown in Fig.5.9 by the two vertical white lines. The weight of the band quickly becomes zero after k_F, therefore as a first approximation it was not considered. The background was subtracted from these EDCs inside the calculation interval, using the Shirley background shown in the equation (3.12) in an iterative matter, as seen in Fig.3.7, and assuming that the intensity at the highest binding energy is completely composed by background. As mentioned early, a difficulty comes from the fact that

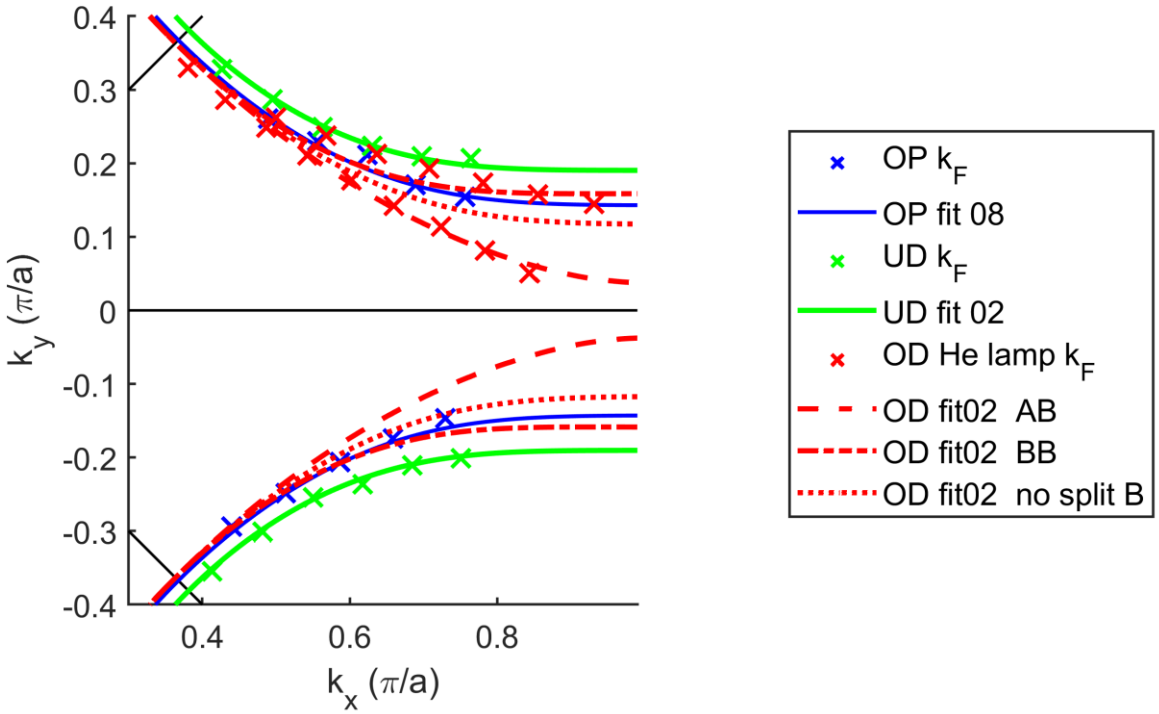

Fig.5.8 Resulting tight binding fit Fermi surface together with the experimentally obtained Fermi vectors for all the samples. For the overdoped sample the AB and BB bands are shown together with the band with no bilayer splitting term (red dotted line)

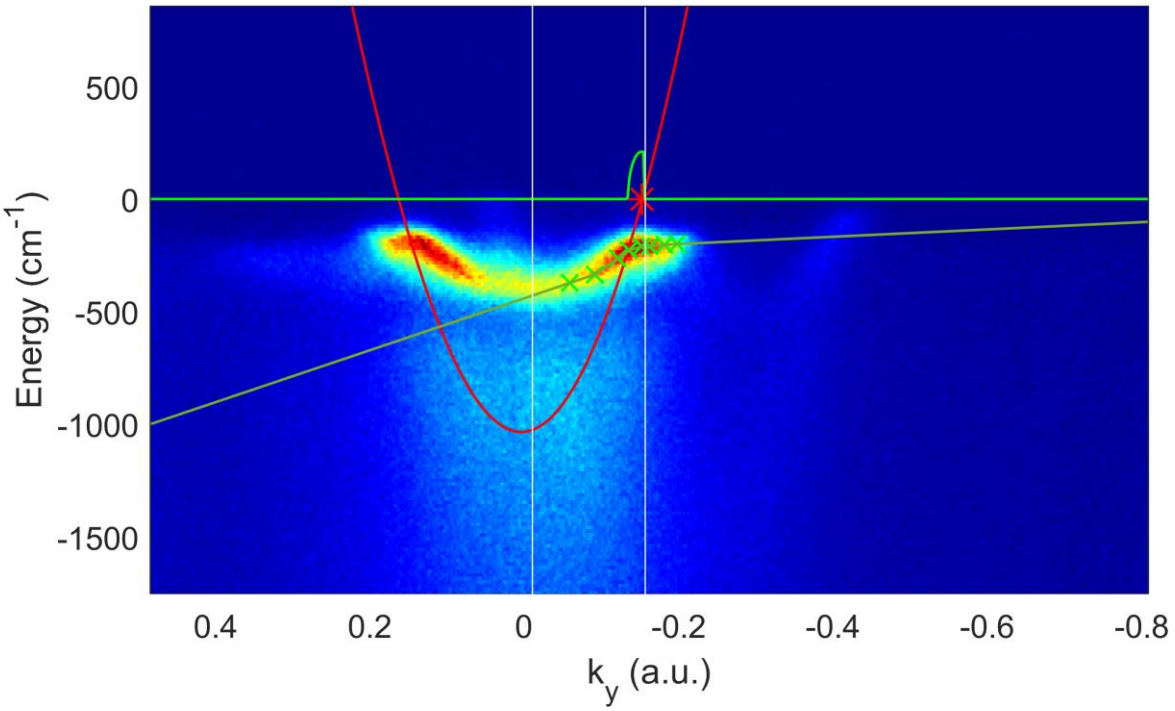

Fig.5.9 Example of superconducting gap Δ_k calculation along the cut (green line), and other inputs for the calculation. The tight binding function is shown by the red curve, the low temperature experimental band by the green cross marks and their interpolating function. The calculation interval is between the two vertical white lines.

the high energy anomalies in the antinodal region introduce some uncertainty. For example, how much the high energy intensity is composed by background, and how much by the anomalies that should contribute to the Raman signal. This could cause some uncertainty on the intensity of the high energy side of the calculated Raman spectra, with respect to the intensity of the peaks that are given by the band at the lower energy. The Green function $G''_{\boldsymbol{k},\omega}$ is obtained from the ARPES intensity with the equation (3.10) and (3.11), assuming the matrix element to be constant. Since the Green function of the unoccupied states is needed for the calculation, a symmetric behavior of the band with respect to the Fermi level was assumed. This should be valid in the case of a particle-hole symmetric superconducting band. Therefore the EDCs were symmetrized with respect to the zero energy. The intensities of the all ARPES cuts were normalized by the maximum intensity value of the EDC at the Fermi vector k_F. This together with the assumed constant matrix element, means we are assuming initially a constant intensity profile along the Fermi surface.

The intensities of the two bands of the overdoped sample were separated to calculate their contribution to the Raman spectra separately. This was done by fitting the EDCs with 3 Gaussian peaks. Two peaks were used to fit one band each, while the remaining peak was used to fit the high energy features. An example of a similar EDC fit is shown in Fig.5.19 in the similar case of the inner plane and outer plane bands of Bi2223. The fit was done initially with completely free parameters; however this leads to good results only for the EDCs where both bands are clearly observed. For the EDCs where one of the two bands intensities is weak a different approach is needed. In this case the band position was fixed by examining the ARPES cuts and the peak position extracted by the fit in the EDCs where the intensity was strong enough. The width of the bands was also fixed by assuming a linear relationship between the width and the binding energy, and the slope of this relationship was assumed by observing the results of the fit where both band were intense enough. At low binding energy this linear relationship is not valid, therefore an appropriate width had to be assumed for the more nodal cuts at low binding energy, and this was again done by observing the results of the fit where the intensity was appropriately high. The results of these EDC fits are shown in Fig.5.10. As it can be seen from these obtained intensity images, the bonding and anti-bonding bands have been successfully separated in the region where they overlap. The abrupt change of intensity where the fit ends could not be avoided unfortunately. This is due to the intensity of one of the bands becoming too small to be fitted at that point. This residual may introduce some unwanted intensity in the calculation, but the effect should be small compared to the intensity given by the rest of the band. The high energy incoherent contribution was also fitted, and was inserted either in the BB or in the AB intensity, with attention not to double count this contribution in the momentum position where both bands contribution to the Raman spectra was calculated.

The ratio of the intensity of the two bands is an additional parameter in the case of multiple bands. The ARPES intensity can change heavily between two different bands because of the matrix element and the previously discussed orbital selectivity. Therefore this ratio is heavily influenced by experimental conditions such as photon energy and photon polarization. In this calculation, in order not to add too many different free parameters, we normalized the ARPES intensity of the

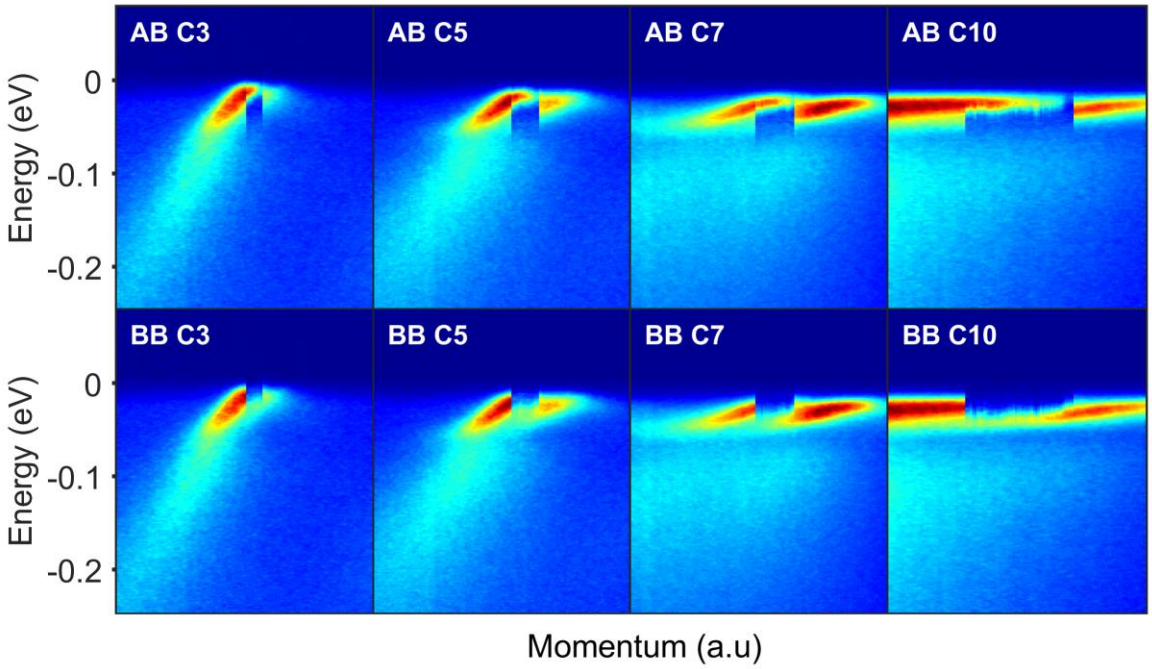

Fig.5.10 ARPES cuts after the subtraction of the fitted BB intensity (first row) and after the subtraction of the fitted AB band intensity. These intensities were used for the AB and BB calculations respectively.

two bands and sumed them up, therefore we performed the calculation assuming a band ratio equal to 1 for simplicity.

5.1.2: Calculation Results and Discussion

The results of the Bi2212 calculations assuming constant intensity profile along the Fermi surface, for all the samples, both in B_{1g} and B_{2g} configuration, are show in Fig.5.11 together with the experimental Raman spectra for these same samples.

Starting from the optimally doped sample, it can be seen in Fig.5.11 (c,d) that we obtain a good reproduction of the experimental Raman spectra. For the B_{1g} configuration in Fig.5.11 (c) we obtain a good reproduction of the peak position, which is only slightly overestimated. Regarding the shape of the calculated spectra we have only a small underestimation of the intensity at low frequency (below 350 cm^{-1}) and a small overestimation at higher frequency than the peak (at 650 cm^{-1}), therefore we have an overall really good reproduction of the shape of the experimental peak. The same can be said for the B_{2g} configuration spectra shown in Fig.5.11 (b). The overall shape is well reproduced, with only a small underestimation at low frequency (below 250 cm^{-1}) and a small overestimation at higher frequency (above 650 cm^{-1}). The peak position seems to be well reproduced, even though the peaks, both the experimental one and the calculated one, are really broad, and therefore there is a big error margin.

For the overdoped sample, the calculated and experimental Raman spectra are shown in Fig.5.11 (a) and (b) for the B_{1g} and B_{2g} configuration, respectively. Here both the AB and BB contribution is shown, with magenta and green dashed lines, respectively. Their contribution summed up with band ratio equal to 1, as discussed earlier, is shown by the red curve. In B_{1g} configuration in Fig.5.11 (a) the calculated AB and BB contribution are not so different between each other and

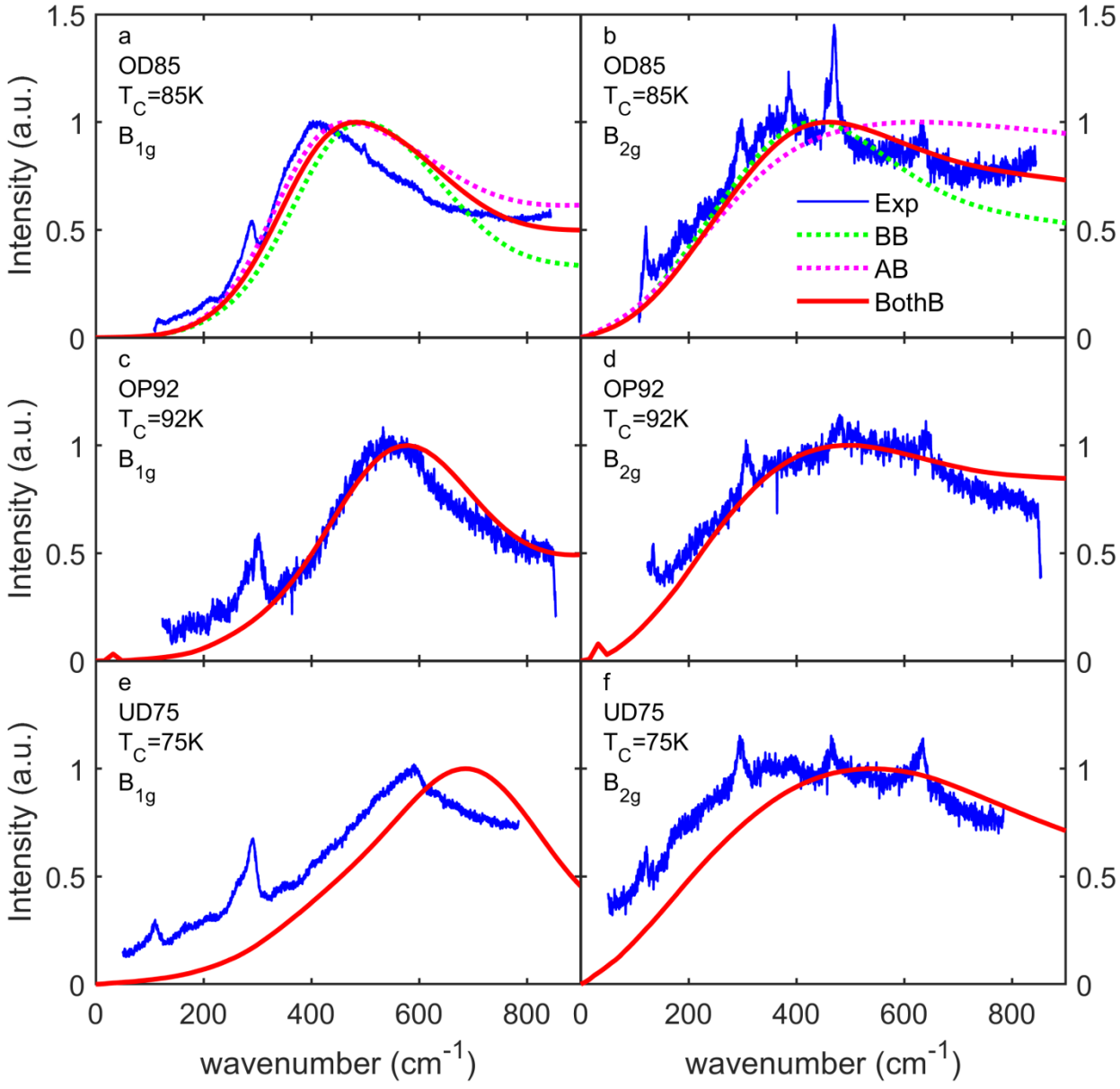

Fig.5.11 Experimental Bi2212 spectra together with the calculated spectra using the Kubo formula and assuming constant profile along the Fermi surface, for the overdoped sample in **a** B_{1g} and **b** B_{2g} configuration the optimally doped sample in **c** B_{1g} and **d** B_{2g} configuration and for the underdoped sample in **e** B_{1g} and **f** B_{2g} configuration. In the overdoped sample panels **a** and **b** both the AB and BB bands calculated contributions are shown by magenta and green dashed lines respectively. Here the red solid line represents the total contribution of both bands summed up with normalized intensity and band ratio equal to one.

quite similar to the experimental spectra. In both cases the peak position is slightly overestimated; therefore the summed calculated spectrum also overestimates the peak position. The intensity at high frequency is slightly overestimated in the AB band calculated spectra, and underestimated in the BB calculated spectra, but the total calculated spectra estimates quite well the ratio between intensity of the peak and high energy intensity. In B_{2g} configuration in Fig. 5.11 (b) the AB and BB bands show quite different calculated spectra. The BB peak position is quite good, with only a small overestimation of the peak position, while the AB calculated spectra shows a broad feature at high frequency in place of the peak. As in B_{1g} the high energy intensity is overestimated for the AB band but underestimated by the BB band. The total spectrum on the other hand, reproduces quite well the experimental B_{2g} spectra, overestimating only slightly the peak position and reproducing well the shape of the experimental spectra. Overall we can conclude that the experimental spectra of the overdoped sample are quite well reproduced, with only a small overestimation of the peak position, in both B_{1g} and B_{2g} configurations.

In Fig.5.11 (e,f) the underdoped calculated spectra are shown, and as it can be seen, we cannot reproduce well the shape of this sample spectra. For the B_{1g} spectrum in Fig.5.11 (e) we can see how the peak position is significantly overestimated, and this leads to a strong underestimation of the intensity at frequency lower than the peak frequency. It follows that the overall shape is not well reproduced. A similar situation presents itself in the B_{2g} configuration in Fig.5.11 (f). Again the peak position is overestimated and this lead to an underestimation of the intensity at frequency lower than the calculated peak. Also in this case the overall shape is not well reproduced.

Altogether we can conclude that a good reproduction of the experimental Raman peak was obtained, with the exception of the underdoped sample. The advantage of using the Kubo formula to calculate the Raman spectra starting from experimental ARPES data can be clearly seen when comparing these spectra to Kinetic theory calculation that use as input some assumed band profile. [38], [39] The overall shape is more realistic and the peaks are naturally broad as compared to the sharp peaks of the previous calculations. [47], [49], [142], [143] In the present work there is no need to introduce a scattering rate, which comes naturally from the experimental ARPES data. Another clear advantage of this approach is that here the anomalies of the band, such as the flat band dispersion in the antinodal region, are accounted for, unlike in the case of a calculation starting from an assumed tight binding dispersion.

Our calculation fails to correctly describe the underdoped sample and the doping dependence of the peak position, since the energy of the peak is constantly increasing with decreasing doping for both B_{1g} and B_{2g} configurations. However this is likely to be an effect of the pseudogap. As previously discussed in section 2.7 to correctly describe the underdoped sample peak position, a special profile of the quasiparticle spectral weight $Z\Lambda$ must be assumed.[47], [49], [142], [143] Here a decreasing weight is given to the antinodal region with decreasing doping, and this can give the correct B_{2g} peak positions and therefore the correct doping dependence. This decreasing quasiparticle spectral weight in the antinodal region with lower doping is justified by the effect of the pseudogap, which suppresses superconductivity and confines the Cooper pairs in the nodal region with decreasing doping.[50]–[55] In our calculation the ARPES cuts were normalized.

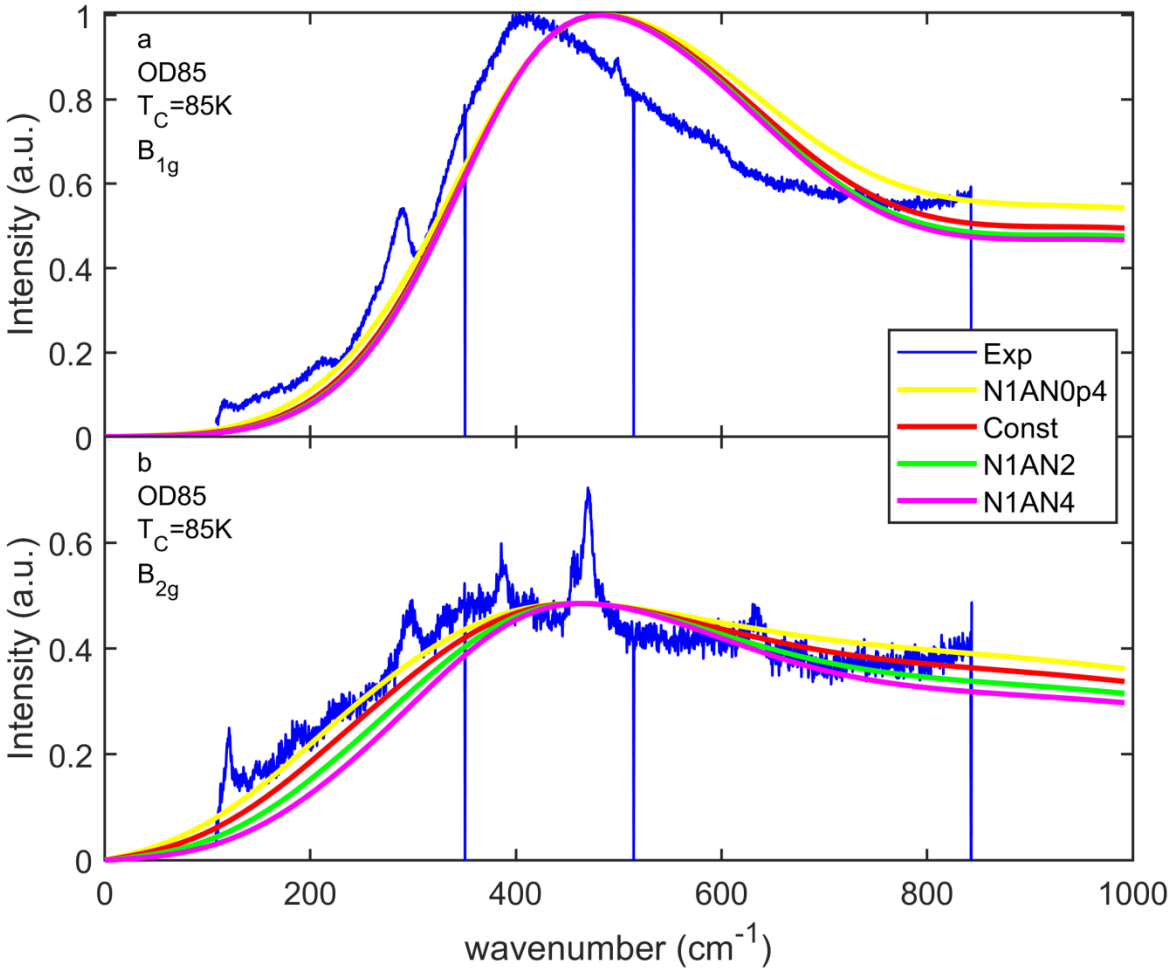

Fig.5.12 Experimental and calculated Raman spectra with different linear intensity profiles for the overdoped sample in **a** B_{1g} configuration and **b** B_{2g} configuration. These spectra are given by the sums of the AB and BB contributions, which are summed up with a band ratio equal to one as in the previous calculation.

Therefore, we considered a constant intensity profile along the Fermi surface. Additionally the matrix element was considered to be constant in the momentum, which is likely to be a rough approximation.

To try to model these two effects we change the intensity along the Fermi surface and repeat the calculation. For simplicity, linear intensity profiles are assumed, where the k_F positions are plotted against their *d*-wave positions $\left|\cos k_{F,x}a - \cos k_{F,y}a\right|$ and the intensity profile is assumed to be linear along this coordinate. In Fig.5.12 the calculation with different linear profiles for the overdoped sample, together with the experimental spectra are shown. These spectra are again obtained as a summation of the AB and BB bands contributions with a band ratio equal to one, as in the previous calculation for the overdoped sample. Here the nomenclature adopted for the intensity profile is N1ANx which means that the nodal value of the intensity profile is 1 while the antinodal value is x. x can be greater or smaller than one, enhancing or suppressing the antinodal

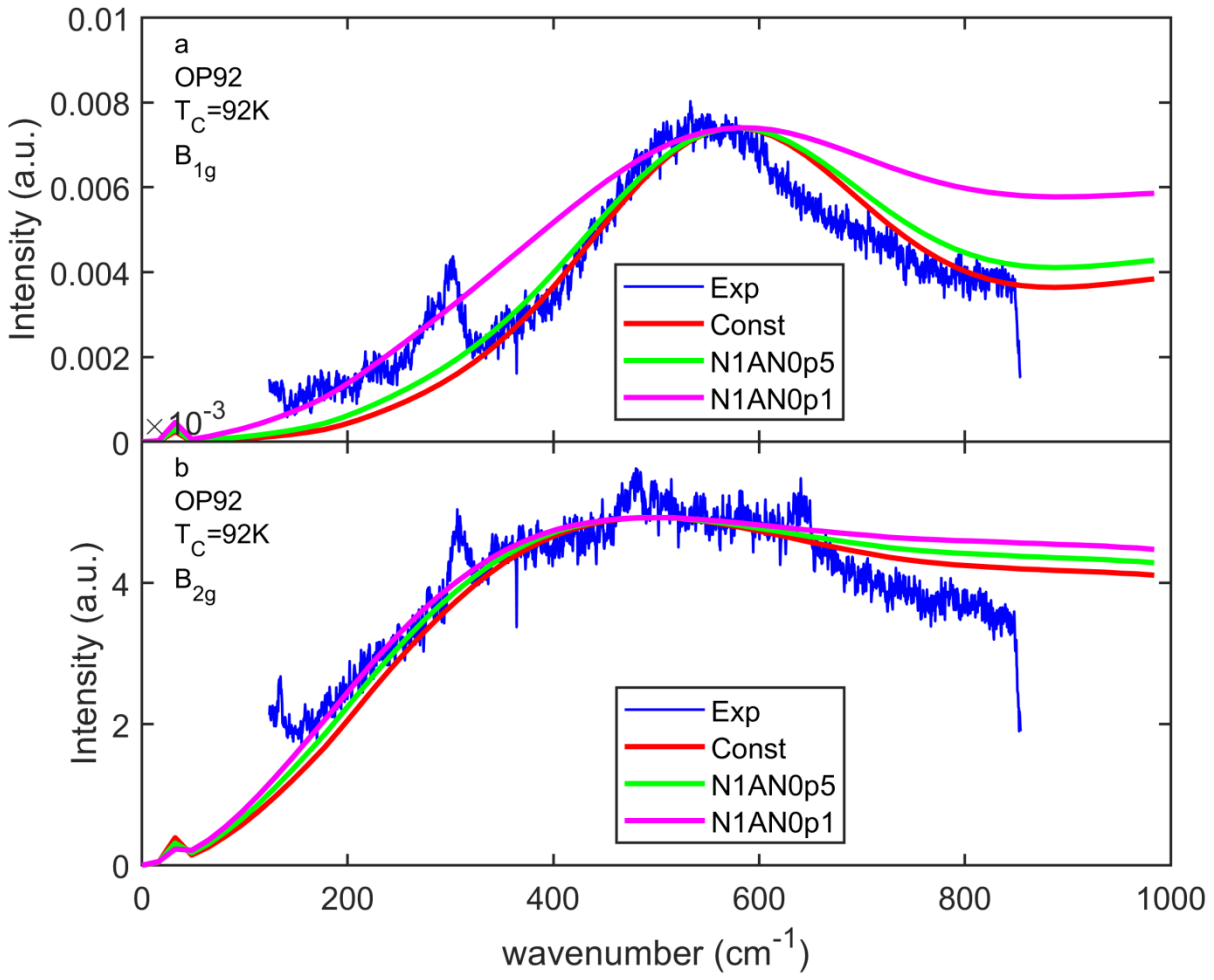

Fig.5.13 Experimental and calculated Raman spectra with different linear intensity profiles for the optimally doped sample in **a** B_{1g} configuration and **b** B_{2g} configuration.

region. In the case x<1 the notation 0px is used which indicates an antinodal intensity of 0.x. In Fig.5.12 (a) the B_{1g} calculated spectra for different linear profiles is shown. Here it can be seen that neither enhancing (magenta curve) nor suppressing (yellow curve) the antinodal region produces significant changes in the calculated spectra, with the only significant difference being the slightly enhanced high frequency intensity when the antinodal region is suppressed. The peak position is robust against modification of the intensity profile and there is no significant improvement in changing it. In Fig.5.12 (b) the B_{2g} calculated spectra for the same linear profiles is shown. Here the modifications are more substantial when the profile is changed. The peak position does not seem to change, while the width of the peak increases when the antinodal region is suppressed (or vice versa decreases when it is enhanced). However this does not seem to produce significant improvement of the calculated spectrum, since, when suppressing the antinode, the low frequency intensity increases, improving the calculated spectra, but so does the high frequency intensity, decreasing the quality of the calculated spectra. Therefore also in B_{2g} configuration there is no significant improvement in changing the profile. Considering that there is no improvement neither in B_{1g} configuration nor in B_{2g} configuration, and that the calculated spectra with linear

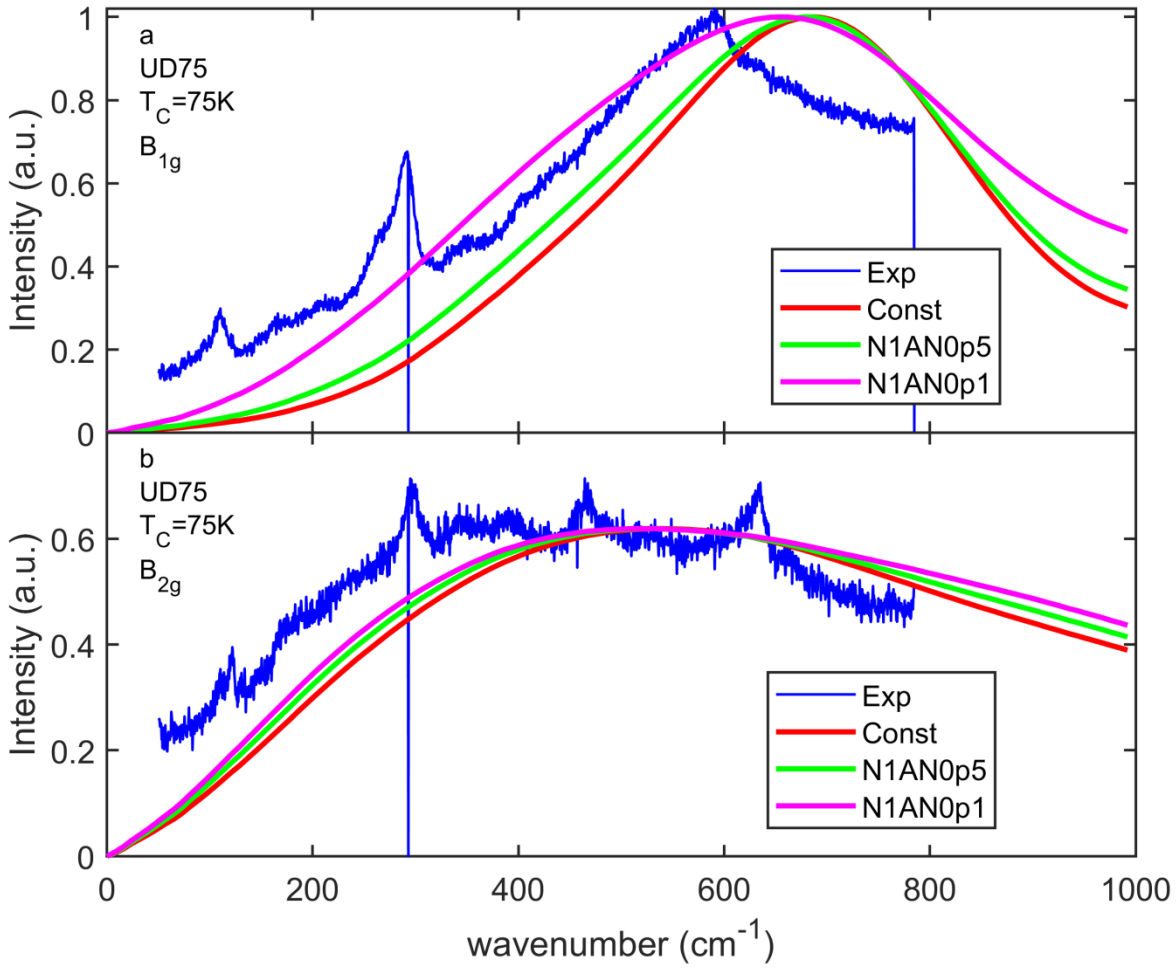

Fig.5.14 Experimental and calculated Raman spectra with different linear intensity profiles for the underdoped sample in **a** B_{1g} configuration and **b** B_{2g} configuration.

profile already reproduces well the experimental one , we can simply consider the constant profile calculated spectra as the best one and as our final pick.

In Fig.5.13 for the optimally doped sample the experimental and calculated with different linear profile spectra are shown. As it can be seen from Fig.5.13 (a) for the B_{1g} configuration, the peak position is again robust against changes of the profile, with only a modification of the broadness of the peak. The suppression of the antinodal region causes the peak to become much broader, and this is accompanied by an overall worsening of the calculated spectra with respect to the experimental one. In B_{2g} configuration in Fig.5.13 (b), the situation is similar to the overdoped B_{2g} configuration case. Again the peak position does not seem to shift and we have a small broadening of the peak with decreasing antinodal spectral weight, accompanied by a small enhancement at lower and higher frequencies. As in the case of the overdoped sample, this is a small improvement for the lower frequencies but a worsening for the higher frequencies, and in total there is no significant improvement by changing the profile in the B_{2g} configuration. Considering both configurations there is no improvement of the calculated spectra by changing the profile we can

pick the constant profile calculated spectra as our best fit also in the case of the optimally doped sample.

For the underdoped sample the calculated spectra with different linear profiles are shown Fig.5.14 together with the experimental Raman peak. In Fig.5.14 (a) the B_{1g} configuration spectra are shown, and here a significant improvement can be seen. By suppressing the antinodal spectral weight the calculated peak position shifts to lower energy, getting closer to the experimental peak position. Additionally the intensity at lower frequency increases, and this is also an improvement of the calculated spectra, since the calculated spectra with constant profile underestimates the intensity at lower frequency. For the B_{2g} configuration in Fig.5.14 (b) the improvement is minute. As in the cases of the other samples the B_{2g} peak broadens, even if only slightly. This is again an improvement in the lower frequencies region and a worsening in the higher frequency region. However in this case of the underdoped sample this is a small improvement since the low frequency region, below the peak, is much larger and more significant than the one at high frequency above the peak. Therefore suppressing the antinodal region constitutes a minor improvement in the calculated B_{2g} configuration spectrum. Altogether we obtain a major improvement in the B_{1g} configuration spectrum and a minor improvement in the B_{2g} configuration spectrum, therefore the antinodal suppressed profile N1AN0p1 can be taken as our pick of the profile that gives the best reproduction of the experimental spectra so far. The N1AN0p1 profile suppresses heavily the antinodal region, giving it an intensity of 0.1 as compared to the nodal region whose intensity is 1.

This profile however, does not decrease the peak energy of the B_{2g} configuration enough to

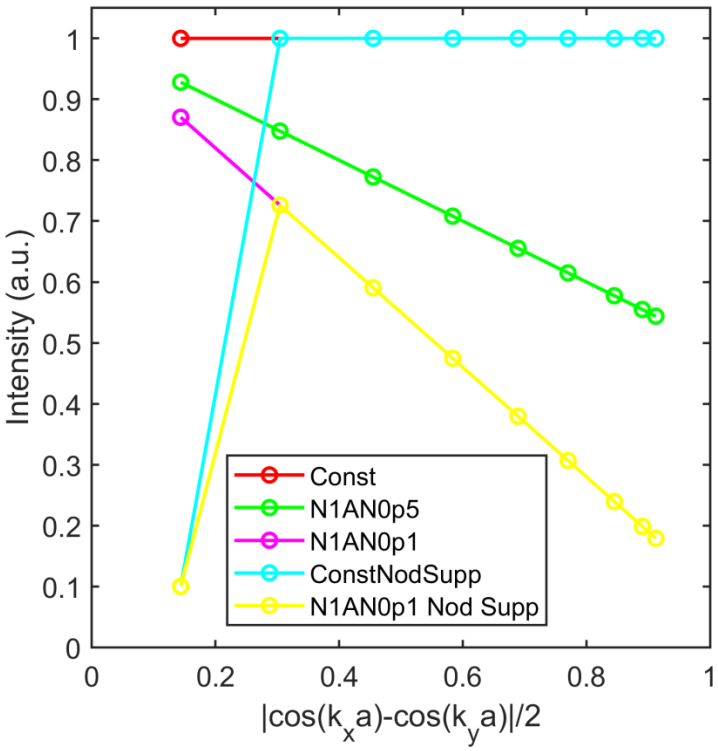

Fig.5.15 Intensity profiles for all of the calculated spectra for the underdoped sample, the cyan and yellow profiles are the ones where the nodal intensity was suppressed.

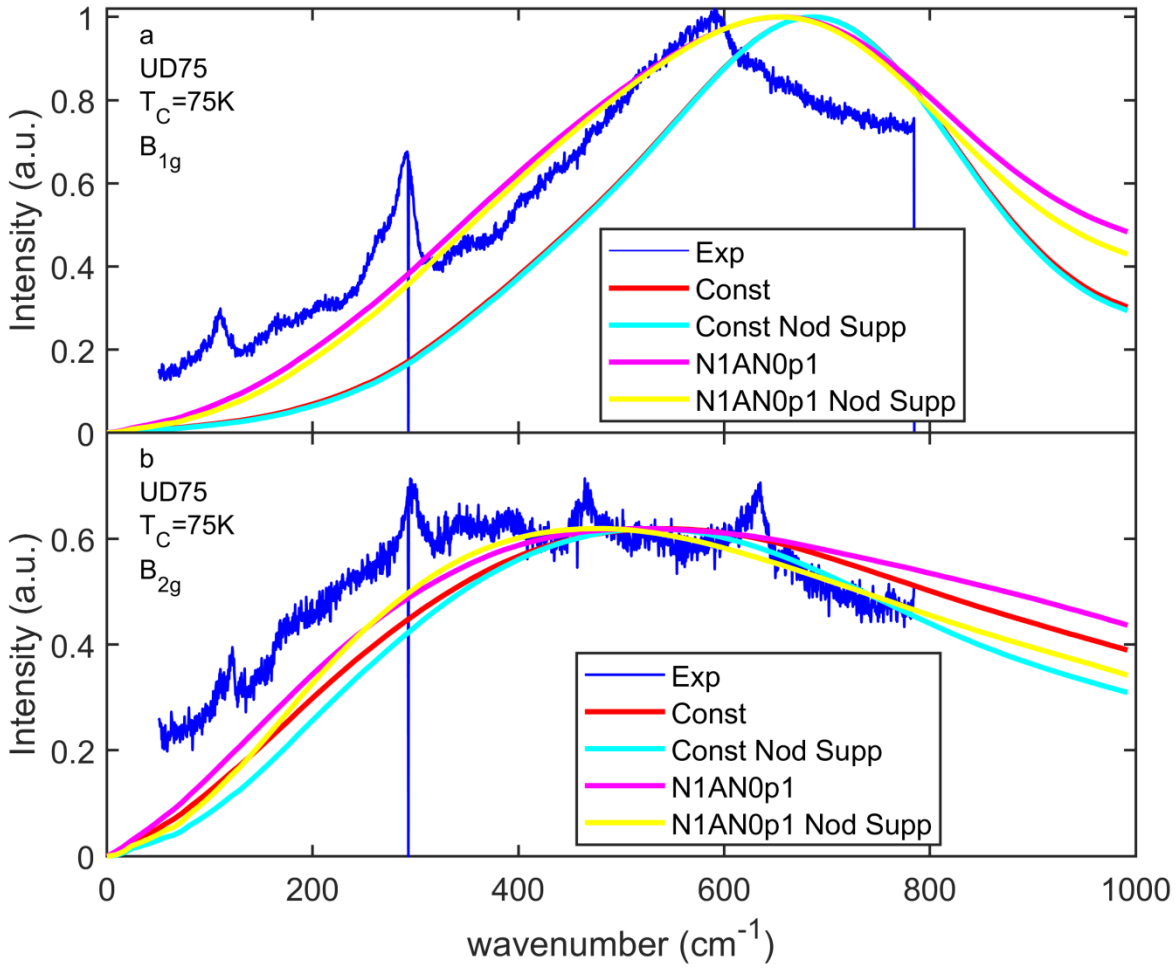

Fig.5.16 Experimental and calculated Raman spectra with different intensity profiles for the underdoped sample in **a** B_{1g} configuration and **b** B_{2g} configuration. Nod. Sup. Stands for nodal suppressed, and these are the profiles shown in Fig.5.15 where the intensity of the most nodal cut was suppressed.

reproduce the experimental observation, since the peak energy of this configuration monotonically increase with lower doping in the three samples. One possibility to try to improve the B_{2g} configuration calculated spectra is, to suppress only the most nodal cut. The reason for this is that the most nodal cut gives a broad spectra which sometimes shows no peak, depending on the intensity profile of the band in the cut, and if the contribution of this cut is overestimated it could hide the peak feature of the B_{2g} configuration in the calculated spectra and prevent us from improving the spectra with a change of the profile. Therefore we calculated the spectra with the suppression of the most nodal cut and with different linear intensity profile for the other cuts. The intensity profiles for all of the calculated spectra for the underdoped sample can be seen in Fig.5.15. The result of the calculation with these nodal suppressed profiles can be seen in Fig.5.16. From this figure we can see that the suppression of the nodal cut does not change neither the B_{1g} nor the B_{2g} calculated spectra drastically if we compare the normal constant profile in the red curve, with the constant profile where only the most nodal cut was suppressed in the cyan curve.

The B_{1g} configuration is not affected since the Raman vertex makes this probe insensible to the nodal cuts. The B_{2g} calculated spectra peak positon does not shift, but the peak becomes sharper, which is a small improvement. If we now apply a decreasing linear profile to the remaining cuts, therefore we use the N1AN0p1 profile, which improved the spectra, for all of the cuts, except for the most nodal one (which we keep suppressed) a great improvement of the spectra can be seen, and this is shown in Fig.5.16 by the yellow curve. The B_{1g} configuration peak shift as the case of the N1AN0p1 profile, since this configuration is not affected by the nodal cut. However, in this case, also the B_{2g} spectra is shifted to lower frequency, and this is a clear improvement, even if the peak position is still overestimated, and the low frequency intensity is still underestimated. The improvement is particularly significant because now the calculated B_{2g} peak energy is lower than the optimally doped one, and therefore we are reproducing the correct doping dependence that was discussed in the previous chapters, and that is shown in Fig5.18. Comparing the nodal suppressed constant profile and the nodal suppressed N1AN0p1 profile (cyan and yellow curve in Fig5.16 and Fig5.15) we can see that the shift to lower frequency of both of the B_{1g} and of the B_{2g} calculated spectra peak is not due to the nodal cut suppression, but to the gradual decrease of the antinodal spectral weight with the N1AN0p1 profile. It is likely that in this dataset an excessive intensity of the nodal cut was hiding the shift of the B_{2g} calculated spectra peak caused by the modification of the profile. Therefore the improvement of the peak and the reproduction of the correct doping dependence are due to the antinodal intensity decreasing profile.

This result is analogous to the previous calculation results that use the kinetic theory[47], [49], [142], [143] in which the antinodal intensity must be suppressed in the underdoped sample to obtain a good reproduction of the B_{2g} peak position and of the B_{1g} peak intensity. Our result is slightly different in the sense that also the B_{1g} peak position is particularly improved by this suppression, but this is most likely due to the different nature of our calculation, that takes as input experimental ARPES data. In these previous works this improvement with decreasing antinodal spectral weight was justified by the competition with the pseudogap, that suppresses superconductivity in the antinode with decreasing doping.[50]–[55] We believe that the present result can be explained in the same manner. In particular if the large antinodal gap in the ARPES data in the underdoped sample is to be attributed mostly to the pseudogap, it makes sense that the calculated Raman spectra using these ARPES data, will have a peak at a higher energy determined by the pseudogap, which will be much larger than the real superconducting energy. Therefore by suppressing the intensity at the antinodal region we are suppressing the contribution from pseudogap dominated states, and enhancing the contribution from lower energy intermediate momentum region states, which have a stronger superconducting character, and we are therefore decreasing the energy of the peak, taking it closer to the experimental value. Considering that in the overdoped and optimally doped samples the effect of the pseudogap is much less than in the underdoped sample, it is reasonable that we can reach a good reproduction of these two higher doping samples Raman spectra with a simple constant profile along the Fermi surface, unlike the pseudogap dominated underdoped sample, where the antinodal spectral weight must be suppressed.

The calculated spectra who give the best reproduction of the experimental Raman spectra are summarized in Fig.5.17, here the constant profile spectra are used for the optimally doped and overdoped samples while the nodal suppressed N1AN0p1 profile is used for the underdoped

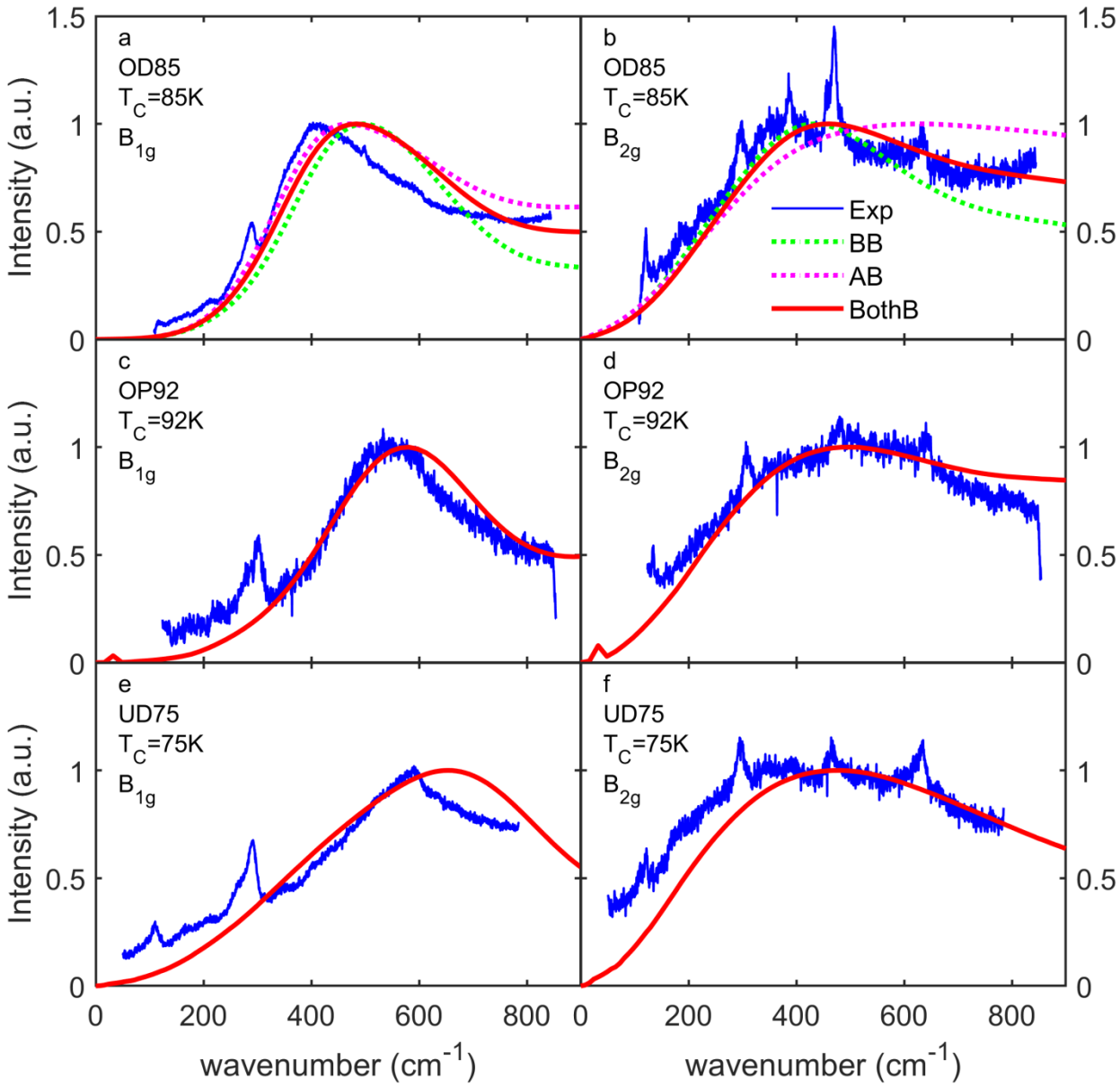

Fig.5.17 Experimental Bi2212 spectra together with the calculated spectra using the Kubo formula and assuming constant profile along the Fermi surface, for the overdoped sample in **a** B_{1g} and **b** B_{2g} configuration and for the optimally doped sample in **c** B_{1g} and **d** B_{2g} configuration. Experimental Bi2212 spectra together with the calculated spectra assuming decreasing intensity profile towards the antinode but with the nodal cut supressed (nodal suppressed N1AN0p1) for the underdoped sample in **e** B_{1g} and **f** B_{2g} configuration. In the overdoped sample panels **a** and **b** both the AB and BB bands calculated contributions are shown by magenta and green dashed lines respectively. Here the red solid line represents the total contribution of both bands summed up with normalized intensity and band ratio equal to one.

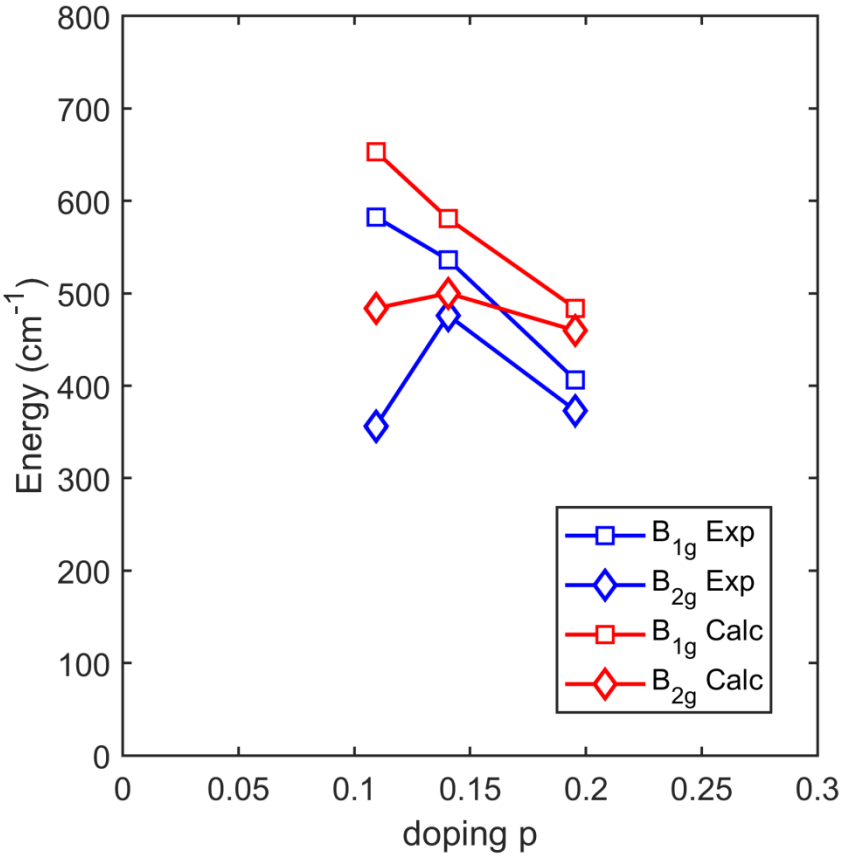

Fig.5.18 Experimental Bi2212 peak positions together with the calculated spectra preak positions using the Kubo formula

sample. Here it can be seen how we were able to reach a good reproduction of all the experimental Raman spectra, with the exception of the underdoped sample, which is not optimally reproduced, but has been improved by our choice of intensity profile suppressing the antinodal region.

In Fig5.18 the calculated and experimental Bi2212 preak positions are summarized. As it can be seen here, the calculated peak positions in all samples and in all of the configurations are higher than the experimental ones. One possible reason for this overestimation is that the effect of the pseudogap is different in ARPES and Raman. The pseudogap dominates the antinodal region in ARPES, but is only weekely observed in Raman as a small suppression of spectral weight. If Raman is not so sensitive to the pseudogap but ARPES is, it is reasonable that the calculated spectra starting from ARPES data overestimates the gap size and therefore the peak position. The different doping dependence in the underdoped side of the B_{1g} and the B_{2g} peak position, namely the two energy scale, was correctly reproduce by our calculation, even if it is not as evident as the experimental one. In particular the B_{2g} doping dependence was reproduced starting from ARPES data where the nodal gap slope is constant, using an appropriate intensity profile that suppressed the antinodal region. This shows how the decreasing B_{2g} peak energy in the underdoped side can be explained, without considering a decreasing gap value, but considering a decreasing antinodal spectral weight caused by the competition of the pseudogap with superconductivity.

5.2: Bi2223 Analysis

5.2.1: Calculation Input preparation

The Bi2223 Kubo calculation has been performed in a similar manner to the Bi2212 Kubo calculation. The ARPES experiment was performed by S.Ideta (National Institute for Molecular Science) on a slightly underdoped, but almost optimally doped sample (T_C=108K) grown by Uchida Group in Tokyo University. The details of the experiment were reported in section 3.4, and will not be repeated here. The only parameter that will be repeated is the photon energy *hv*=8eV. This parameter is of high interest here, since, as discussed previously, the ARPES sensitivity to a certain band can change dramatically when the photon energy is changed, due to the modification of the matrix element. It was shown in Ref.[123] that the relative intensity of the IP and OP strongly varies with the incident photon energy.With the photon energy used here, the IP band is suppressed with respect to the OP band. This can be seen clearly in Fig.5.19, where all of the ARPES cuts are shown, zooming on the two bands. The IP band is extremely weak in the nodal region in the present dataset. By moving away from the node the band becomes gradually more intense in the intermediate momentum region, but it starts disappearing again towards the antinode and is observed only until cut 13 in which it is extremely weak (panel C13 in Fig 5.19). After the cut 13 the IP band is undistinguishable from the high energy incoherent intensity. On the other hand the OP band remains intense in all the present ARPES cuts. The fact that the IP band is extremely weak in the nodal and antinodal region in the present dataset poses a challenge to the calculation, since these 2 momentum regions are the most important for calculating the B_{2g} and B_{1g} configuration respectively due to the momentum dependence of the Raman vertex of these 2 configurations shown in equations (3.16) and (3.15). However, since in this dataset both the IP and OP bands are observed, we attempt to use it to calculate the contribution to the Raman spectra of each of these 2 bands, as it was done for the overdoped sample.

There is a certain amount of interaction between the 2 bands in the intermediate and antinodal region as it can be seen in Fig 5.19. It is not clear if this intensity should contribute to the Raman spectra, therefore we tried to avoid this contribution in the calculation for the IP band by removing it through the EDC fit.

As in the case of Bi2212 calculation the k_F positions have been extracted by inspection of the MDCs. Unlike in the case of Bi2212, this operation could be done also in the most antinodal cuts, since also in these cuts the band is dispersive enough, and not completely flat. This may be due to the fact that these cuts are in fact not so close to the border of the Brillouin zone as the ones of Bi2212, and this can be seen in Fig.5.20. The mapping was done by ensuring that the position of the band along the nodal line was consistent with the previous reports,[123] and the result of this mapping can be seen in Fig.5.20. The fact that the measured ARPES cuts do not reach the antinode may also be a limitation when using these data for the calculation, since this region may be quite necessary for a better reproduction of the B_{1g} configuration. However the underdoped IP band peak disappears even more far from the antinode, so the IP calculated contribution should be

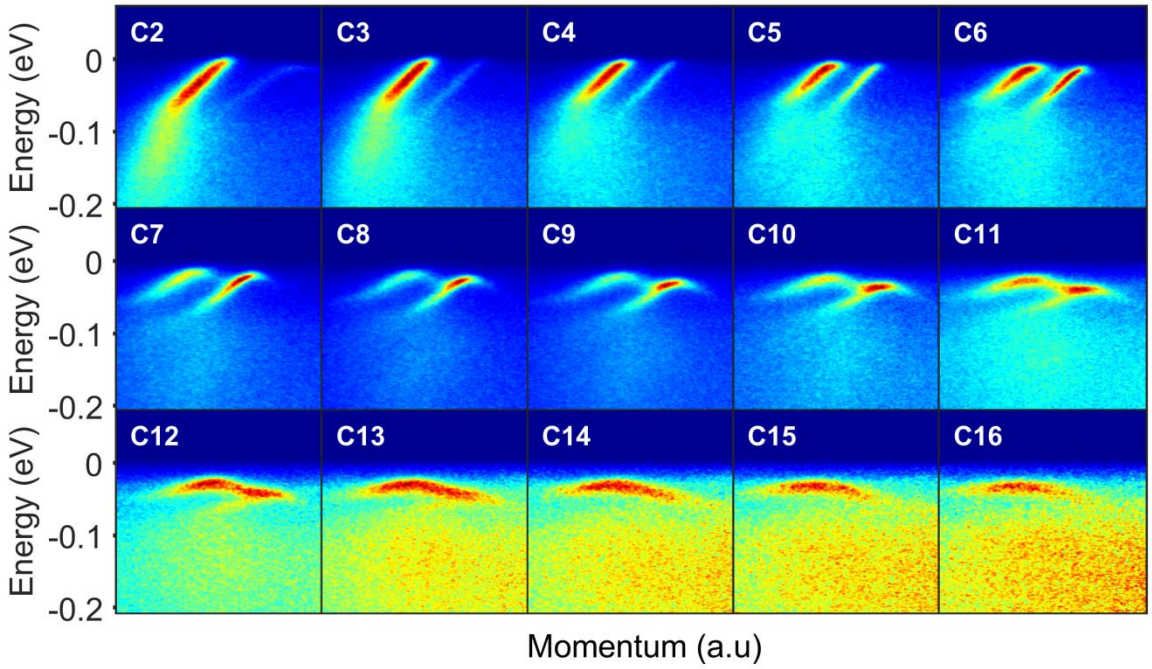

Fig.5.19 ARPES cuts for the slightly underdoped (but almost optimally doped) Bi2223 sample, going from the node in C2 to the most antinodal cut in C16

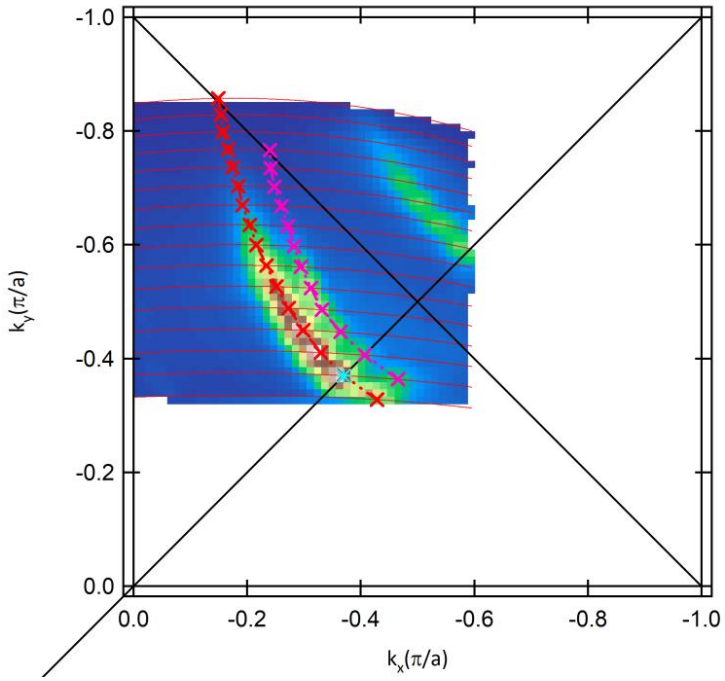

Fig.5.20 ARPES data mapping for the slightly underdoped (but almost optimally doped) Bi2223 sample The extracted Fermi vectors are represented by the purple crosses for the inner plane band, and by red crosses for the outer plane band. A ghost image of one of the bands is also observed closer to the (π,π) point of the momentum space.

unaffected by this limitation. The same is not true unfortunately for the OP band, therefore the peak position in the B_{1g} configuration may be slightly changed.

The tight binding fit was performed in this case using two separate tight binding equations, one for each band, unlike the Bi2212 overdoped sample case where a bilayer splitting term was used. The doping imbalance between the IP and OP layer gives a large band splitting, therefore in the Bi2223 case we can simply fit the two bands separately using the equation (5.1). The tight binding parameters are summarized in Table 5.2, and are found to be roughly consistent with the previous reports.[123] The ratio of the nearest and the next nearest neighbour hopping parameter t'/t is found to be increasing from the OP to the IP band which is the expected behaviour. From Fig.5.21 and Fig.5.22 the good quality of the fit can be assessed. In Fig.5.21 the experimental k_F together with the Fermi surface calculated from the tight binding fitting are shown for both the OP and IP bands. Here it can be seen how the calculated Fermi surface follows well the experimental k_F for both bands. In Fig.5.22 the fitted tight binding function along the ARPES cuts, together with the experimental k_F are shown. Also from this figure we can see how the fitted function follows well the k_F positions, but we can also see how the tight binding fails to describe well the experimental bands. This is analogous to the Bi2212 case, where again the tight binding fails to describe the anomalies of the bands, such as the kinks and the flat band dispersion. However, as we previously discussed for the Bi2212 case, since we have only a limited use for the tight binding function in our calculation, that is to give a first approximation of the gap opening along the ARPES cuts, we proceed with the calculation with confidence that the tight binding result is sufficient as a first approximation, despite its limitations.

Since, as said previously, all of the Fermi vector positions could be experimentally determined from the MDCs, also the most antinodal ones, in the Bi2223 case there was no need to use the tight binding fit to determine these antinodal k_F. The tight binding is only used to determine the size of the superconducting gap along the ARPES cuts, and is inserted in the Kubo equation (5.3), and plays a role in the calculation only for the small interval of momenta where $\Delta_{\boldsymbol{k}} \neq 0$.

The raw ARPES intensity was treated in a similar manner to the Bi2212 case. Firstly we removed the Shirley background in the iterative manner previously described, and assuming that the intensity at the highest binding energy was composed only by background. An example of Shirley background subtraction for an EDC of Bi2223 can be seen in Fig.5.23. After the background

	t (eV)	t'/t	t''	μ (eV)
OP	0.734	0.251	t'/2	-0.773
IP	0.633	0.275	t'/2	-0.386

Table 5.2 Summary of all the resulting fit parameters for the 2 bands of the Bi2223 sample. t'' is fixed to be half of t'.

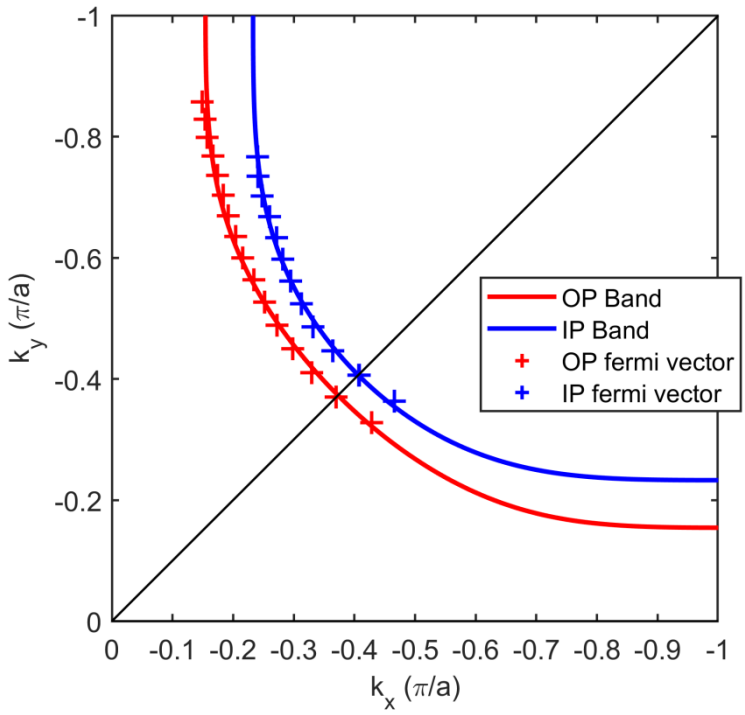

Fig.5.21 Resulting tight binding fit Fermi surface together with the experimentally obtained Fermi vectors for both the inner and outer plane bands.

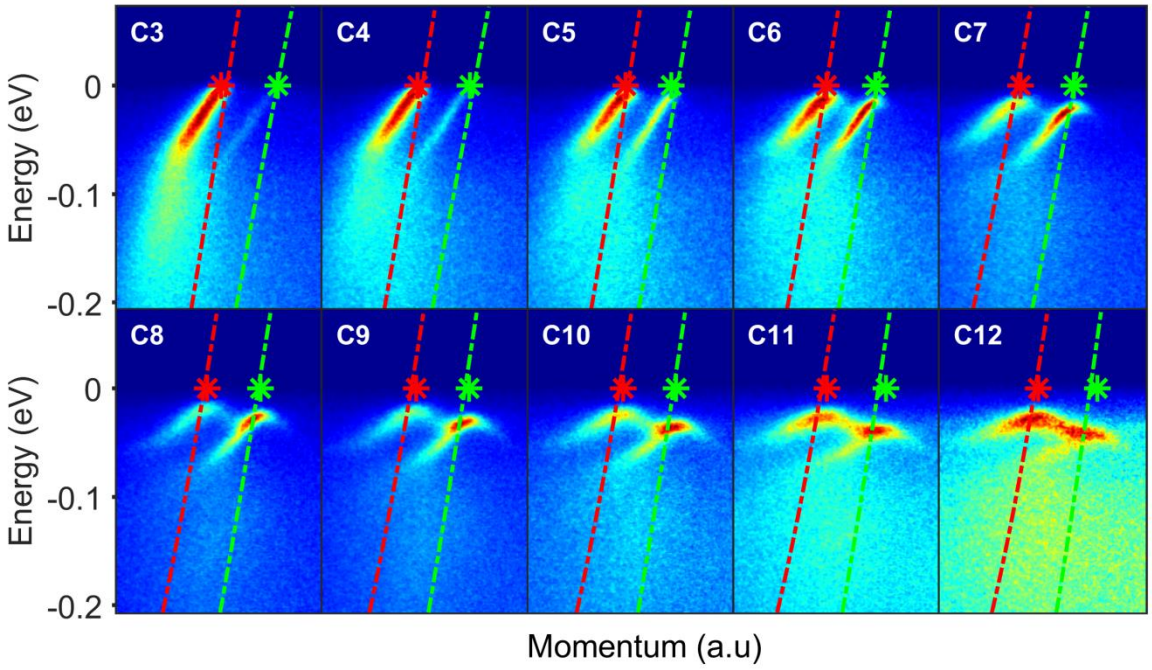

Fig.5.22 Tight binding fit results along the ARPES cuts for both the inner and outer plane band (green and red dashed lines respectively) going from the node in C3 to the most antinodal cut in C12, together with the experimental k_F (green and red stars for the IP and OP respectively)

subtraction, the inner and outer plane bands must be separated. This was done in a similar manner to the overdoped Bi2212 sample, by fitting the EDCs with 3 different Gaussian peaks after the background subtraction. This procedure is clearly shown in Fig.5.23. Also in this case 2 Gaussian peaks are used to fit the IP and OP bands (one for each), and an additional peak is used for the high energy incoherent intensity.

The EDC fit had to be done in multiple steps. Firstly the fit was done with fully free parameter, which gives good results only in the momenta where both bands are strong. This is not the case for the nodal and antinodal regions where the IP band is extremely weak, and for case of the antinodal region is also mixed with other strong contribution, such as the high energy incoherent intensity and the back-bending of the OP band. Since the IP band was so weak in the nodal region (see cut C3 and C4 in Fig.5.19) it had to be fitted on its whole length, also for the momenta where the OP band was not observed, otherwise the calculated Raman spectra would have been submerged by noise. In this step the peak position was fixed and the width was calculated with an appropriate relationship with the binding energy (peak position), therefore the only free parameter was the intensity. This fit with less free parameters was also done for the intermediate and antinodal cuts at the momenta where the free parameter fit was not successful. For the last 3 antinodal cuts before the IP band disappears, where the band was extremely weak, and mixed with other contribution, this had to be taken a step further, by assuming also an appropriate intensity profile along the band, and leaving therefore only a multiplication constant for the whole band as free parameter. Since the IP band was so weak on the whole Fermi surface, we opted to calculate the Raman contribution only from the fitted IP band function for the whole Fermi surface. This had to be done to avoid the strong contribution that noise has on a low intensity band in the

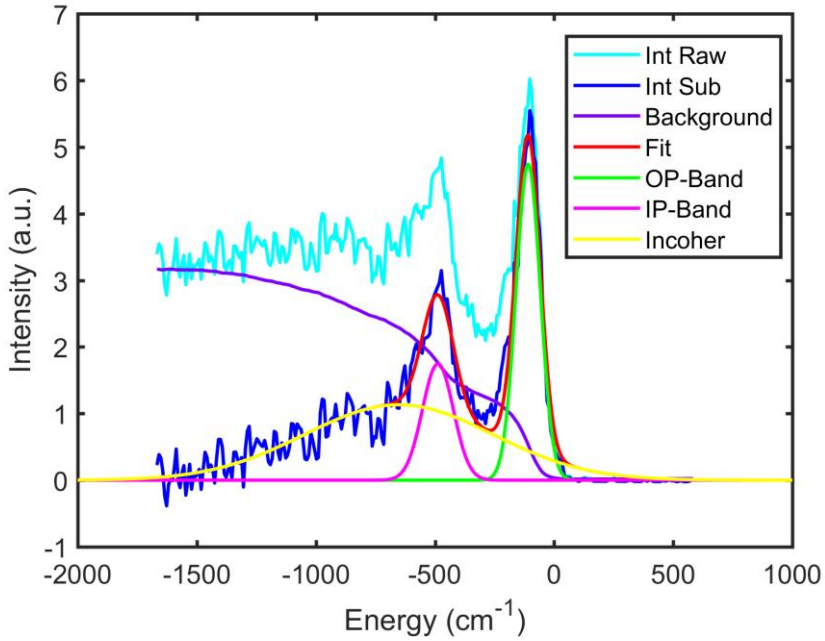

Fig.5.23 Example of treatment of the raw ARPES EDCs, the Shirley background is subtracted from the raw spectra, which is subsequently fitted with 3 Gaussian peaks, one for each band and one for the high energy incoherent intensity.

Raman calculation with the Kubo formula.

The result of our EDC fitting and the input of our calculation can be seen in Fig.5.24. In the upper row, the intensity used as an input for the outer plane calculation is shown. Since this calculation is done until the OP k_F and not past this momentum point, it is not necessary to subtract properly the IP intensity past this point and an intermediate fit result, which subtracts appropriately the IP intensity before the OP k_F could be used. For this reason the residual IP intensity seen in the figure is not a reason of concern. In the lower row of Fig.5.24 the input intensity for the IP can be seen. Here, as said before, we take as input only the fitted IP intensity to avoid contributions from the background intensity. From this figure we can see that, even if the fit result is kind of crude, we were able to successfully separate the OP and IP intensity, and we could therefore proceed to calculate their contribution to the Raman spectra separately.

The ARPES cuts intensity was again normalized by the maximum intensity value at the Fermi momentum k_F for each cut, and both the inner and outer plane cuts where normalized to the same value. Therefore this calculation will consider constant intensity profile along the Fermi surface, as the initial Bi2212 calculation, and considering the same intensity for the inner and outer plane bands. Since there is a strong dependence of the relative intensity of the two bands on the ARPES photon energy, it is difficult to predict what should be the real relative intensity of the bands (of the spectral function) after the elimination of the matrix element effect. Therefore considering it equal may be a rough approximation. One quick consideration is that there is a

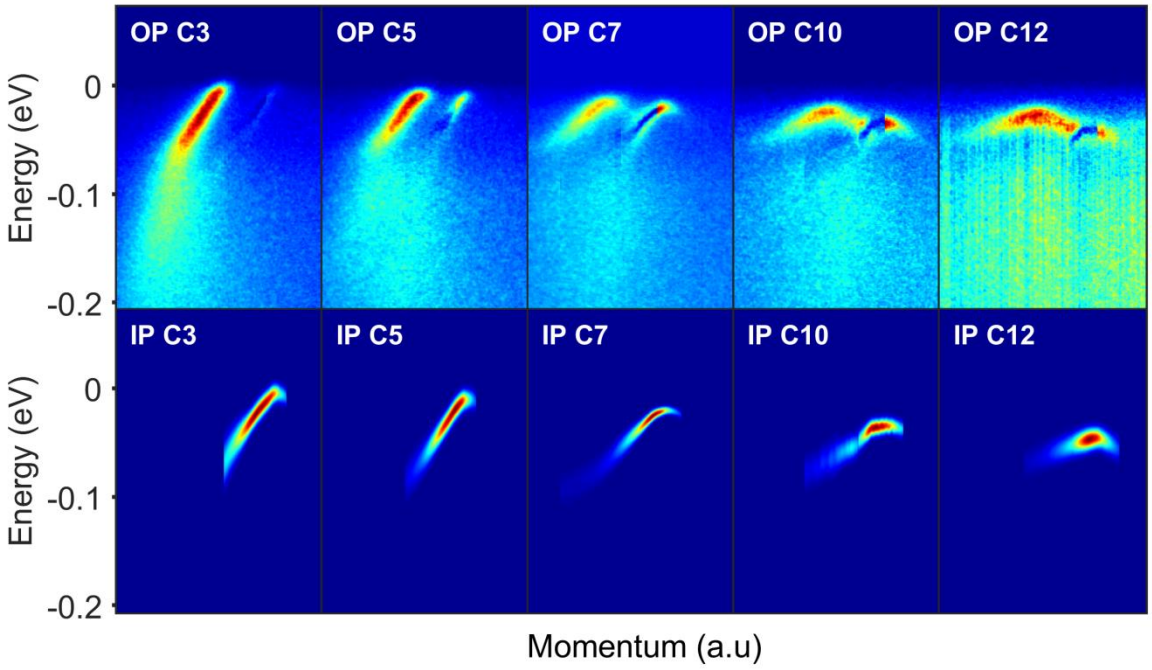

Fig.5.24 Results of the EDC fitting and input intensity for the Kubo calculation for the outer plane (upper row) and for the inner plane (lower row). For the outer plane the total cut intensity after the subtraction of the fitted IP intensity was used as an input for the calculation. For the IP calculation only the IP fitted intensity was used.

double number of OP than the number of IP in a unit cell, therefore the OP intensity might be larger.

The calculated intensity of Fig.5.24 was symmetrized and the calculation was performed on an appropriate momentum range. For the OP band this range is constituted by the momentum interval between the point of the cut on the (0,0)-(π, π) line and the OP Fermi vector. For the IP this was done from the momentum where the fit of Fig.5.24 begins to the IP k_F.

5.2.2: Calculation Results and Discussion

The result of the Bi2223 Kubo calculation using this separated IP and OP intensity is shown in Fig.5.25. In Fig.5.25 (a) the calculated B_{1g} contribution can be seen. The first observation from this panel is that the OP and IP calculated Raman spectra shown with red and green lines respectively, give a peak at a significantly different energy position. Additionally the energy positions of these calculated IP and OP Raman peaks are close to those of the two experimental pair breaking peaks that were found in this study and discussed in section 4.2. The calculated peak positions together with the experimental peak positions are summarized in Table 5.3. As it can be seen, these values are close, with a difference of only 65 cm^{-1} for the OP and 23 cm^{-1} for the IP. In both cases the calculated peak position is slightly lower than the experimental one. This result is a strong evidence that our peak assignment was correct and more importantly it constitutes a strong proof that the origin of the experimental double pair breaking peak is indeed the double superconducting gap of Bi2223 which originates from the two chemically inequivalent inner and outer Cu-O_2 layers.

By summing up the calculated B_{1g} IP and OP contribution with a band ratio of 1.7 (enhancing the IP contribution) we can obtain the magenta line in Fig.5.25 (a) which is a good fit of the low temperature experimental B_{1g} Raman spectrum. Unlike the case of the overdoped Bi2212 sample, here we had to use a band ratio greater than one, enhancing the IP band contribution, to obtain a good fit. This will be discussed more in detail later on. This obtained total calculated spectrum reproduces well the shape of the experimental B_{1g} Raman spectrum, with only a small overestimation of the intensity between 250 cm^{-1} and 500 cm^{-1} which originates from the small underestimation of the OP peak positon. One possible reason for this underestimation is that the

B_{1g} peak	Exp cm^{-1}	Calc cm^{-1}
OP	565	500
IP	805	782

Table 5.3 comparison between the calculated and experimental peak energies in cm^{-1}. A good correspondence between the two is found.

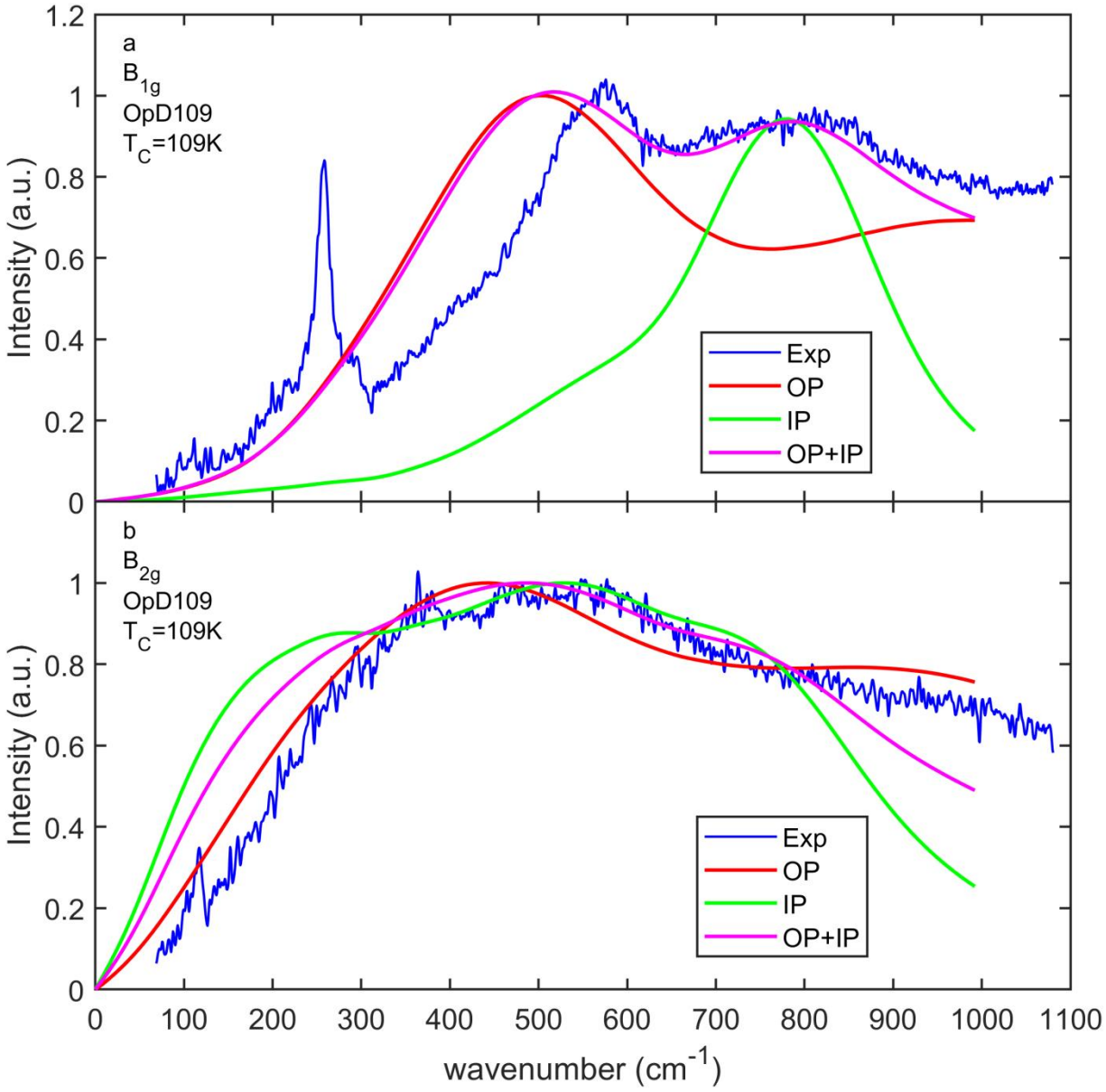

Fig.5.25 Experimental and calculated Raman spectra for the optimally doped Bi2223 sample in **a** B_{1g} configuration and **b** B_{2g} configuration. The red and green curves are respectively the OP and IP calculated contribution to the Raman spectra. The magenta curve is the summation of the OP and IP peak contribution with a band ratio of 1.7 enhancing the inner plane band intensity.

starting ARPES data does not reach the antinodal region as discussed before and as shown in the mapping in Fig.5.20. The fact that we are missing out the contribution from these most antinodal cuts may reduce the total calculated peak position with respect to the experimental one and generate this discrepancy. On the other hand the IP peak is well reproduced by the calculated contribution, in both of the peak position and the overall shape. This may signify that even if some residual of the IP band remains, at more antinodal cuts than the one where the ARPES intensity of the IP band disappears in our dataset, this does not contribute significantly to the Raman spectrum.

In Fig.5.25 (b) the B_{2g} calculated contribution for the two bands is shown together with the experimental B_{2g} low temperature Raman spectrum. Here we can see that even if the IP calculated spectrum is quite strange, the IP and OP calculated peaks have an overall similar shape, which is similar in both cases to the experimental spectrum. Both of these two bands calculated spectra seem to reproduce quite well the broad peak and the shape of the experimental spectrum. Here the IP calculated contribution shows a peculiar shape with three humps. This behaviour is most likely not intrinsic, and it is probably due to limitations of the ARPES data and of our fit. As discussed earlier the nodal IP band is extremely weak, and in the most nodal cut the band intensity is just above the noise intensity. It follows that even a good fit of such a low intensity band cannot be of high quality, and modifications in the band profile may occur. Unfortunately the most antinodal cut is the one that, due to the Raman vertex, contribute the most to the B_{2g} calculated contribution. For these reasons the quality of the fit is not so high, and this is reflected in the unrealistic humps of the IP B_{2g} calculated contribution. Nevertheless this calculated spectra overall shape is not so far from the experimental B_{2g} Raman spectrum, and not so different from the OP calculated spectrum, which does not share the IP problem of low intensity. Therefore we believe that even with these limitations the IP B_{2g} calculated contribution is not completely unrealistic. The OP B_{2g} peak overall shape is quite good, with a peak that only slightly underestimates the experimental peak positons, and is only slightly too sharp. Summing up the calculated contribution from the two bands, with the same band ratio that was used for the B_{1g} calculated spectrum (band ratio of 1.7), we obtain the total B_{2g} calculated spectrum, shown with the magenta line in Fig.5.25 (b). This total calculated spectrum also reproduces quite well the shape of the experimental peak, with a good reproduction of the peak position and of the peak broadness.

Altogether we were able to reach a good reproduction of the experimental Raman spectra both in B_{1g} and B_{2g} configurations, using the Kubo formula with ARPES data as input, and calculating the separated contribution of the two bands. We believe that the fact that we were able to reproduce the double peak structure separately with the OP and IP ARPES intensities constitutes a strong proof that the origin of this double peak structure is to be attributed to the double superconducting gap of Bi2223 and to the two inequivalent kind of copper oxygen layers.

As stated before the present result was obtained with an enhancement of the IP band intensity with respect to the OP one, more specifically a band ratio of 1.7. The IP and OP ARPES cuts have been normalized, in the manner described previously, and following this normalization the IP band had to be enhanced by a factor of 1.7. The reason we had to give this enhancement to the IP intensity can be seen in Fig.5.26 (a). Here the summated Raman contribution with many different band ratios is shown for B_{1g} in Fig.5.26 (a) and for B_{2g} in Fig.5.26 (b). It is evident that the summation with band ratio equal to one, which is same intensity along the Fermi surface for both bands, shown in Fig.5.26 (a) by the yellow curve, is dominated by the OP contribution and the IP peak is only slightly visible. To obtain the correct relative intensity of the B_{1g} peaks the IP ARPES intensity must be enhanced up to a band ratio of 1.75, which is shown by the green dashed curve, and which gives the best fit of the experimental spectra. For the B_{2g} configuration in Fig.5.26 (b) we see how the band ratio does not play a big role in the overall shape of the calculated peak. This is due to the fact that the OP and IP calculated contributions are not so different between each

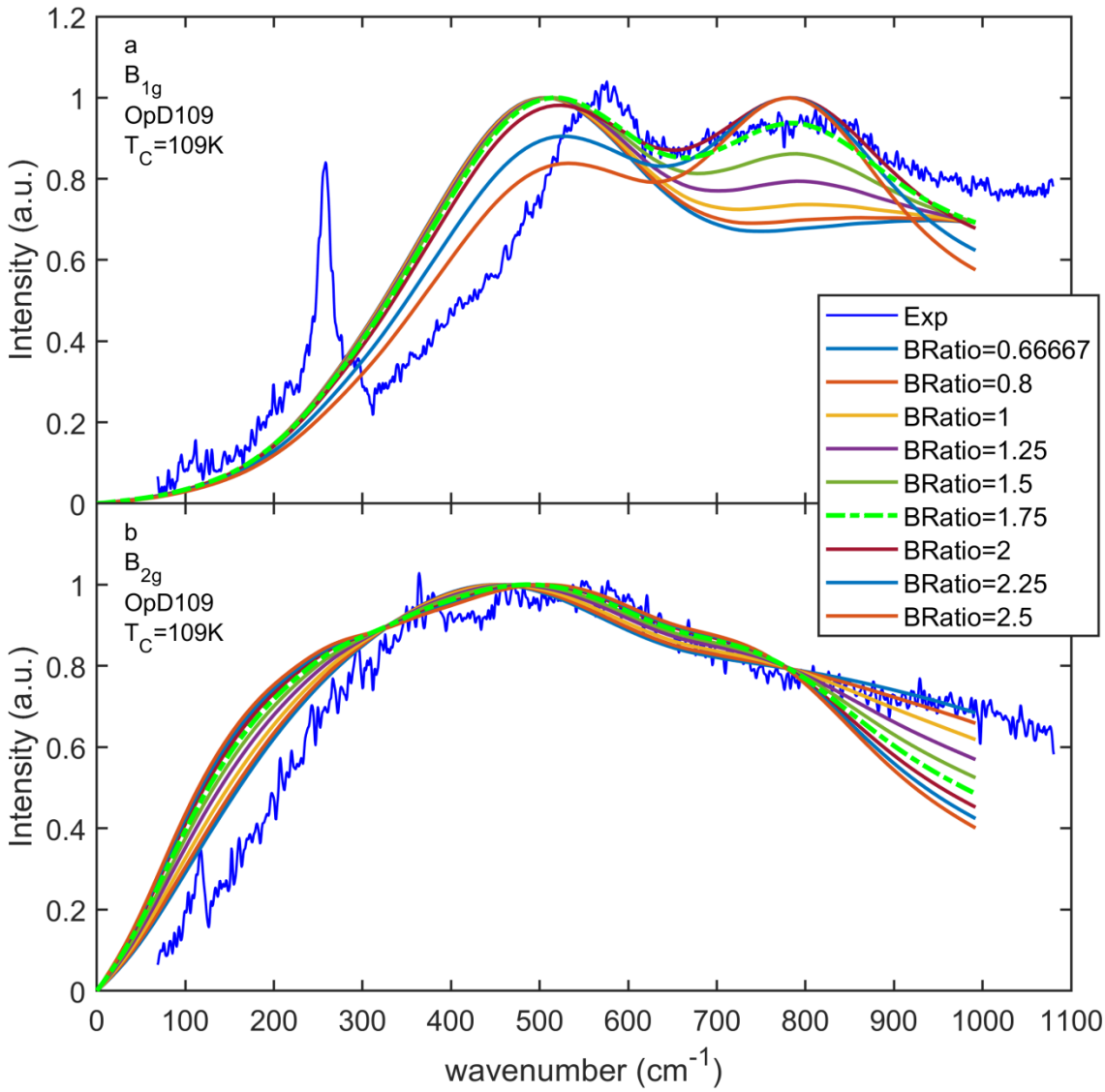

Fig.5.26 Experimental and calculated Raman spectra with different band ratios for the optimally doped Bi2223 sample in **a** B_{1g} configuration and **b** B_{2g} configuration. The green dashed curve is the summation of the OP and IP peak contribution with a band ratio of 1.7, enhancing the inner plane band intensity, which gives the best fit reproducing correctly the relative intensity of the Raman peaks.

other, and therefore the band ratio does not change much the total spectra. Since this parameter does not influence so much the B_{2g} configuration spectrum but gives a clear improvement of the B_{1g} configuration spectrum for a band ratio of 1.75, this value was taken as the final one for the best fit.

We have to note however that it is unlikely that this value of the band ratio represent the real relative intensity of the band, but that it is probably better to view this parameter as mere fitting parameter with little physical meaning. There are multiple reasons for this. Firstly there is the consideration that the double number of OP layer per unit cell may signify that the OP intensity

should be intrinsically stronger. Then, the ARPES photon energy must be considered and in this case it is supposed to furtherly enhance the OP band intensity. However in this calculation the ARPES intensity of the two bands was normalized to the same value, therefore it seems strange, given the previous considerations that we need to furtherly enhance the IP band with a band ratio of 1.75, and this value may be unrealistic. One possible source of this anomaly may be that since the IP band was so weak in the nodal and antinodal region we had to assume several parameters including the width and, in the antinodal region, the intensity profile. Since the Kubo calculation is a convolution of the peaks of the symmetrized EDCs with themselves, not only the intensity profile of the band, but also the width of the EDC may strongly influence the intensity. Overall too many factors may influence this parameter, and therefore it is better to view it as a mere fit parameter with little physical meaning. An additional reason that may cause us to have given an excessive weight to the IP may in fact come from the OP calculated spectrum. The B_{1g} calculated spectrum shows a dip structure above its peak at approximately the same frequency of the IP peak. If this dip structure was overestimated in the OP spectrum, this may happen for example with an excessive background subtraction, the needed IP peak intensity to correctly reproduce the experimental B_{1g} spectrum would increase.

In this calculation we were able to obtain a good fit of the experimental Raman spectra using a linear intensity profile along the Fermi surface, but there are multiple reasons to consider a different profile. Firstly the real intensity profile (or quasiparticle spectral weight) may change with the momentum, or the ARPES intensity may be influenced by the matrix element. Additionally if we consider the result on Bi2212 discussed in the previous section, in which we were able to improve on the spectrum calculated for the underdoped sample by using a profile suppressing the antinodal region, it is certainly better to try different profiles also in the Bi2223 case for completeness. This has been done in Fig.5.27 and Fig.5.28 for the outer and inner plane calculated contribution respectively. Here the same notation used in the previous section is adopted, where the name of the profile indicates the intensity value in the node and in the antinode.

In Fig.5.27 (a) the OP calculated contribution with different linear profiles for the B_{1g} configuration is shown. Here it is obvious that the spectrum is extremely robust against modifications of the intensity profile, since the spectrum is almost unchanged. The only modification may be a minute shift of the peak at higher energy, accompanied by a minute sharpening of the peak, with increasing antinodal weight. However these modifications are so small that they can be considered irrelevant. This may be due to the strong similarities between the cuts in the antinodal region for the OP band, that collectively give extremely similar contributions, and make this spectral shape robust. In Fig.5.27 (b) the OP calculated contribution with different linear profiles for the B_{2g} configuration is shown is also shown. Here the effect of enhancing the antinodal region is to make the peak shaper, while suppressing it has the opposite effect, and the peak position does not seem to shift by a significant amount. However since the constant profile calculated OP contribution has an appropriately broad peak, that reproduces quite well the experimental shape, it seems that there is no improvement in the fit by neither suppressing nor enhancing the antinodal spectral weight. The N1AN2 spectra (that doubles the antinodal weight) gives a small improvement in the lower frequencies, however the sharpening of the peak is not an

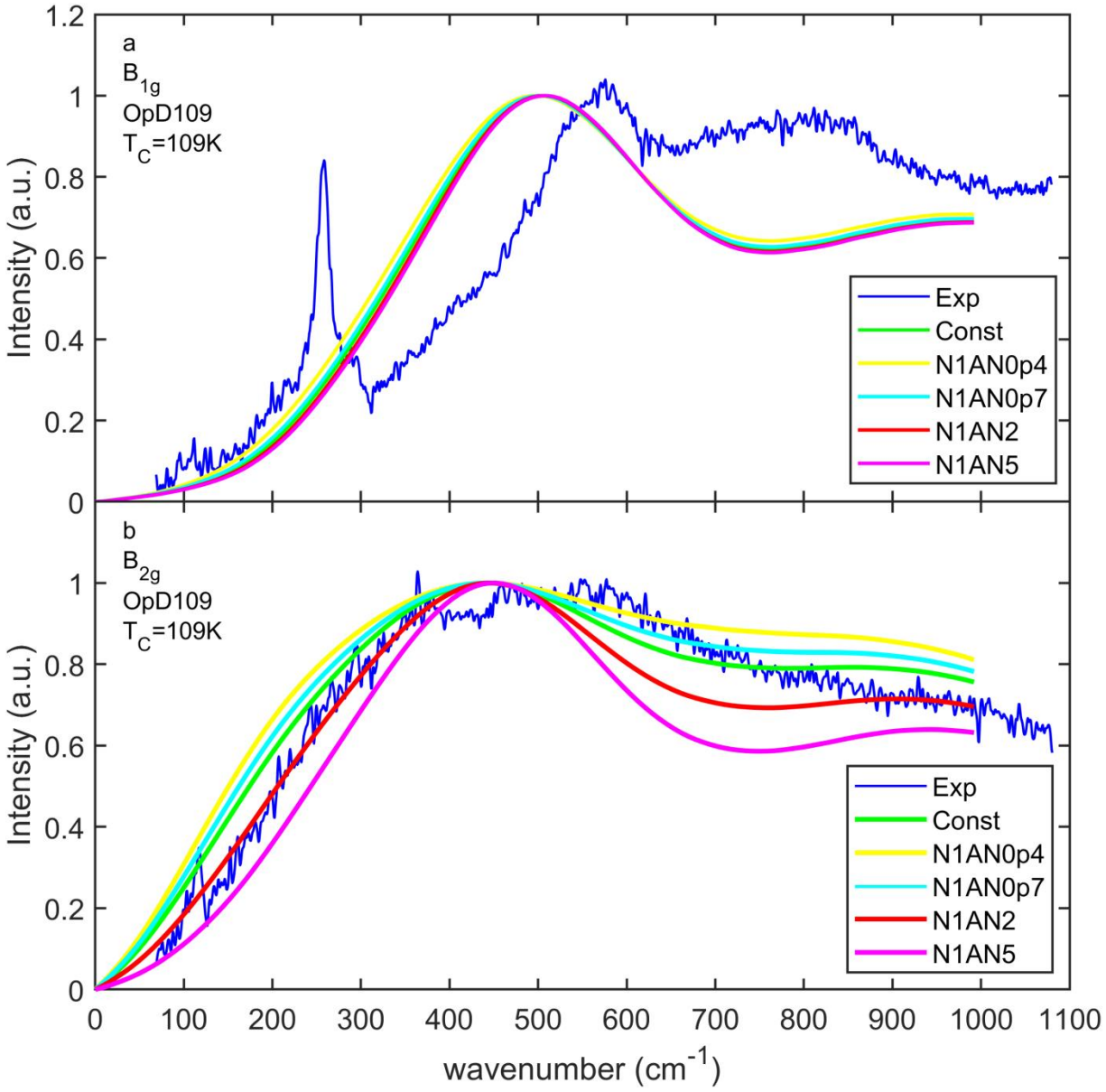

Fig.5.27 Experimental Raman spectra and calculated OP contribution to the Raman spectra with different linear profiles for the optimally doped Bi2223 sample in **a** B_{1g} configuration and **b** B_{2g} configuration.

improvement since the experimental spectra is broader, and also causes an underestimation of the intensity at the higher frequencies. Overall it seems that no improvement is obtained by changing the intensity profile and a since the result seems to be worsening in the B_{2g} configuration, we believe that the best reproduction of the peak was already reached with the constant profile calculated spectra and we therefore pick it as our best result for the OP contribution calculation.

The same procedure of calculating the Raman spectra with different linear profiles is repeated for the IP in Fig.5.28. The calculations with different profiles for the B_{1g} configuration are shown in Fig.5.28 (a), and as in the case of the OP calculation the peak positon is found to be very robust against changes of the intensity profile. The tail of the peak at high frequency is suppressed

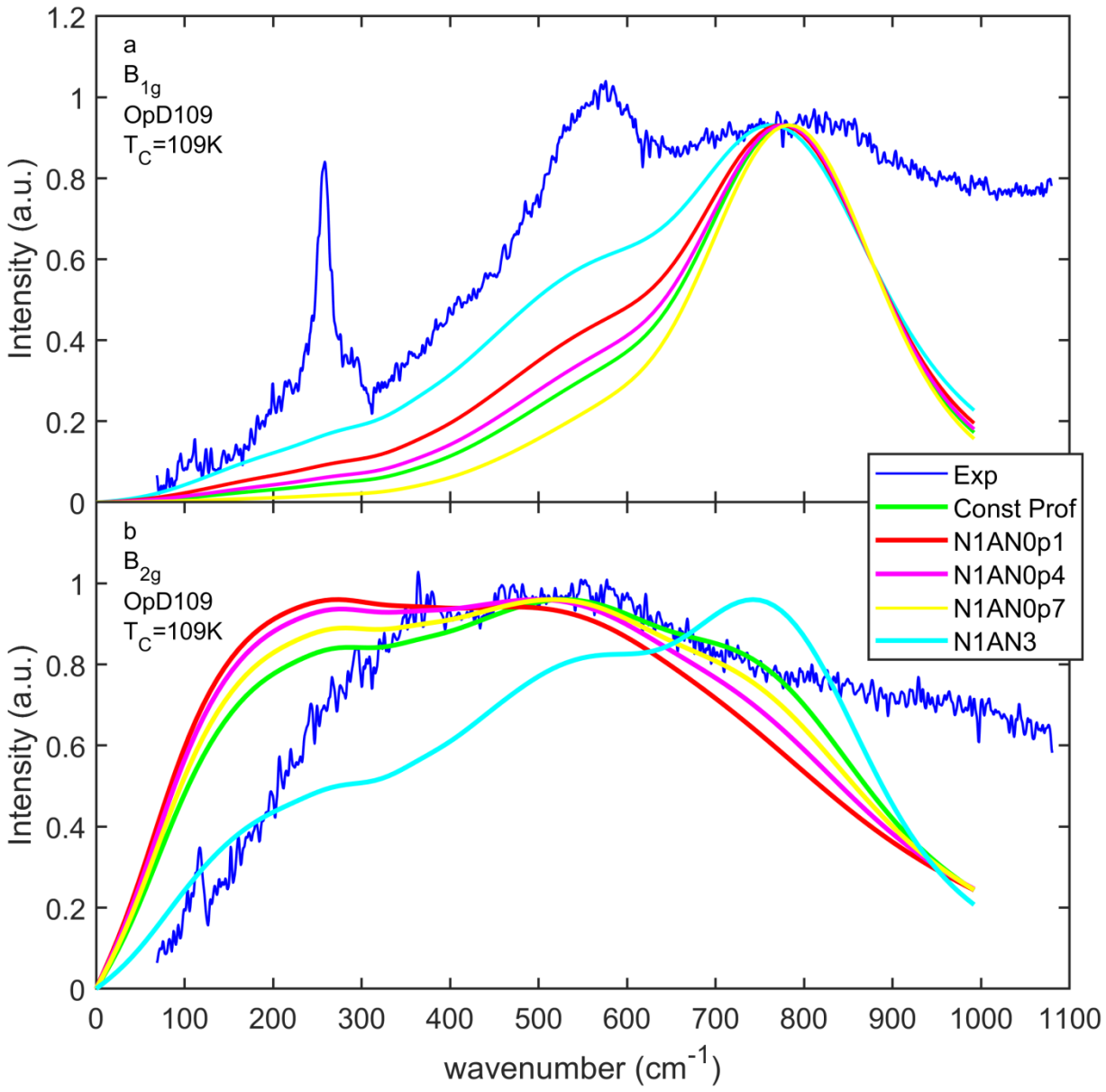

Fig.5.28 Experimental Raman spectra and calculated IP contribution to the Raman spectra with different linear profiles for the optimally doped Bi2223 sample in **a** B_{1g} configuration and **b** B_{2g} configuration.

together with suppression of the antinodal region, however the peak is almost unchanged. The only minute changes that are visible are a tiny shift at a higher frequency and a minute sharpening of the peak when the antinodal intensity is suppressed. The shift at higher frequency would be an improvement, since as discussed earlier, the peak position is slightly underestimated. However, the shift is so tiny that it can hardly be considered a significant improvement. In Fig.5.28 (b) the B_{2g} calculated intensity for the IP with different linear profiles is also shown. These calculated spectra suffer greatly from the previously discussed limitations of the nodal IP band fit, and the three artefact humps are visible. Apart from those, no significant improvement is observed when the profile is changed. Suppressing the antinodal region makes the peak shift at lower frequency,

while enhancing it shifts the peak at higher frequency, additionally the overall shape seems to be modified in both cases. However since the starting peak position and the overall shape of the calculated spectrum with constant profile are already quite good, these modifications of the spectral profile seem to lead only to a worsening of the calculated spectrum. Therefore, considering both configurations, also in the case of the inner plane our choice of profile that gives the calculated spectrum better representing the experimental one is again the constant profile. However, we do feel that these data do not exclude the possibility of an improvement with different profiles if a different ARPES dataset was to be used, especially for the underdoped inner plane, since this failure of the different profiles to give a better reproduction of the Raman spectra may be simply due to the previously discussed limitations of this ARPES data. More specifically the IP band is extremely weak in the nodal and antinodal region, and while this may be sufficient to roughly reproduce the peak position under the right assumptions, it may not be sufficient to reproduce a consistent evolution of the contribution along the Fermi surface, preventing therefore relevant observations when the profile is changed. Since the IP is underdoped, it is especially on this layer contribution that we expected a decreasing antinodal weight to be beneficial, since this has been shown in the previous kinetic calculation for single and double layer components, [47], [49], [142], [143] and we also were able to show it in this work in the case of underdoped Bi2212.

In conclusion, even if the IP intensity is extremely weak, we were able to separate the IP and OP band intensity in the ARPES input data and reproduce well the experimental Raman spectra of Bi2223. The fact that we can reproduce the energies of the two experimental peaks observed in this work in the B_{1g} spectra, using the separated OP and IP intensities, constitutes a strong evidence that our assignment of the peaks is correct, and that the double peak structure truly originates from the two superconducting gaps on the OP and IP bands. Unfortunately the limitations of the ARPES data forced us to perform some assumptions on the IP band in the nodal and antinodal region. These assumptions, while being sufficient to reproduce the B_{1g} peaks energy, are likely to prevent us from drawing further conclusions on the bands ratio and on the intensity profile along the Fermi surface. For this reason, the enhancement of the IP intensity, and therefore the obtained band ratio of 1.7, that was used to reproduce the Raman spectra, is likely to carry little physical meaning, and should be viewed as a mere fitting parameter. Since suppressing the antinodal region gave an improvement of the calculated spectra in the case of underdoped Bi2212 samples, both in the present work and in previous calculation, we expected the same improvement in the underdoped IP contribution to the Raman spectra, however this was not observed. The reason for this is again likely to be the weakness of the IP band in the input ARPES data, which forced some assumptions on the IP band.

6: Conclusions

6.1: Bi2223 experimental Raman results

In this work we obtained Bi2223 samples of four different doping levels, spanning from a slightly overdoped sample to a strongly underdoped one, through annealing in oxygen atmosphere. The samples were characterized by SQUID magnetometry and by X-ray diffraction to evaluate the critical temperature and the average sample doping level.

Raman scattering measurement revealed a double pair-breaking peak structure in the low temperature B_{1g} spectra, which was never observed before in the Raman spectra of Cuprates. We interpret this double peak structure as a Raman direct signature of the double superconducting gap of the triple layer cuprate Bi2223, originating from the two inequivalent Cu-O_2 layers, the inner and the outer plane. The two peaks energies values for the optimally doped sample were found to be consisted with the gap energies values found by ARPES in the literature.

Within our experimental resolution the two peaks were found to be appearing at the same temperature. The different hole concentration in these two layers could lead to two different critical temperatures for the two kinds of layers, however since the two peaks were found to appear simultaneously at the same temperature, this points to an interaction between the two layers. In this picture, through tunneling of Cooper pairs between the layers, the layer with the highest critical temperature drives the layer with lower critical temperature to superconduct at higher temperatures.

Under the assumption that the doping imbalance between the two different Cu-O_2 layers of Bi2223 does not change when the average doping of the sample is changed, we were able to estimate the layer doping level, starting from the layer doping level found by NMR for the optimally doped sample, also for the remaining samples.

Going from the optimally doped sample to the lower doping sample, the energy of the B_{1g} peaks increased, both for the inner and outer plane peak, while that of the B_{2g} peak decreases, meaning that the two energy scale that was observed in the other single and double layer cuprates, has been found also in the triple layer Bi2223. The present result constitutes, to our knowledge, the first doping dependent spectroscopic study on the triple layer cuprates where the OP and the IP signals were resolved.

Considering that the superconducting gap was found to be constant in a broad range of doping by ARPES, the increase in the B_{1g} pair breaking peaks energy with lower doping is strange. Since the antinodal gap, which is associated with the pseudogap is increasing with lower doping, one possible explanation is to assume that, despite the competition between the pseudogap state and superconductivity, some positive interaction also exists between the two and that this enhances the pair-breaking energy in the antinodal region with lower doping. However even if the antinodal superconducting energy is enhanced, the two state still competes, and superconductivity gets

gradually expelled from the antinode when the hole content decreases. This could explain why the B_{1g} pair breaking peaks energy increases with lower doping but the same time it loses intensity and T_C is suppressed.

Additionally, when the layer doping estimated was used to plot the B_{1g} peaks energy, we found that the inner and outer plane energies seem to align on a single line, and this unifying picture is surprising. This seems to imply that despite the chemical and structural differences between the two layers, the peak energy is not different, and is only influenced by the layer doping. This is likely to be due to proximity effects, where the interaction between the two layers averages out the value of the two gaps.

Finally after the division of the peak energy, by the maximum sample critical temperature, we found that this ratio $PE/k_BT_{C,MAX}$ is much higher in Bi2223 than in the other single and double layer cuprates, meaning that Bi2223 has a low T_C relative to its large gap value. This is likely to be a multilayer effect. There are several possible explanations for the increased IP gap, that could include: protection from the blocking layer disorders[8], high next-nearest neighbor hoping value *t'*,[7] or the strong pseudogap in this underdoped layer if we assume some degree of positive interaction with superconductivity as discussed above. The tunneling of Cooper pairs could average the IP and OP gaps out, giving large values for both of the two, and increasing the superfluid density of the underdoped IP.[158] All of these effects could contribute to increase the peak energy PE value, while the T_C could be reduced by the competition of the strong pseudogap state, originating from the underdoped IP, with superconductivity, confining the Cooper pairs towards the antinode. The combination of these effect could explain the large ratio $PE/k_BT_{C,MAX}$ found here.

All of these considerations point to a complex situation in the triple layer components, where the combination of multilayer effects, and the non-trivial relationship between superconductivity and the pseudogap, could give the right condition for the high T_C of these materials.

6.2: Bi2212 Raman results analysis based on ARPES

In this work we were able to reproduce the Bi2212 Raman spectra starting from the ARPES experimental data for samples of three different dopings using the Kubo formalism.

The more realistic Raman spectra obtained, with respect to the previous calculations using the kinetic theory, show the advantage of this method. Using the experimental ARPES data as an input we can introduce naturally the scattering rates in the calculation, and correctly account for the experimental band anomalies, which are ignored in calculations using assumed tight binding-like bands as input.

Assuming constant intensity profiles along the Fermi surface we could reproduce correctly the overdoped and optimally doped Raman spectra, with good reproduction of the overall shape and

only a small overestimation of the peak positions. However we could not reproduce correctly the underdoped sample spectra. To improve the fit of this sample we had to assume a particular intensity profile along the band, suppressing the antinodal intensity (and also the most nodal cut). With this suppression of the antinodal weight, both the B_{1g} and B_{2g} configuration spectra were improved, and we were able to obtain the correct doping dependence, namely the two energy scale. This result is analogous to the result of previous kinetic theory calculations, [47], [49], [142], [143] where the antinodal intensity is suppressed to improve the calculation results. This can be explained by the competition between superconductivity and the pseudogap state, where in the underdoped samples the Cooper pairs are confined in the nodal region, and therefore it is necessary to suppress the contribution of the pseudogap dominated antinodal states for the correct calculation of the pair breaking Raman peak behavior. The fact that we can reproduce the doping dependence of the nodal B_{2g} Raman peak in the underdoped side, starting from the doping independent ARPES nodal gap, shows that there is no inconsistency between the two techniques, but that this is an effect of the different way the two techniques pick up the confinement of the Cooper pairs in the nodal region caused by the competition of the pseudogap with superconductivity.

In all of our calculation both the B_{1g} and B_{2g} configuration peak positions are overestimated. This could be also caused by a difference in the effect of the pseudogap in the two techniques ARPES and Raman. The pseudogap state is only weakly visible in Raman as a suppression of spectral weight, but it has a strong effect in ARPES dominating the antinodal spectra. This could mean that ARPES is more sensible to the pseudogap. Therefore it is plausible that in the calculation of the Raman spectra starting from the ARPES data, the pseudogap dominated spectra increase the calculated Raman peak energy, leading to an overestimation of the peak position.

In conclusion these calculations proved the viability of the Kubo calculation of the Raman spectra starting from the experimental ARPES data and show that the apparent inconsistency between the two techniques may be due only to a difference in how the two pick up the pseudogap effect.

6.3: Bi2223 Raman results analysis based on ARPES

In this work we were also able to reproduce the optimally doped Bi2223 Raman spectra, starting from the ARPES experimental data, using the Kubo formalism.

This calculation is challenged by the fact that the signal from the inner plane band is extremely weak in the nodal and antinodal region. Despite this difficulty we were able to separate the inner and outer plane ARPES intensity by fitting the EDCs with Gaussian peaks, and fixing different fit parameters to solve the problem of the weakness of the IP band.

This allowed us to calculate separately the IP and OP band contribution to the Raman spectra, and the striking result was that these two gave a peak in the B_{1g} Raman spectra at distinct energy positions, which correspond to the energy positions of the two experimental Raman peaks found

in this work. This finding is a strong proof supporting our assignment of the two peaks to double superconducting gap of Bi2223 originating from the inner and outer plane gaps respectively.

Contrary to the Bi2212 case, here the peak positions in the B_{1g} configuration were underestimated slightly. In the case of the OP this difference may be due to the fact that the ARPES data used as an input do not reach the end of the first Brillouin zone, but stop at a slightly less antinodal momentum.

We were able to correctly reproduce the shape of both the B_{1g} and the B_{2g} configurations, even though the IP intensity had to be enhanced even after the two band intensity was normalized along the Fermi surface. The fact that the IP intensity had to be enhanced may not have any physical meaning, but it may only be due to the limitations of the ARPES data, where the IP intensity is extremely weak, and forces us to assume some parameters for the EDC peaks, that may lead to the underestimation of the IP contribution to the Raman spectrum.

The dependence of the OP and IP contribution on the intensity profile of the bands along the Fermi surface was investigated, as in the case of Bi2212. However no clear improvement of the spectra was found, even for the underdoped IP contribution which was expected to show some improvement of the calculated spectra with a decreasing antinodal intensity, basing on the previous Bi2212 results. This may be again due to the weakness of the IP band, which may prevent us from seeing the dependence on the band intensity profile for the same reason that we just discussed.

In conclusion, even if this calculation is hindered by the weakness of the IP band in the input ARPES data, we were able to give a solid evidence that the assignment of the experimental double peak structure is correct. Unfortunately the limitation of the ARPES data prevents us to draw ulterior conclusions on the intensity profile of the band along the Fermi surface or on the ratio of the two bands intensity.

6.4: Closing remarks

The present results hint to a complex situation in the multilayer cuprates, where the combination of multilayer effects and the non-trivial relationship between superconductivity and the pseudogap may give the high T_C of these samples. Since the complex physics of these materials is still poorly understood, these new experimental findings may help to lay the foundation of future experimental and theoretical works.

Publications

- G. Vincini, K. Tanaka, T. Adachi, L. Sobirey, S. Miyasaka, S. Tajima, S. Adachi, N. Sasaki, T. Watanabe, Double pair breaking peak in Raman scattering spectra of triple layer cuprate Bi2223. (submitted for publication to Physical Review B in May 2018)

- N.T. Hieu, G. Vincini, K. Tanaka, T. Masui, S. Miyasaka, S. Tajima, T. Sasagawa, Quantitative comparison between electronic Raman scattering and angle resolved photoemission spectra in $Bi_2Sr_2CaCu_2O_{8+\delta}$ superconductors: Doping dependence if the nodal and antinodal superconducting gap. (in preparation)

- G. Vincini, K. Tanaka, T. Adachi, L. Sobirey, S. Miyasaka, S. Tajima, S. Adachi, N. Sasaki, T. Watanabe, Quantitative comparison between electronic Raman scattering and angle resolved photoemission spectra in the triple layer cuprate Bi2223 (in preparation)

Conference presentations

- Physical Society of Japan (JPS) Autumn meeting 2016, Giulio Vincini, L. Sobirey, K. Tanaka, T. Adachi, N. Murai, S. Miyasaka, S. Tajima, S. Adachi,T. Watanabe, Double pair breaking peak in triple layer cuprate Bi2223

- 29th International Superconductivity Symposium (ISS2016) Tokyo, Japan, Giulio Vincini, K. Tanaka, T. Adachi, N. Murai, S. Miyasaka, S. Tajima, S. Adachi,T. Watanabe, Double pair breaking peak in triple layer cuprate Bi2223 (poster presentation)

- Physical Society of Japan (JPS) Autumn meeting 2017, Giulio Vincini, K. Tanaka, T. Adachi, S. Miyasaka, S. Tajima, S. Adachi, T. Watanabe, Doping dependence of the double pair breaking peak in triple layer cuprate Bi2223

- Physical Society of Japan (JPS) Annual (73th) meeting 2018, Giulio Vincini, K. Tanaka, S. Ideta, T. Adachi, S. Miyasaka, S. Tajima, S. Adachi, T. Watanabe, A. Fujimori, Analysis of Raman spectra of Bi-based cuprates using ARPES results

Acknowledgements

This work was made possible thanks to all the wonderful people that assisted me greatly and to those who made my life in Japan wonderful. Here I would like to express my sincerest gratitude to all of these people.

Firstly I am deeply grateful to Prof. Setsuko Tajima, for accepting me in her laboratory, and guiding me through these years in an extremely professional but cheerful attitude. Her assistance was invaluable both for my studies and for my life in Japan.

Secondly I would like to thank Prof. Shigeki Miyasaka, whose assistance was vital to my research and whose help with the experimental and organizational issues was irreplaceable, both for me and for all the other member of Tajima Lab.

My deep thanks go also to Prof. Masamichi Nakajima, for his assistance with experimental an everyday lab life issues.

I would like to thank profoundly Prof. Kiyohisa Tanaka for his invaluable guidance in the Kubo calculations showed in this work. I also thank sincerely Prof. Shinichiro Ideta for providing and discussing with me his Bi2223 ARPES data. I also have to thank deeply these two professors for their wonderful hospitality in the National Institute for Molecular Science, in Okamachi.

I am deeply thankful to Prof. Watanabe, for his collaboration, useful comments on my work and for providing me the Bi2223 high quality crystals that were used for my research. I am also deeply grateful to S. Adachi, N. Sasaki, and all the other members of Prof. Watanabe group that were involved in the growth of the samples.

I would also like to express my deep gratitude to the laboratory secretaries, Ms. Ayako Owaki and before her Ms. Yoshiko Ishimoto. They have both helped me greatly during my stay, and they have treated me with great kindness, for which I am extremely grateful. I also want to express my appreciation to Ms. Hitomi Ami for her assistance with both private and university matters and for helping in my Japanese studies by organizing the Japanese Half-Hour in the Science Buddy program at the Graduate School of Science.

I would also like to express my most sincere gratitude to all the other members of Tajima Lab. who helped me greatly with my experiments, everyday life, and who made my life in Japan much more cheerful with their friendship. I thank Dr. Tatsuya Kobayashi for his guidance and Dr. Naoki Murai for his precious help with the Raman instrumentation. I am profoundly grateful to Dr. Toru Adachi for his invaluable assistance with research and everyday matters, and most of all for his sincere friendship. I thank deeply Mr. Zi How Tin, for his precious help with my research and for his wonderful friendship. I would also like to extend my most sincere gratitude to all the members of Tajima Lab, both older and younger than me, who I am not explicitly mentioning here. It is also thanks to all of these people efforts that the group is a good environment to carry out our research in a cheerful and positive manner.

I would like to thank the people that helped me with my Japanese studies, by giving their time for free. I am sincerely thankful to Mrs. Mihoko Inoue for helping me with my studies for more than a year, and later for organizing the lessons. I am deeply grateful to Mrs. Chie Sekiguchi for her long assistance with my Japanese studies and for her friendship.

I am extremely grateful to my family, for their unconditional love, for always pushing me to become a better person and accomplish good results in my life. Needless to say I would have never reached this point in my life without their loving guidance.

I am also profoundly grateful to my best friend Matteo for always being close to me and my family, even while being almost on the other side of the globe.

Finally, I am incredibly thankful to Andrea, my future wife, for all the joy that she brought to my life, and for her invaluable support that allowed me to complete my studies. She has also contributed actively in this thesis by editing some of the figures here presented.

Giulio Vincini

Osaka, 07/15/2018

References

[1] M. Hashimoto, I. M. Vishik, R.-H. He, T. P. Devereaux, and Z.-X. Shen, "Energy gaps in high-transition-temperature cuprate superconductors," *Nat. Phys.*, vol. 10, no. 7, pp. 483–495, 2014.

[2] I. M. Vishik *et al.*, "Phase competition in trisected superconducting dome," *Proc. Natl. Acad. Sci.*, vol. 109, no. 45, pp. 18332–18337, 2012.

[3] J. Mesot *et al.*, "Superconducting Gap Anisotropy and Quasiparticle Interactions : A Doping Dependent Photoemission Study," *Phys. Rev. Lett.*, vol. 83, no. 4, p. 840, 1999.

[4] S. V Borisenko *et al.*, "Superconducting gap in the presence of bilayer splitting in underdoped (Pb,Bi)2Sr2CaCu2O8+δ," *Phys. Rev. B*, vol. 66, p. 140509, 2002.

[5] A. Iyo *et al.*, "T c vs n Relationship for Multilayered High- T c Superconductors," *J. Phys. Soc. Jpn.*, vol. 76, no. 9, pp. 094711–094716, 2007.

[6] S. Chakravarty, H. Kee, and K. Volker, "An explanation for a universality of transition temperatures in families of copper oxide superconductors," *Nature*, vol. 428, pp. 53–55, 2004.

[7] E. Pavarini, I. Dasgupta, T. Saha-Dasgupta, O. Jepsen, and O. K. Andersen, "Band-Structure Trend in Hole-Doped Cuprates and Correlation with Tc max," *Phys. Rev. Lett.*, vol. 87, no. 4, p. 047003, 2001.

[8] H. Eisaki *et al.*, "Effect of chemical inhomogeneity in bismuth-based copper oxide superconductors," *Phys. Rev. B*, vol. 69, p. 064512, 2004.

[9] H. Mukuda, S. Shimizu, A. Iyo, and Y. Kitaoka, "High-Tc Superconductivity and Antiferromagnetism in Multilayered Copper Oxides ---A New Paradigm of Superconducting Mechanism," *J. Phys. Soc. Jpn.*, vol. 81, p. 011008, 2012.

[10] J. Bardeen, L. N. Cooper, and J. R. Schrieffer, "Theory of Superconductivity," *Phys. Rev.*, vol. 108, p. 1175, 1957.

[11] M. L. Cohen, "Comments on the Maximum Superconducting Transition Temperature," *AIP Conf. Proc.*, vol. 4, p. 17, 1972.

[12] J. G. Bednorz and K. . A. Miiller, "Condensed Matt Possible High T c Superconductivity in the Ba - L a - C u - 0 System," *Zeitschrift für Phys. B Condens. Matter*, vol. 64, pp. 189–193, 1986.

[13] A. Schilling, M. Cantoni, J. D. Guo, and H. R. Ott, "Superconductivity above 130 K in the Hg–Ba–Ca–Cu–O system," *Nature*, vol. 363, pp. 56–58, 1993.

[14] P. Dai, B. C. Chakoumakos, G. F. Sun, K. W. Wong, Y. Xin, and D. F. Lu, "Synthesis and neutron powder diffraction study of the superconductor HgBa2Ca2Cu3O8 + δ by Tl substitution," *Phys. C Supercond. its Appl.*, vol. 243, no. 3–4, pp. 201–206, 1995.

[15] Y. Kamihara *et al.*, "Iron-Based Layered Superconductor: LaOFeP," *J. Am. Chem. Soc.*, vol. 128, no. 31, pp. 10012–10013, 2006.

[16] Y. Kamihara, T. Watanabe, M. Hirano, and H. Hosono, “Iron-Based Layered Superconductor La[O1-xFx]FeAs (x = 0.05−0.12) with Tc = 26 K,” *J. Am. Chem. Soc.*, vol. 130, no. 11, pp. 3296–3297, 2008.

[17] A. P. Drozdov, M. I. Eremets, I. A. Troyan, V. Ksenofontov, and S. I. Shylin, “Conventional superconductivity at 203 kelvin at high pressures in the sulfur hydride system,” *Nature*, vol. 525, pp. 73–76, 2015.

[18] Y. Wang and Y. Ma, “Perspective: Crystal structure prediction at high pressures,” *J. Chem. Phys.*, vol. 140, p. 040901, 2014.

[19] P. J. Ray, “Structural investigation of La(2-x)Sr(x)CuO(4+y) - Following staging as a function of temperature,” University of Copenhagen, 2015.

[20] N. Barišić *et al.*, “Universal sheet resistance and revised phase diagram of the cuprate high-temperature superconductors,” *Proc. Natl. Acad. Sci.*, vol. 110, no. 30, pp. 12235–12240, 2013.

[21] R. S. Markiewicz, S. Sahrakorpi, M. Lindroos, H. Lin, and A. Bansil, “One-band tight-binding model parametrization of the high-Tc cuprates including the effect of kz dispersion,” *Phys. Rev. B*, vol. 72, no. 5, p. 54519, 2005.

[22] Z.-X. Shen *et al.*, “Anomalously large gap anisotropy in the a-b plane of Bi2Sr2CaCu2O8+δ,” *Phys. Rev. Lett.*, vol. 70, no. 10, pp. 1553–1556, 1993.

[23] I. M. Vishik *et al.*, “Doping-Dependent Nodal Fermi Velocity of the High-Temperature Superconductor Bi2Sr2CaCu2O8+δ Photoemission Spectroscopy,” *Phys. Rev. Lett.*, vol. 104, no. 20, p. 207002, 2010.

[24] B. Batlogg *et al.*, “Isotope Effect in the High-Tc Superconductors Ba2YCu3O7 and Ba2EuCu3O7,” *Phys. Rev. Lett.*, vol. 58, no. 22, pp. 2333–2336, 1987.

[25] A. Mourachkine, “The oxygen isotope effect on critical temperature in superconducting copper oxides,” *Supercond. Sci. Technol.*, vol. 17, no. 4, pp. 721–723, 2004.

[26] X. Chen *et al.*, “Oxygen isotope effect in Bi2Sr2Can−1CunO2n+4+δ (n=1,2,3) single crystals,” *Phys. Rev. B*, vol. 76, p. 140502, 2007.

[27] V. L. Ginzburg and L. D. Landau, “On the Theory of superconductivity,” *Zh.Eksp.Teor.Fiz.*, vol. 20, pp. 1064–1082, 1950.

[28] V. L. Ginzburg, “Once again about high-temperature superconductivity,” *Contemp. Phys.*, vol. 33, no. 1, pp. 15–23, 1992.

[29] N. E. Hussey, K. Takenaka, and H. Takagi, “Universality of the Mott–Ioffe–Regel limit in metals,” *Philos. Mag.*, vol. 84, no. 27, pp. 2847–2864, 2004.

[30] E. Fradkin, S. A. Kivelson, and J. M. Tranquada, “Colloquium: Theory of intertwined orders in high temperature superconductors,” *Rev. Mod. Phys.*, vol. 87, no. 2, pp. 457–482, 2015.

[31] B. Keimer, S. A. Kivelson, M. R. Norman, S. Uchida, and J. Zaanen, “From quantum matter to high-temperature superconductivity in copper oxides,” *Nature*, vol. 518, no. 7538, pp. 179–186, 2015.

[32] P. W. Anderson, “The Resonating Valence Bond State in La2CuO4 and Superconductivity,” *Science (80-.).*, vol. 235, no. 4793, p. 1196 LP-1198, Mar. 1987.

[33] A. Damascelli, Z. Hussain, and Z.-X. Shen, “Angle-resolved photoemission studies of the cuprate superconductors,” *Rev. Mod. Phys.*, vol. 75, no. 2, pp. 473–541, Apr. 2003.

[34] E. Dagotto, “Correlated electrons in high-temperature superconductors,” *Rev. Mod. Phys.*, vol. 66, no. 3, pp. 763–840, 1994.

[35] J. L. Tallon, C. Bernhard, H. Shaked, R. L. Hitterman, and J. D. Jorgensen, “Generic superconducting phase behavior in high-Tc cuprates: Tc variation with hole concentration in YBa2Cu3O7-δ,” *Phys. Rev. B*, vol. 51, no. 18, p. 12911, 1995.

[36] M. R. Presland, J. L. Tallon, R. G. Buckley, R. S. Liu, and N. E. Flower, “General trends in oxygen stoichiometry effects on Tc in Bi and Tl superconductors,” *Phys. C Supercond.*, vol. 176, no. 1, pp. 95–105, 1991.

[37] S. Blanco-Canosa *et al.*, “Resonant x-ray scattering study of charge-density wave correlations in YBa 2 Cu 3 O 6 + x,” *Phys. Rev. B*, vol. 054513, no. 90, pp. 43–45, 2014.

[38] T. P. Devereaux, D. Einzel, B. Stadlober, R. Hackl, D. H. Leach, and J. J. Neumeier, “Electronic Raman scattering in high-Tc superconductors: A probe of dx2-y2 pairing,” *Phys. Rev. Lett.*, vol. 72, no. 3, pp. 396–399, 1994.

[39] T. P. Devereaux and D. Einzel, “Electronic Raman scattering in superconductors as a probe of anisotropic electron pairing,” *Phys. Rev. B*, vol. 51, no. 22, pp. 16336–16357, 1995.

[40] H. Ding *et al.*, “Angle-resolved photoemission spectroscopy study of the superconducting gap anisotropy in Bi2Sr2CaCu2O8+x,” *Phys. Rev. B*, vol. 54, no. 14, pp. R9678--R9681, 1996.

[41] W. N. Hardy, D. A. Bonn, D. C. Morgan, R. Liang, and K. Zhang, “Precision measurements of the temperature dependence of λ in YBa2Cu3O6.95: Strong evidence for nodes in the gap function,” *Phys. Rev. Lett.*, vol. 70, no. 25, pp. 3999–4002, 1993.

[42] D. J. Van Harlingen, “Phase-sensitive tests of the symmetry of the pairing state in the high-temperature superconductors---Evidence for dx2−y2 symmetry,” *Rev. Mod. Phys.*, vol. 67, no. 2, pp. 515–535, Apr. 1995.

[43] K. Tanaka *et al.*, “Distinct Fermi-Momentum-Dependent Energy Gaps in Deeply Underdoped Bi2212,” *Science (80-.).*, vol. 314, no. 5807, pp. 1910–1913, 2006.

[44] T. Kondo, R. Khasanov, T. Takeuchi, J. Schmalian, and A. Kaminski, “Direct evidence for a competition between the pseudogap and high temperature superconductivity in the cuprates,” *Nature*, vol. 457, no. January, pp. 296–300, 2009.

[45] J. Zhao *et al.*, “Universal features in the photoemission spectroscopy of high-temperature superconductors,” *Proc. Natl. Acad. Sci.*, vol. 110, no. 44, pp. 17774–17777, 2013.

[46] S. Sugai, H. Suzuki, Y. Takayanagi, T. Hosokawa, and N. Hayamizu, “Carrier-density-dependent momentum shift of the coherent peak and the LO phonon mode in p -type high-T c superconductors,” *Phys. Rev. B*, vol. 68, p. 184504, 2003.

[47] M. LE Tacon *et al.*, “Two energy scales and two distinct quasiparticle dynamics in the

superconducting state of underdoped cuprates," *Nat. Phys.*, vol. 2, pp. 537–543, 2006.

[48] S. Blanc *et al.*, "Quantitative Raman measurement of the evolution of the Cooper-pair density with doping in Bi 2 Sr 2 CaCu 2 O 8 + □ superconductors," *Phys. Rev. B*, vol. 80, p. 140502, 2009.

[49] S. Blanc *et al.*, "Loss of antinodal coherence with a single d-wave superconducting gap leads to two energy scales for underdoped cuprate superconductors.," *Phys. Rev. B*, vol. 82, p. 144516, 2010.

[50] L. B. Ioffe and A. J. Millis, "d-Wave superconductivity in doped Mott insulators," *J. Phys. Chem. Solids*, vol. 63, pp. 2259–2268, 2002.

[51] K. McElroy *et al.*, "Coincidence of Checkerboard Charge Order and Antinodal State Decoherence in Strongly Underdoped Superconducting Bi 2 Sr 2 CaCu 2 O 8 + δ," *Phys. Rev. Lett.*, vol. 94, p. 197005, 2005.

[52] Y. Kohsaka *et al.*, "How Cooper pairs vanish approaching the Mott insulator in Bi 2 Sr 2 CaCu 2 O 8 1 d," *Nature*, vol. 454, p. 1072, 2008.

[53] D. L. Feng *et al.*, "Signature of Superfluid Density in the Single-Particle Excitation," *Science (80-.).*, vol. 289, pp. 277–281, 2000.

[54] H. Ding *et al.*, "Coherent Quasiparticle Weight and Its Connection to High- T c Superconductivity from Angle-Resolved Photoemission," *Phys. Rev. Lett.*, vol. 87, no. 22, p. 227001, 2001.

[55] I. M. Vishik *et al.*, "A momentum-dependent perspective on quasiparticle interference in Bi 2 Sr 2 CaCu 2 O 8 + δ," *Nat. Phys.*, vol. 5, no. 10, pp. 718–721, 2009.

[56] Y. J. Uemura *et al.*, "Universal Correlations between Tc and ns/m∗ (Carrier Density over Effective Mass) in High-Tc Cuprate Superconductors," *Phys. Rev. Lett.*, vol. 62, no. 19, pp. 2317–2320, 1989.

[57] V. J. Emery and S. A. Kivelson, "Importance of phase fluctuations in superconductors with small superfluid density," *Nature*, vol. 374, p. 434, Mar. 1995.

[58] A. Lanzara *et al.*, "Evidence for ubiquitous strong electron–phonon coupling in high-temperature superconductors," *Nature*, vol. 412, p. 510, Aug. 2001.

[59] D. Reznik *et al.*, "Electron–phonon coupling reflecting dynamic charge inhomogeneity in copper oxide superconductors," *Nature*, vol. 440, p. 1170, Apr. 2006.

[60] S. Raghu, S. A. Kivelson, and D. J. Scalapino, "Superconductivity in the repulsive Hubbard model: An asymptotically exact weak-coupling solution," *Phys. Rev. B*, vol. 81, no. 22, p. 224505, 2010.

[61] D. J. Scalapino, "A common thread: The pairing interaction for unconventional superconductors," *Rev. Mod. Phys.*, vol. 84, no. 4, pp. 1383–1417, 2012.

[62] M. Le Tacon *et al.*, "Intense paramagnon excitations in a large family of high-temperature superconductors," *Nat. Phys.*, vol. 7, p. 725, Jul. 2011.

[63] M. P. M. Dean *et al.*, “Persistence of magnetic excitations in La2−xSrxCuO4 from the undoped insulator to the heavily overdoped non-superconducting metal,” *Nat. Mater.*, vol. 12, p. 1019, Aug. 2013.

[64] H. F. Fong *et al.*, “Spin susceptibility in underdoped YBa2Cu3O6+x,” *Phys. Rev. B*, vol. 61, no. 21, pp. 14773–14786, 2000.

[65] P. Dai, H. A. Mook, R. D. Hunt, and F. Do\ifmmode \breveg\else \ug\fian, “Evolution of the resonance and incommensurate spin fluctuations in superconducting YBa2Cu3O6+x,” *Phys. Rev. B*, vol. 63, no. 5, p. 54525, 2001.

[66] W. W. Warren *et al.*, “Cu spin dynamics and superconducting precursor effects in planes above Tc in YBa2Cu3O6.7,” *Phys. Rev. Lett.*, vol. 62, no. 10, pp. 1193–1196, Mar. 1989.

[67] H. Alloul, T. Ohno, and P. Mendels, “89 Y NMR evidence for a fermi-liquid behavior in YBa2Cu3O6+x,” *Phys. Rev. Lett.*, vol. 63, no. 16, pp. 1700–1703, 1989.

[68] C. C. Homes, T. Timusk, R. Liang, D. A. Bonn, and W. N. Hardy, “Optical conductivity of c axis oriented YBa2Cu3O6.70: Evidence for a pseudogap,” *Phys. Rev. Lett.*, vol. 71, no. 10, pp. 1645–1648, 1993.

[69] C. Renner, B. Revaz, J.-Y. Genoud, K. Kadowaki, and \O. Fischer, “Pseudogap Precursor of the Superconducting Gap in Under- and Overdoped Bi2Sr2CaCu2O8+δ,” *Phys. Rev. Lett.*, vol. 80, no. 1, pp. 149–152, 1998.

[70] M. R. Norman *et al.*, “Destruction of the Fermi surface in underdoped high-Tc superconductors,” *Nature*, vol. 392, p. 157, Mar. 1998.

[71] M. R. Norman, D. Pines, and C. Kallin, “The pseudogap: friend or foe of high T c ?,” *Adv. Phys.*, vol. 54, no. 8, pp. 715–733, Dec. 2005.

[72] T. C. Hsu, J. B. Marston, and I. Affleck, “Two observable features of the staggered-flux phase at nonzero doping,” *Phys. Rev. B*, vol. 43, no. 4, pp. 2866–2877, Feb. 1991.

[73] C. M. Varma, “Pseudogap Phase and the Quantum-Critical Point in Copper-Oxide Metals,” *Phys. Rev. Lett.*, vol. 83, no. 17, pp. 3538–3541, 1999.

[74] S. Chakravarty, R. B. Laughlin, D. K. Morr, and C. Nayak, “Hidden order in the cuprates,” *Phys. Rev. B*, vol. 63, no. 9, p. 94503, 2001.

[75] W. S. Lee *et al.*, “Abrupt onset of a second energy gap at the superconducting transition of underdoped Bi2212,” *Nature*, vol. 450, no. November, pp. 81–84, 2007.

[76] A. Kaminski, T. Kondo, T. Takeuchi, and G. Gu, “Pairing, pseudogap and Fermi arcs in cuprates,” *Philos. Mag.*, vol. 95, no. 5–6, pp. 453–466, Feb. 2015.

[77] M. Hashimoto *et al.*, “Particle–hole symmetry breaking in the pseudogap state of Bi2201,” *Nat. Phys.*, vol. 6, no. 6, pp. 414–418, Apr. 2010.

[78] R.-H. He *et al.*, “From a Single-Band Metal to a High-Temperature Superconductor via Two Thermal Phase Transitions,” *Science (80-.).*, vol. 331, no. 6024, p. 1579 LP-1583, Mar. 2011.

[79] U. Chatterjee *et al.*, “Observation of a d-wave nodal liquid in highly underdoped

Bi2Sr2CaCu2O8+δ," *Nat. Phys.*, vol. 6, p. 99, Nov. 2009.

[80] H.-B. Yang *et al.*, "Reconstructed Fermi Surface of Underdoped Bi2Sr2CaCu2O8+δ Cuprate Superconductors," *Phys. Rev. Lett.*, vol. 107, no. 4, p. 47003, 2011.

[81] A. Kanigel *et al.*, "Evidence for Pairing above the Transition Temperature of Cuprate Superconductors from the Electronic Dispersion in the Pseudogap Phase," *Phys. Rev. Lett.*, vol. 101, no. 13, p. 137002, 2008.

[82] H.-B. Yang, J. D. Rameau, P. D. Johnson, T. Valla, A. Tsvelik, and G. D. Gu, "Emergence of preformed Cooper pairs from the doped Mott insulating state in Bi2Sr2CaCu2O8+δ," *Nature*, vol. 456, p. 77, Nov. 2008.

[83] M. Hashimoto *et al.*, "Direct spectroscopic evidence for phase competition between the pseudogap and superconductivity in Bi2Sr2CaCu2O8+δ," *Nat. Mater.*, vol. 14, p. 37, Nov. 2014.

[84] T. Yoshida *et al.*, "Coexisting pseudo-gap and superconducting gap in the high-Tc superconductor La2-xSrxCuO4," *arXiv:1208.2903 [cond-mat.str-el]*, pp. 2–6, 2012.

[85] J. M. Tranquada, B. J. Sternlieb, J. D. Axe, Y. Nakamura, and S. Uchida, "Evidence for stripe correlation of spins and holes in copper oxide superconductirs," *Nature*, no. 375, pp. 561–563, 1995.

[86] M. Kofu, S.-H. Lee, M. Fujita, H.-J. Kang, H. Eisaki, and K. Yamada, "Hidden Quantum Spin-Gap State in the Static Stripe Phase of High-Temperature La2−xSrxCuO4 Superconductors," *Phys. Rev. Lett.*, vol. 102, no. 4, p. 47001, 2009.

[87] P. Corboz, T. M. Rice, and M. Troyer, "Competing States in the t-J Model: Uniform d-Wave State versus Stripe State," *Phys. Rev. Lett.*, vol. 113, no. 4, p. 46402, Jul. 2014.

[88] D. J. Scalapino and S. R. White, "Stripe structures in the t–t'-J model," *Phys. C Supercond.*, vol. 481, pp. 146–152, 2012.

[89] T. Wu *et al.*, "Magnetic-field-induced charge-stripe order in the high-temperature superconductor YBa2Cu3Oy," *Nature*, vol. 477, p. 191, Sep. 2011.

[90] E. H. da S. Neto *et al.*, "Ubiquitous Interplay between Charge Ordering and High-Temperature Superconductivity in Cuprates," *Science (80-.).*, Dec. 2013.

[91] R. Comin *et al.*, "Charge Order Driven by Fermi-Arc Instability in Bi2Sr2-xLaxCuO6+δ," *Science (80-.).*, vol. 343, no. 6169, pp. 390–392, 2014.

[92] W. Tabis *et al.*, "Charge order and its connection with Fermi-liquid charge transport in a pristine high-Tc cuprate," *Nat. Commun.*, vol. 5, p. 5875, Dec. 2014.

[93] G. Ghiringhelli *et al.*, "REPORTS Long-Range Incommensurate Charge Fluctuations in (Y,Nd)Ba 2 Cu 3 O 6+," *Science (80-.).*, vol. 337, no. August, pp. 821–825, 2012.

[94] J. Chang *et al.*, "Direct observation of competition between superconductivity and charge density wave order in YBa2Cu3O6.67," *Nat. Phys.*, vol. 8, no. 12, pp. 871–876, Oct. 2012.

[95] M. H. Hamidian *et al.*, "Atomic-scale electronic structure of the cuprate d -symmetry form

factor density wave state," *Nat. Phys.*, vol. 12, no. February, pp. 150–156, 2016.

[96] S. Blanco-Canosa *et al.*, "Resonant X-ray Scattering Study of Charge Density Wave Correlations in YBa 2 Cu 3 O 6+x," *Phys. Rev. B*, vol. 90, no. 5, p. 054513, 2014.

[97] N. Doiron-leyraud *et al.*, "Quantum oscillations and the Fermi surface in an underdoped high- T c superconductor," *Nature*, vol. 447, no. May, pp. 565–568, 2007.

[98] Y. Ando, K. Segawa, S. Komiya, and A. N. Lavrov, "Electrical Resistivity Anisotropy from Self-Organized One Dimensionality in High-Temperature Superconductors," *Phys. Rev. Lett.*, vol. 88, no. 13, p. 137005, Mar. 2002.

[99] R. Daou *et al.*, "Broken rotational symmetry in the pseudogap phase of a high-Tc superconductor," *Nature*, vol. 463, p. 519, Jan. 2010.

[100] V. Hinkov *et al.*, "Electronic Liquid Crystal State in the High-Temperature Superconductor YBa2Cu3O6.45," *Science (80-.).*, vol. 319, no. 5863, pp. 597–600, 2008.

[101] K. Fujita, M. H. Hamidian, S. D. Edkins, C. Koo, and Y. Kohsaka, "Direct phase-sensitive identification of a d -form factor density wave in underdoped cuprates," *Proc. Natl. Acad. Sci.*, pp. E3026–E3032, 2014.

[102] B. Fauqué *et al.*, "Magnetic Order in the Pseudogap Phase of High-TC Superconductors," *Phys. Rev. Lett.*, vol. 96, no. 19, p. 197001, 2006.

[103] Y. Wang *et al.*, "Onset of the vortexlike Nernst signal above Tc in La2−xSrxCuO4and Bi2Sr2−yLayCuO6," *Phys. Rev. B*, vol. 64, no. 22, p. 224519, Nov. 2001.

[104] L. Li *et al.*, "Diamagnetism and Cooper pairing above Tc in cuprates," *Phys. Rev. B*, vol. 81, no. 5, p. 054510, 2010.

[105] J. Corson, R. Mallozzi, J. Orenstein, J. N. Eckstein, and I. Bozovic, "Vanishing of phase coherence in underdoped Bi2Sr2CaCu2O8+δ," *Nature*, vol. 398, p. 221, Mar. 1999.

[106] N. Bergeal, J. Lesueur, M. Aprili, G. Faini, J. P. Contour, and B. Leridon, "Pairing fluctuations in the pseudogap state of copper-oxide superconductors probed by the Josephson effect," *Nat. Phys.*, vol. 4, p. 608, Jun. 2008.

[107] T. Kondo *et al.*, "Point nodes persisting far beyond Tc in Bi2212," *Nat. Commun.*, vol. 6, p. 7699, 2015.

[108] E. Uykur, K. Tanaka, T. Masui, S. Miyasaka, and S. Tajima, "Persistence of the superconducting condensate far above the critical temperature of YBa2 (Cu,Zn)3 Oy revealed by c -axis optical conductivity measurements for several zn concentrations and carrier doping levels," *Phys. Rev. Lett.*, vol. 112, no. 12, p. 127003, 2013.

[109] Y. Wang, L. Li, and N. P. Ong, "The Nernst effect in high-Tc superconductors," *Phys. Rev. B*, vol. 73, no. 2, p. 024510, 2005.

[110] A. Kanigel *et al.*, "Evolution of the pseudogap from Fermi arcs to the nodal liquid," *Nat. Phys.*, vol. 2, p. 447, Jun. 2006.

[111] A. V Chubukov, M. R. Norman, A. J. Millis, and E. Abrahams, "Gapless pairing and the Fermi

arc in the cuprates," *Phys. Rev. B*, vol. 76, no. 18, p. 180501, Nov. 2007.

[112] S. Kaiser *et al.*, "Optically induced coherent transport far above Tc in underdoped YBa2Cu3 O6+??," *Phys. Rev. B - Condens. Matter Mater. Phys.*, vol. 89, no. 18, pp. 1–9, 2014.

[113] S. Martin, A. T. Fiory, R. M. Fleming, L. F. Schneemeyer, and J. V Waszczak, "Normal-state transport properties of Bi2+xSr2−yCuO6+δ crystals," *Phys. Rev. B*, vol. 41, no. 1, pp. 846–849, 1990.

[114] T. R. Chien, Z. Z. Wang, and N. P. Ong, "Effect of Zn impurities on the normal-state Hall angle in single-crystal YBa2Cu3−xZnxO7−δ," *Phys. Rev. Lett.*, vol. 67, no. 15, pp. 2088–2091, 1991.

[115] C. M. Varma, P. B. Littlewood, S. Schmitt-Rink, E. Abrahams, and A. E. Ruckenstein, "Phenomenology of the normal state of Cu-O high-temperature superconductors," *Phys. Rev. Lett.*, vol. 63, no. 18, pp. 1996–1999, 1989.

[116] T. Valla, A. V Fedorov, P. D. Johnson, Q. Li, G. D. Gu, and N. Koshizuka, "Temperature Dependent Scattering Rates at the Fermi Surface of Optimally Doped Bi2Sr2CaCu2O8+δ," *Phys. Rev. Lett.*, vol. 85, no. 4, pp. 828–831, 2000.

[117] B. Vignolle *et al.*, "Quantum oscillations in an overdoped high-Tc superconductor," *Nature*, vol. 455, p. 952, Oct. 2008.

[118] U. Chatterjee *et al.*, "Electronic phase diagram of high-temperature copper oxide superconductors," *Proc. Natl. Acad. Sci.*, vol. 108, no. 23, p. 9346 LP-9349, Jun. 2011.

[119] M. Platé *et al.*, "Fermi Surface and Quasiparticle Excitations of Overdoped Tl2Ba2CuO6+δ," *Phys. Rev. Lett.*, vol. 95, no. 7, p. 77001, 2005.

[120] S. Wakimoto, H. Zhang, K. Yamada, I. Swainson, H. Kim, and R. J. Birgeneau, "Direct Relation between the Low-Energy Spin Excitations and Superconductivity of Overdoped High-Tc Superconductors," *Phys. Rev. Lett.*, vol. 92, no. 21, p. 217004, 2004.

[121] M. Mori, T. Tohyama, and S. Maekawa, "Electronic states and superconductivity in multilayer high-Tc cuprates," *Phys. Rev. B*, vol. 66, no. 6, p. 64502, 2002.

[122] D. L. Feng *et al.*, "Bilayer Splitting in the Electronic Structure of Heavily Overdoped Bi2Sr2CaCu2O8+δ," *Phys. Rev. Lett.*, vol. 86, no. 24, pp. 5550–5553, Jun. 2001.

[123] S. Ideta *et al.*, "Enhanced superconducting gaps in the trilayer high-temperature Bi 2Sr2Ca2Cu3O10+δ cuprate superconductor," *Phys. Rev. Lett.*, vol. 104, no. 22, pp. 227001–227004, 2010.

[124] Y. Tokunaga *et al.*, "Effect of carrier distribution on superconducting characteristics of the multilayered high-Tc cuprate (Cu0.6C0.4)Ba2Ca3Cu4O12+y: 63Cu−NMR study," *Phys. Rev. B*, vol. 61, no. 14, pp. 9707–9710, Apr. 2000.

[125] S. Adachi *et al.*, "Single-crystal Growth of Underdoped Bi-2223," *Phys. Procedia*, vol. 65, no. April 2016, pp. 53–56, 2015.

[126] T. Fujii, T. Watanabe, and A. Matsuda, "Single-crystal growth of Bi2Sr2Ca2Cu3O10+δ (Bi-2223) by TSFZ method," *J. Cryst. Growth*, vol. 223, no. 1–2, pp. 175–180, 2001.

[127] B. Liang and C. T. Lin, “On the growth of underdoped Bi2Sr2CaCu2O8+δ single crystals by TSFZ method,” *J. Cryst. Growth*, vol. 237–239, pp. 756–761, 2002.

[128] G. Calestani, M. G. Francesconi, G. Salsi, G. D. Andreetti, and A. Migliori, “Structural modulation and superconducting properties in (Bi, Pb) 2Sr2 (Y, Ca) Cu2Oz,” *Phys. C Supercond.*, vol. 197, no. 3, pp. 283–298, 1992.

[129] M. R. Norman, M. Randeria, H. Ding, and J. C. Campuzano, “Phenomenological models for the gap anisotropy of Bi2Sr2CaCu2O8 as measured by angle-resolved photoemission spectroscopy,” *Phys. Rev. B*, vol. 52, no. 1, pp. 615–622, 1995.

[130] S. Iwai *et al.*, “Imbalance of Hole Density between Inner and Outer Planes and Superconducting Transition Temperature in Multilayered Cuprates,” *JPS Conf. Proc.*, vol. 1, p. 012105, 2014.

[131] T. Fujii, I. Terasaki, T. Watanabe, and A. Matsuda, “Doping dependence of anisotropic resistivities in the trilayered superconductor Bi 2 Sr 2 Ca 2 Cu 3 O 10+δ,” *Phys. Rev. B*, vol. 66, p. 024507 1-5, 2002.

[132] S. Sakai *et al.*, “Raman-scattering measurements and theory of the energy-momentum spectrum for Underdoped Bi2Sr2CaCuO8+δ Superconductors: Evidence of an s-wave structure for the pseudogap,” *Phys. Rev. Lett.*, vol. 111, no. 10, pp. 2–6, 2013.

[133] N. Murai *et al.*, “Effect of out-of-plane disorder on superconducting gap anisotropy in Bi2+xSr2−xCaCu2O8+δ as seen via Raman spectroscopy,” *Phys. Rev. B*, vol. 85, p. 020507, 2012.

[134] N. Murai *et al.*, “Electronic Raman scattering on out-of-plane disordered Bi2Sr2CaCu2O8+δ: How the pseudogap affects the superconducting Raman response,” *Phys. Rev. B*, vol. 91, no. 21, p. 214520, 2015.

[135] F. Venturini, M. Opel, R. Hackl, H. Berger, L. Forro, and B. Revaz, “Doping dependence of the electronic Raman spectra in cuprates,” *J. Phys. Chem. Solids*, vol. 63, no. 12, pp. 2345–2348, 2002.

[136] X. K. Chen, J. G. Naeini, K. C. Hewitt, J. C. Irwin, R. Liang, and W. N. Hardy, “Electronic Raman scattering in underdoped YBa 2 Cu 3 O 6.5,” *Phys. Rev. B*, vol. 56, no. 2, pp. 513–516, 1997.

[137] M. Limonov, S. Lee, S. Tajima, and A. Yamanaka, “Superconductivity-induced resonant Raman scattering in multilayer high-Tc superconductors,” *Phys. Rev. B - Condens. Matter Mater. Phys.*, vol. 66, no. 5, pp. 545091–545097, 2002.

[138] B. Loret *et al.*, “Unconventional High-Energy-State Contribution to the Cooper Pairing in the Underdoped Copper-Oxide Superconductor HgBa2Ca2Cu3 O8+δ,” *Phys. Rev. Lett.*, vol. 116, no. 19, pp. 197001–197006, 2016.

[139] L. V Gasparov *et al.*, “Electronic Raman scattering of T1-2201 and T1-2223 and the symmetry of the energy gap,” *Phys. B*, vol. 223–224, pp. 484–489, 1996.

[140] A. Hoffmann, P. Lemmens, G. Giintherodt, V. Thomas, and K. Wmzer, “Electronic Raman scattering of T1-2223 and the symmetry of the superconducting gap,” *Phys. C Supercond. its Appl.*, vol. 235–240, pp. 1897–1898, 1994.

[141] A. Sacuto, R. Combescot, N. Bontemps, C. A. Muller, V. Viallet, and D. Colson, “Electronic Raman scattering in HgBa 2 Ca 2 Cu 3 O 8 ⁒ single crystals: Analysis of the superconducting state,” *Phys. Rev. B*, vol. 58, no. 17, pp. 721–733, 1998.

[142] A. Sacuto, Y. Gallais, M. Cazayous, M.-A. Measson, G. D. Gu, and D. Colson, “New insights into the phase diagram of the copper oxide superconductors from electronic Raman scattering,” 2012.

[143] A. Sacuto *et al.*, “Electronic Raman scattering in copper oxide superconductors: Understanding the phase diagram,” *Comptes Rendus Phys.*, vol. 12, no. 5–6, pp. 480–501, 2011.

[144] A. Maljuk and C. T. Lin, “Floating Zone Growth of Bi2Sr2Ca2Cu3Oy Superconductor,” *Crystals*, vol. 6, no. 5, 2016.

[145] S. De Almeida-Didry *et al.*, “Investigations for the growth of large underdoped Bi2Sr2CaCu2O8+δ single crystals,” *J. Cryst. Growth*, vol. 312, no. 3, pp. 466–470, 2010.

[146] G. D. Gu, K. Takamuku, N. Koshizuka, and S. Tanaka, “Large single crystal Bi-2212 along the c-axis prepared by floating zone method,” *J. Cryst. Growth*, vol. 130, no. 1, pp. 325–329, 1993.

[147] X. H. Chen *et al.*, “Anisotropic resistivities of single-crystal Bi2Sr2CaCu2O8+δ with different oxygen content,” *Phys. Rev. B*, vol. 58, no. 21, pp. 14219–14222, 1998.

[148] J. H. P. M. Emmen, S. K. J. Lenczowski, J. H. J. Dalderop, and V. A. M. Brabers, “Crystal growth and annealing experiments of the high Tc superconductor Bi2Sr2CaCu2O8 + δ,” *J. Cryst. Growth*, vol. 118, no. 3, pp. 477–482, 1992.

[149] T. P. Devereaux and R. Hackl, “Inelastic light scattering from correlated electrons,” *Rev. Mod. Phys.*, vol. 79, no. 1, pp. 175–233, 2007.

[150] A. A. Abrikosov and V. M. Genkin, “.,” *Sov. Phys.-JETP*, vol. 38, p. 417, 1974.

[151] M. V Klein, “Electronic raman scattering,” in *Light Scattering in Solids I*, Springer, 1983, pp. 147–204.

[152] H. B. Callen, “HB Callen and TA Welton, Phys. Rev. 83, 34 (1951).,” *Phys. Rev.*, vol. 83, p. 34, 1951.

[153] N. Waeselmann, *Structural transformations in complex perovskite-type relaxor and relaxor-based ferroelectrics at high pressures and temperatures*. 2012.

[154] S. M. Khalil and A. Sedky, “Annealing temperature effect on the properties of Bi:2212 superconducting system,” *Phys. B Condens. Matter*, vol. 357, no. 3, pp. 299–304, 2005.

[155] N. N. Kovaleva *et al.*, “<math display="inline"> <mi>c</mi> </math> -axis lattice dynamics in Bi-based cuprate superconductors,” *Phys. Rev. B*, vol. 69, no. 5, p. 054511, 2004.

[156] F. Venturini *et al.*, “Observation of an Unconventional Metal-Insulator Transition in Overdoped CuO2 Compounds,” *Phys. Rev. Lett.*, vol. 89, no. 10, pp. 107003-1–5, 2002.

[157] Y. Gallais, A. Sacuto, T. P. Devereaux, and D. Colson, “Interplay between the pseudogap and

superconductivity in underdoped HgBa2CuO4+δ single crystals," *Phys. Rev. B*, vol. 71, p. 012506, 2005.

[158] S. A. Kivelson, "Making high T c higher : a theoretical proposal," *Phys. B*, vol. 318, pp. 61–67, 2002.

[159] J. Graf *et al.*, "Universal High Energy Anomaly in the Angle-Resolved Photoemission Spectra of High Temperature Superconductors: Possible Evidence of Spinon and Holon Branches," *Phys. Rev. Lett.*, vol. 98, no. 6, p. 67004, Feb. 2007.

[160] A. D. Gromko *et al.*, "Mass-renormalized electronic excitations at (π,0) in the superconducting state of Bi2Sr2CaCu2O8+δ," *Phys. Rev. B*, vol. 68, no. 17, p. 174520, Nov. 2003.

[161] W. Meevasana *et al.*, "Hierarchy of multiple many-body interaction scales in high-temperature superconductors," pp. 1–7, 2007.